

Influence of coronal mass ejection orientation on dynamics in interplanetary space

Martinić, Karmen

Doctoral thesis / Disertacija

2024

Degree Grantor / Ustanova koja je dodijelila akademski / stručni stupanj: **University of Zagreb, Faculty of Science / Sveučilište u Zagrebu, Prirodoslovno-matematički fakultet**

Permanent link / Trajna poveznica: <https://um.nsk.hr/um:nbn:hr:217:449126>

Rights / Prava: [In copyright](#)/[Zaštićeno autorskim pravom.](#)

Download date / Datum preuzimanja: **2025-03-30**



Repository / Repozitorij:

[Repository of the Faculty of Science - University of Zagreb](#)





University of Zagreb
Faculty of Science
Department of Geophysics

Karmen Martinić

**Influence of coronal mass ejection
orientation on dynamics in interplanetary
space**

DOCTORAL THESIS

Zagreb, 2024



University of Zagreb
Faculty of Science
Department of Geophysics

Karmen Martinić

**Influence of coronal mass ejection
orientation on dynamics in interplanetary
space**

DOCTORAL THESIS

Supervisor:
Dr. Sc. Bojan Vršnak

Zagreb, 2024



Sveučilište u Zagrebu
Prirodoslovno-matematički fakultet
Geozički odsjek

Karmen Martinić

Utjecaj orijentacije koronina izbačaja na dinamiku u međuplanetarnom prostoru

DOKTORSKI RAD

Mentor:
Dr. Sc. Bojan Vršnak

Zagreb, 2024

This doctoral thesis was made at the University of Zagreb, Faculty of Science, Department of Geophysics, under the supervision of Dr. Sc. Bojan Vršnak as a part of the Doctoral programme of Geophysics at the University of Zagreb, Faculty of Science, Department of Geophysics.

Supervisor information

Bojan Vršnak was born in Zagreb on March 16, 1957. He graduated in 1980 in the field of theoretical physics from the Faculty of Science, University of Zagreb, where he also earned his master's degree in astrophysics in 1983 and his doctorate in astrophysics (solar physics) in 1987. Since 1981, he has been employed at the Hvar Observatory, Faculty of Geodesy, University of Zagreb, and since 2000 he has held the title of scientific advisor in a permanent position.

The main research area of Dr. Bojan Vršnak is solar physics, with a particular emphasis on the theoretical and empirical aspects related to eruptive phenomena in the solar atmosphere. This primarily includes the study of magnetohydrodynamic processes and instabilities that lead to coronal eruptions and solar flares. He also studies the formation and propagation of magnetohydrodynamic shock waves in the corona and interplanetary space, as well as the structure and physical state of solar prominences and the global structure of the solar atmosphere. Finally, he investigates the heliospheric propagation of coronal mass ejections, the physics of the Sun-Earth system, and space weather along with the development of predictive models.

He has published a significant number of scientific articles and publications: the NASA-ADS bibliographic database lists 394 items (>12450 citations, 29 items with more than 100 citations, h-index=58), of which 265 are peer-reviewed scientific articles. The WOS/JCR/SCI bibliographic database includes 202 items (9202 citations, h-index=56).

He is a member of the editorial boards of international scientific journals such as Solar Physics, The Scientific World Journal, Journal of Astrophysics, Frontiers in Physics and Astronomy and Space Sciences, Open Astronomy, and Central European Astrophysics Bulletin. He is also a member of associations including the International Astronomical Union (IAU), American Geophysical Union (AGU), European Astronomical Society (EAS), Committee on Space Research (COSPAR), Joint Organization for Solar Observation (JOSO), Community of European Solar Radio Astronomers (CESRA), and the Croatian Astronomical Society (HAD).

B. Vršnak has developed rich research collaborations with scientists from numerous European and global institutions, such as the Air Force Research Laboratory (USA), Astronomical Institute Ondrejov (Czech Republic); Astrophysical Institute Potsdam (Germany); Catholic

University of America (USA); Chinese Astronomical Society (China), Christian-Albrechts-University in Kiel (Germany); International Space Science Institute, Bern (Switzerland); Belgian Institute for Space Aeronomy (Belgium); Institute for Geophysics, Astrophysics and Meteorology, Graz (Austria); NASA - Goddard Space Flight Center (USA); National Solar Observatory (USA); Paris-Meudon Observatory (France); Royal Observatory of Belgium (Belgium); Udaipur Solar Observatory (India); Naval Research Laboratory (USA).

He has been a project leader or collaborator on numerous international, bilateral, and domestic scientific projects in the field of solar physics and space weather, including 4 EU FP7 /HORIZON2020 projects, 1 European Space Agency project, and several bilateral projects with Austria and Germany. On six occasions, he was a member of the international expert research team at the International Space Science Institute, Bern (so-called ISSI team).

Dr. Vršnak teaches at the Faculty of Science in Zagreb - a course in the doctoral program: Solar Magnetohydrodynamics. He was a visiting professor at Karl-Franzens University Graz three times: in 2001, teaching the course Solar Flares; in 2007, teaching Solar Flare and Coronal Mass Ejection Physics; and in 2014, teaching Coronal Mass Ejection Physics. He has supervised 15 doctoral dissertations, 8 master's theses, and 11 undergraduate theses. He is the author of the university textbook "Foundations of Plasma Physics" (Školska knjiga, 1996), three manuals, and 14 book chapters. He is active in popularizing astronomy (several public lectures annually and numerous popular science articles).

In 2017, he was awarded the prestigious "Kristian Birkeland Medal" by the international scientific committee for outstanding achievements in the field of space weather during the "European Space Weather Week." According to a comprehensive scientometric study by Stanford University based on the SCOPUS database of scientific productivity and citations worldwide, he is among the top 2% of the most influential scientists globally in his field, both for his entire scientific career and for the years 2019 and 2022. He received the "Župan's Recognition" for exceptional contributions to scientific research (Rečica ob Savinji, Slovenia, 2021). In 2022, an asteroid in the asteroid belt was named (179874) Bojanvršnak = 2002 TS315 in his honor.

Acknowledgements

I would like to thank my supervisor, Dr. Sc. Bojan Vršnak, who supported me during the critical moments of my PhD. Our discussions were very important for my professional development.

The biggest thanks go to my co-supervisor, Dr. Sc. Mateja Dumbović. Her guidance has played a crucial role in shaping my scientific career, and I am deeply grateful for the knowledge and insights she has shared with me.

My special thanks go to my co-authors, Assoc. Prof. Dr. Manuela Temmer from the University of Graz and Dr. Sc. Eleanna Asvestari from the University of Helsinki. I thank them for their discussions and advice regarding the direction of my research. I would also like to thank all of the other co-authors: Assoc. Prof. Astrid Veronig from the University of Graz, Dr. Sc. Jaša Čalogović from the University of Zagreb, Dr. Sc. Tobias Rindlisbacher from the University of Bern, and Asst. Prof. Nada Al-Haddad from the University of New Hampshire. Their collaboration and contributions were very valuable for my research.

I gratefully acknowledge the financial support from the Croatian Science Foundation under the project IP-2020-02-9893 (ICOHOSS) and the Croatian Science Foundation within the scope of the "Young Researchers' Career Development Project - Training New Doctoral Students" program. Additionally, I acknowledge the support from the Austrian-Croatian Bilateral Scientific Projects "Comparison of ALMA Observations with MHD-Simulations of Coronal Waves Interacting with Coronal Holes," "Multi-Wavelength Analysis of Solar Rotation Profile," and "Analysis of Solar Eruptive Phenomena from Cradle to Grave" for their contributions to this thesis.

I am deeply grateful to my Family- Matera, Tatera, Nina and Nikola. Your love has been a steady presence in my life, and I feel incredibly fortunate to have each of you by my side.

Influence of coronal mass ejection orientation on dynamics in interplanetary space

Karmen Martinić

Department of Geophysics, Faculty of Science, University of Zagreb

Abstract

When coronal mass ejections (CMEs) propagate through interplanetary space, they interact with the surrounding magnetic field and solar wind, which are neither homogeneous nor isotropic. Consequently, CMEs with different orientations may face varying environmental conditions, leading to different interactions based on their orientation. Our observational studies include remote and in-situ analysis of CMEs. We derived their orientation near Sun using 3D and 2D CME geometry reconstruction methods based on remote observations, as well as their orientation near Earth using a rotational profile of the magnetic field detected in-situ. A complementary simulation study was performed using the EUropean Heliospheric FORecasting Information Asset, a 3D magnetohydrodynamic (MHD) model with two spheromak CMEs, differing only in inclination. In general, we found that plasma flows in front of the CME differ based on orientation, though no significant difference in MHD drag between different orientations was found. These findings enhance our understanding of CME-ambient interactions, which is crucial for advancing space weather predictions.

Keywords: coronal mass ejections, heliosphere, inclination effect, magnetohydrodynamic drag, non-radial flows

Supervisor: Dr. Sc. Bojan Vršnak

Reviewers: Dr. Sc. Roman Brajša, Assoc. Prof. Dr. Manuela Temmer, Prof. Dr. Sc. Snježana Markušić

Utjecaj orijentacije koronina izbačaja na dinamiku u međuplanetarnom prostoru

Karmen Martinić

Geofizički odsjek, Prirodoslovno-matematički fakultet, Sveučilište u Zagrebu

Sažetak

Koronini izbačaji (engl., *coronal mass ejections*, CMEs) u međuplanetarnom prostoru međudjeluju s okolnim magnetskim poljem i Sunčevim vjetrom, koji ne pokazuju homogenost niti izotropnost. Posljedično, CME-ovi različitih orijentacija nailaze na drugačije uvijete u međuplanetarnom prostoru, stoga njihovo međudjelovanje može ovisiti o orijentaciji CME-ova. Proučavali smo CME-ove različitih orijentacija pomoću daljinskih i in-situ podataka. Orijetacija CME-ova blizu Sunca određena je koristeći metode 3D i 2D rekonstrukcije geometrije iz daljinskih mjerenja. Orijetacija CME-a u blizini Zemlje određena je koristeći rotacijski profil magnetskog polja mjerenog in-situ. Komplementarna analiza je provedena pomoću European Heliospheric Forecasting Information Asset, 3D magnetohidrodinamičkog (MHD) modela, sa sferomak reprezentacijom dva CME-a koji se razlikuju jedino po orijentaciji. Pokazali smo da tok plazme, neposredno ispred CME-ova, ovisi o orijentaciji istih, međutim značajna razlika u MHD otporu nije pronađena. Ovaj rad doprinosi boljem razumijevanju interakcije između CME-ova i ambijentalog magnetskog polja te Sunčevog vjetra, što je ključno za poboljšanje predikcija u okviru svemirskog vremena (engl. *space weather*).

Ključne riječi: koronin izbačaj, heliosfera, inklinacija, magnetohidrodinamički otpor, ne-radijalni tokovi plazme

Mentor: Dr. Sc. Bojan Vršnak

Recenzenti: Dr. Sc. Roman Brajša, Assoc. Prof. Dr. Manuela Temmer, Prof. Dr. Sc. Snježana Markušić

Contents

1	Introduction	1
1.1	The Sun and interplanetary space	1
1.1.1	The Parker spiral model	3
1.1.2	Quasi-dipolar magnetic field	4
1.1.3	Solar cycle and related magnetic field and solar wind variations	5
1.2	Coronal mass ejections	7
1.2.1	The origin of coronal mass ejections	8
1.2.2	Remote and in-situ observations of coronal mass ejections	9
1.2.3	CME modelling and arrival predictions	12
1.3	Motivation	16
2	Scientific Papers	19
2.1	Determination of coronal mass ejection orientation and consequences for their propagation	19
2.2	Effects of coronal mass ejection orientation on its propagation in the heliosphere	30
2.3	Probing coronal mass ejections inclination effects with EUHFORIA	42
3	Unified discussion	61
4	Conclusions	65
	References	67
	Curriculum vitae	75
	Prošireni sažetak na hrvatskom jeziku	77

Chapter 1

Introduction

This thesis includes the research related to the interaction of the most violent eruptions originating on the Sun, known as coronal mass ejections (CMEs), and the ambient environment dominated by the Sun's magnetic field and continuous supersonic charged particle outflow known as the solar wind. The way CMEs evolve and propagate through interplanetary space remains a subject of limited understanding. However, especially in today's modern and technology-driven society, it is crucial to study these eruptions and to improve predictions on their arrival time, speed, and geoeffectiveness. CMEs' predictions are part of *space weather*, a relatively young field of research that connects the Sun, heliosphere, and near-Earth environments such as magnetosphere, ionosphere, and atmosphere. Space weather events that have an impact on Earth's environment can potentially harm satellites and disrupt ground-based technology. These events can lead to electrical power outages, disruptions in Global Navigation Satellite Systems (GNSS), and interference with radio transmission signals, particularly during severe geomagnetic storms. Given the essential role that satellite technologies play in our modern world, it is of utmost importance to enhance our capabilities for monitoring and forecasting space weather. The most important space weather effects are summarised in Figure 1.1.

1.1 The Sun and interplanetary space

Interplanetary space is influenced primarily by the presence of the Sun and its various activities. Parker (1958) laid the foundation for a coherent and comprehensive understanding of the heliosphere. A theoretical framework was introduced to explain the existence and behavior of the solar wind. The solar wind is a continuous stream of charged particles emanating from the Sun's upper atmosphere. This plasma consists mainly of electrons, protons, and alpha particles and reaches velocities of 250 – 750 km/s. Parker (1958) also introduced the concept of

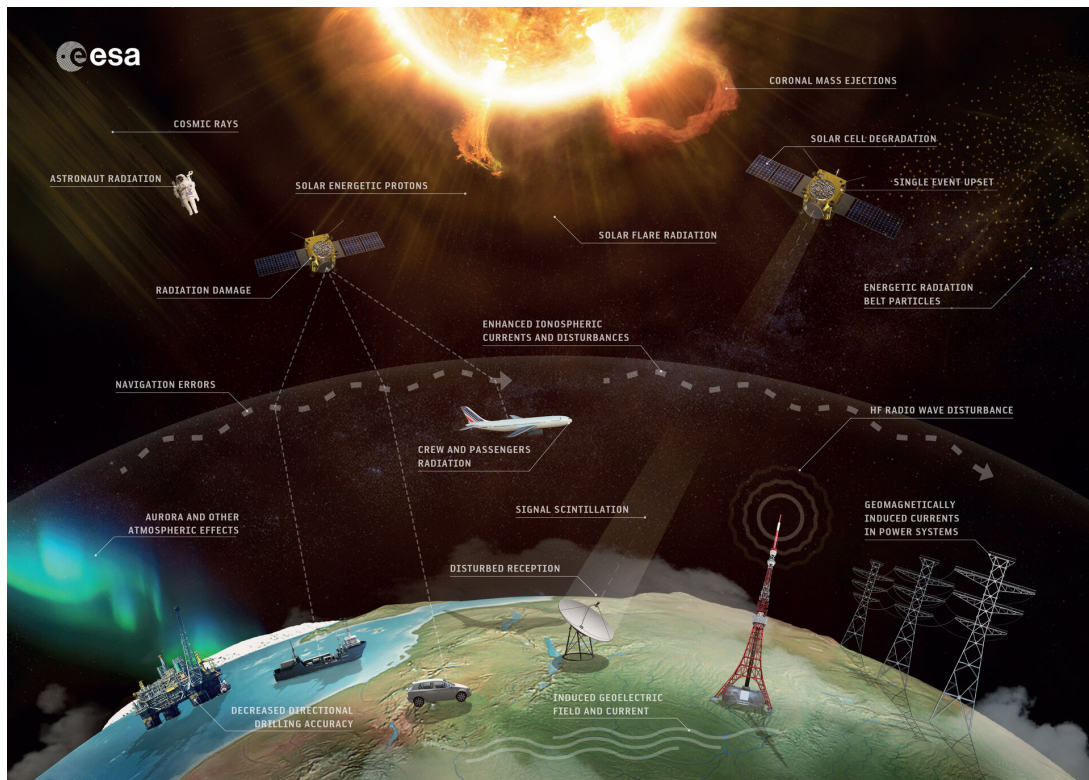


Figure 1.1: Schematic overview of space weather effects. Credit by ESA.

the Parker spiral, which describes the spiral shape of the Sun's magnetic field lines as they are carried outward by the solar wind. Another major milestone in heliophysics research was the launch of the twin Voyager spacecraft (Behannon et al., 1977), which provided measurements of the most distant parts of the heliosphere. These measurements supplemented numerous studies that enhanced our understanding of heliosphere (Burlaga et al., 1981; Burlaga et al., 2005; Stone et al., 2013; Cummings et al., 2016). Another important mission related to heliosphere exploration is the Ulysses spacecraft (Balogh et al., 1992), launched in 1990. Ulysses was the first spacecraft to explore the 3-dimensional (3D) structure of the heliosphere over a wide range of latitudes. The mission ended in 2009 after nearly 3 orbits around the Sun. Efforts towards better understanding of the Sun and the heliosphere continued with the launch of the Wind spacecraft (Ogilvie & Parks, 1996), Advanced Composition Explorer (ACE, Chiu et al., 1998), Solar and Heliospheric Observatory (SOHO, Domingo et al., 1995), and Solar Dynamic Observatory (SDO, Pesnell et al., 2012). Current solar and heliospheric research objectives are summarized within Parker Solar Probe (PSP) and Solar Orbiter (SolO) mission objectives (Raouafi et al., 2023; Müller et al., 2020; Berghmans et al., 2023). They focus on understanding the solar dynamo, the heating of the solar corona, the origin of the solar wind, mechanisms that

energize and transport energetic particles, and solar transients that drive variability of the heliosphere that will ultimately lead to advancing space weather predictions. The interested reader is referred to Temmer et al. (2023) for the current status and outlook of CME-related research.

In the following subsections, 1.1.1 and 1.1.2 a brief overview of the stationary heliosphere is given, an approximation that is most valid near solar minimum when the solar corona is slowly evolving. In the next subsection, 1.1.3, we highlight the fluctuations in the heliosphere due to solar cycle variations and the existence of large heliospheric transients, such as the interaction of fast and slow solar wind streams and CMEs.

1.1.1 The Parker spiral model

The solar corona is the uppermost layer of the solar atmosphere where the solar wind originates. Assuming a frozen-in condition state due to the high electrical conductivity of the plasma in the corona, the solar magnetic field is pulled into interplanetary space by the supersonic solar wind. This means that the configuration of the interplanetary magnetic field (IMF) is determined by the velocity of the solar wind and the rotating source, i.e., the rotation of the Sun with angular velocity $\Omega = 2.7 \cdot 10^{-6}$ rad/s. Under the condition of only radial solar wind outflow with constant velocity and assuming that the footpoints of the magnetic field are fixed and therefore rotate with the Sun, we can derive the simplest form of the IMF. In the spherical coordinate system (r, θ, ϕ) rotating with the Sun, the solar wind has the following components:

$$U_r = u; \quad U_\phi = -\Omega r \sin \theta; \quad U_\theta = 0.$$

Combining the above equations one can get:

$$\frac{1}{r} \frac{dr}{d\phi} = \frac{U_r}{U_\phi} = \frac{u}{-\Omega r \sin \theta}.$$

Integrating the above equation from R_0 to r and from ϕ_0 to ϕ , under the assumption that $u = u_0 = \text{const.}$, we obtain:

$$r - R_0 = -\frac{u_0}{\Omega \sin \theta} (\phi - \phi_0),$$

where ϕ_0 is the initial azimuthal angle at the surface of the Sun R_0 . The above equation repre-

sents, in a purely geometric sense, a familiar Archimedean spiral. The winding distance, i.e., the radial distance at which the spiral has wound around the Sun, assuming that $u_0 = 400$ km/s, is about 6 AU. Under the same conditions, the Parker spiral near the Earth forms an angle of about 45° with the Sun-Earth line, as shown in Figure 1.2.

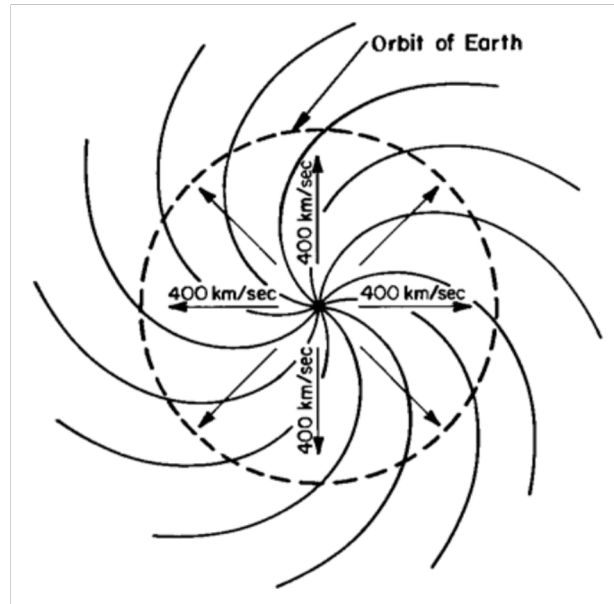


Figure 1.2: Illustration of Parker's spiral model for the interplanetary magnetic field in the solar equatorial plane (as seen from above the north pole) with a radial solar wind expansion of 400 km/s. The figure is taken from Kivelson & Russel (1996).

1.1.2 Quasi-dipolar magnetic field

In the first-order approximation, the solar magnetic field can be viewed as a dipole with an axis aligned with the solar rotation axis (Figure 1.3 left, dashed lines). However, due to the existence of solar wind and solar rotation, the field lines are pulled further away and ripped open near the equator (Figure 1.3, solid lines). Figure 1.3, left panel, was adapted from Pneuman & Kopp (1971) and shows the results of the MHD simulation of a dipolar magnetic field imposed on the photosphere and with solar wind outflow imposed. In the region near the equator where oppositely oriented magnetic field lines meet, the current sheath, i.e., the heliospheric

current sheath (HCS), is formed. The HCS is known to have the shape of a "ballerina skirt" (see Figure 1.3). Its characteristic ripple is due to the angle of inclination of the dipole axis of the magnetic field with respect to the axis of rotation of the Sun and to deviations from an ideal dipole field (Owens & Forsyth, 2013). The HCS presented here was derived from a combined simulation of the solar corona and heliosphere using the MHD approach, as described in Odrzciel et al. (2004). This simulation was performed during the 1912 Carrington rotation near the equator. The presence of red and blue colors in the plot indicates deviations or "warps" in the HCS structure extending about 10 degrees both above and below the equator. The thick black line represents the trajectory of the Earth through the HCS in this particular time frame, the beginning of solar cycle 23 (near solar minimum).

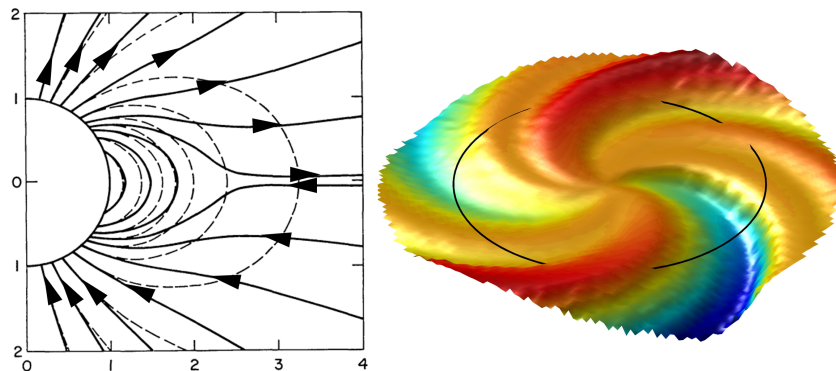


Figure 1.3: Left: Illustration of dipolar magnetic field lines (dashed) being pulled away by the solar wind (solid lines), as shown in the model of Pneuman & Kopp (1971). Right: 3D representation of the HCS near to solar minimum. The thick black line represents the trajectory of the Earth as it passes through the HCS. The figure was adapted from Owens & Forsyth (2013).

1.1.3 Solar cycle and related magnetic field and solar wind variations

The solar cycle, i.e. the approximately 11-year periodicity in Sun's activity, was first discovered by the German astronomer Samuel Heinrich Schwabe back in 1843 (Arlt, 2011; Schwabe, 1844). The major contribution to continuous quantitative recording and a better understanding of the solar cycle variations continued with Swiss astronomer Rudolf Wolf (Wolf, 1856). In the period of about 11 years, the periodicity is visible in the number and size of sunspots, solar flares, solar prominences, and CMEs. For most of these phenomena, the abundance is the greatest in the maximum of the solar cycle and smallest in the minimum of the solar cycle. Figure 1.4 shows schematically the modification of the magnetic field within one solar cycle (Figure 1.4,

uppermost panels), figure adapted from High Altitude Observatory ¹, solar disk magnetograms from SOHO/EIT (Scherrer et al., 1995) provided by Solar monitor ² dating from June 1996 to June 2006 with the time step of two years (Figure 1.4, middle panels), and the monthly international sunspot number as a function of time (Figure 1.4, bottommost panel) provided by WDC-SILSO ³, Royal Observatory of Belgium, Brussels. We can see how the Sun's activity varies from very low in 1996 (solar minimum), to very high around 2001 (solar maximum), and then in 2006 back to low activity and to another solar minimum. As mentioned earlier, the IMF is well approximated during the solar minimum by a quasi-dipolar magnetic configuration with a small inclination between the magnetic and rotational axes. Consequently, the HCS aligns closely with the Sun's rotational equator. Also, coronal holes as a source of fast solar wind are mostly restricted to the polar regions. During this period, CMEs are much rarer and primarily observed at low latitudes (Owens & Forsyth, 2013). During solar maximum, the situation is much more complex, quadrupolar and higher order moments gain importance (Hoeksema et al., 1982; Wang et al., 2000). The coronal magnetic field changes more frequently and thus the number of CMEs and their latitudinal extent increases. As for the solar wind, as shown by the Ulysses observations (McComas et al., 2003), the area of the coronal hole at the pole shrinks, and the fast solar wind now occurs close to the ecliptic plane.

The solar dynamo provides the underlying explanation for this variability. Babcock (1961) presented the first conceptual dynamo model after summarizing observational data. To this day, many scientists are working to understand the dynamo better and to develop better, more accurate models of it (Leighton, 1969; Duvall, 1979; Howe, 2009; Ulrich, 2010; Charbonneau, 2010). The solar dynamo is a collection of complex and interacting physical processes that generate and maintain the solar magnetic field in a periodic manner and are responsible for solar magnetic reversals. The most fundamental elements of the dynamo model are the so-called Ω and α effects. The Ω effect is dominated by the Sun's differential rotation, which causes a predominantly poloidal magnetic field to stretch and twist around the Sun. In this process, the toroidal magnetic field component is generated. (See Figure 1.4, top panels a) and b)). The α effect, as described by Steenbeck et al. (1966), explains the restoration of the original poloidal field. The α effect refers to the twisting of the toroidal field by the Coriolis force as it rises with the convection cells (see Figure 1.4, top panel c)). After the solar maximum, the meridional flow has shifted the magnetic flux toward the pole (see Figure 1.4, topmost panels d) and e)), and finally, the flux cancellation restores the poloidal component, but now with reversed polarity (see Figure 1.4, topmost panel f)).

¹<https://www2.hao.ucar.edu/hao-science/science-topic/sun-as-a-dynamo>

²<https://www.solarmonitor.org/>

³<https://www.sidc.be/SILSO/home>

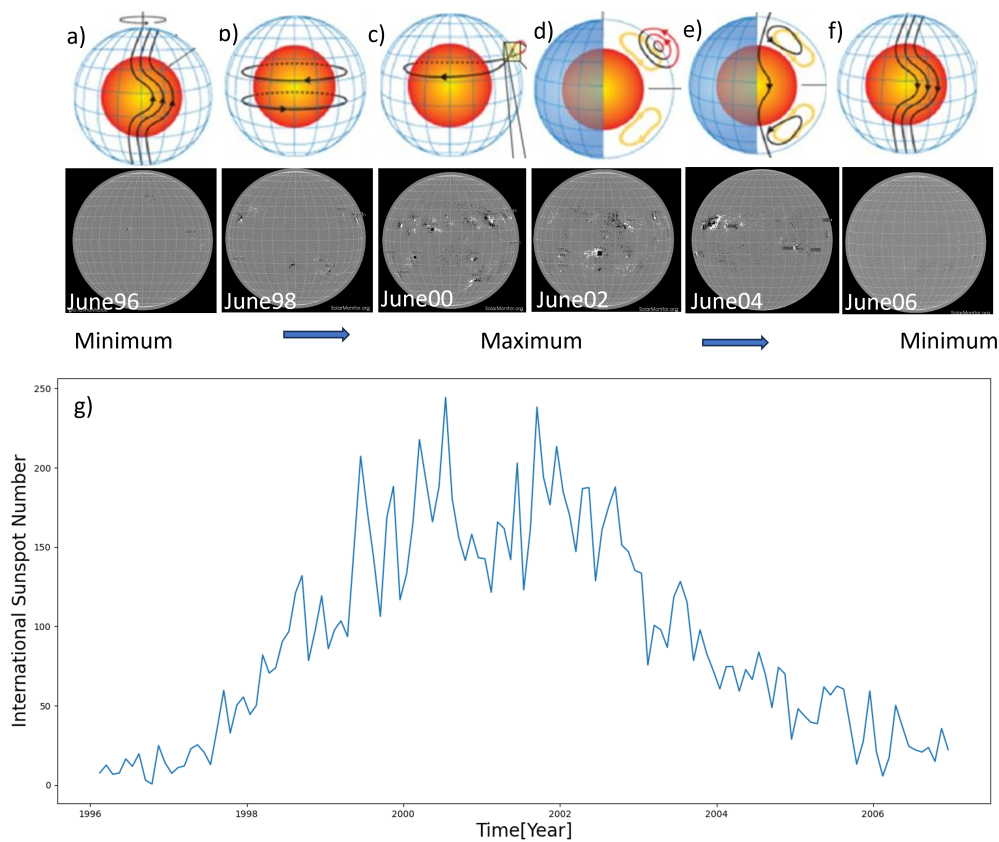


Figure 1.4: The upper panels show the change in the magnetic field within one solar cycle. The middle panels show magnetogram data of the solar disk from SOHO /EIT, ranging from June 1996 to June 2006 with a time step of two years. The lower panel shows the monthly international sunspot number as a function of time. The upper panels were adapted from the High Altitude Observatory ⁴, the magnetograms of the solar disk in the middle panels were adapted from the Solar Monitor ⁵ and the lower panel was created from data from the WDC-SILSO ⁶, the Royal Observatory of Belgium in Brussels.

1.2 Coronal mass ejections

Coronal mass ejections (CMEs) are massive, magnetically dominated eruptions originating in the solar corona. Most CMEs, especially during the peak of the solar cycle, originate in regions known as active regions (ARs) (for a definition of ARs and historical context, see van Driel-Gesztelyi & Green, 2015). ARs are regions characterized by intense magnetic activity and high-energy processes. These regions are often associated with sunspots, which are areas of reduced surface temperature caused by strong magnetic field that inhibit convection and heat transport. ARs are locations where the Sun's magnetic field lines exit and re-enter the solar

surface. After their outburst, CMEs propagate and expand in interplanetary space. During their propagation, they interact with the surrounding charged particles and magnetic field structures, such as the Earth's magnetic field. This interaction produces geomagnetic storms that can cause significant damage in the near-Earth environment (Zhang et al., 2003; Zhang et al., 2004; Zhang et al., 2021a).

CMEs are often associated with solar flares and filament eruptions. Solar flares are intense bursts of energy and light emanating from the surface of the Sun. They are caused by the sudden release of magnetic energy stored in the Sun's atmosphere and they result in the emission of various forms of electromagnetic radiation. Solar prominences (called filaments when observed on the solar disk) are dense and cool chromospheric materials located in the solar corona and held against gravity by the magnetic field. Although these three phenomena can be observed independently and one does not necessarily determine the existence of the other, these three phenomena are undeniably related and can be explained as different aspects of a single physical process within the theory of a "standard flare model" (also known as the CSHKP model). For more on the model and CME initiation, see section 1.2.1.

Once the CME outburst occurs, we can track it remotely using coronagraphs and heliospheric imagers aboard satellites. The first CME observations were performed shortly after the launch of the Orbiting Solar Observatory (OSO-7) satellite in 1970 (Tousey, 1973; Howard, 2006). CMEs can also be observed in-situ in interplanetary space as they propagate, with direct measurements of plasma and magnetic field features as the CME passes the satellite. Gosling et al. (1975) were the first to establish a link between remotely observed CMEs and their in-situ CME signatures in data from the Pioneer 9 spacecraft. Further details on the remote and in-situ observations and the different properties of CMEs are described in section 1.2.2.

1.2.1 The origin of coronal mass ejections

The significant discovery of solar flares by Carrington (1859) and Hodgson (1859), combined with Hale's study (Hale, 1908) of magnetic field in sunspots, acted as a catalyst for understanding the origin of CMEs and related phenomena. There followed a period of extensive debate about the close connection between solar flare generation and magnetism in ARs. Advances in ground-based and space-based telescopes and the ever-increasing capabilities of numerical simulations have accelerated this trend and contributed significantly to our understanding of the physical background of CMEs and related phenomena. It is widely accepted that ARs are formed by the emergence of a toroidal magnetic flux originating from the deeper convection zone. This process is commonly referred to as flux emergence, as highlighted by Parker (1955). In most dynamo models (such as Charbonneau, 2010 and Brun & Browning, 2017), the origin

and enhancement of toroidal flux is due to turbulence and shear within the tachocline. However, there are considerations that additional energy could be added to the system by small-scale photospheric motions such as shear, flux cancelation, twisting by rotation, and braiding due to granular motion. Overall, these findings gave significant support to the established "standard flare model" based on the concept of magnetic reconnection, known as the CSHKP model, named after its principal authors (Carmichael, 1964, Sturrock, 1966, Hirayama, 1974, Kopp & Pneuman, 1976). Discoveries from the end of the last century suggest that CMEs consist of a so-called flux-rope (FR) structure (Chen et al., 1997; Bothmer & Schwenn, 1998; Moore et al., 2001). In its simplest form, a FR is a cylindrical structure in which a poloidal magnetic field component rotates about an axial magnetic field component that follows the central axis of the cylinder (Lundquist, 1950). FR is a key component in the framework of the CSHKP model and its 2D (Shibata et al., 1995) and more complex 3D representations (such as Aulanier et al., 2012, Janvier et al., 2013). The main features of the CSHKP model are shown in Figure 1.5 and can be explained as highlighted in Toriumi & Wang (2019): "The magnetic flux rope becomes unstable and erupts into the higher atmosphere, entraining the overlying coronal field. The legs of the coronal field are drawn as inflows into a current sheet underneath the flux rope and reconnect. The outflows from the reconnection region further enhance the eruption of the river rope. The field lines after reconnection form a cusp structure, while the accelerated electrons from the reconnection site precipitate along the field lines and heat the chromosphere to produce flare ribbons."

1.2.2 Remote and in-situ observations of coronal mass ejections

CMEs can be observed remotely with coronagraphs onboard satellites, instruments designed with the occulting disk to block the bright photospheric light that is around six orders of magnitude brighter than the solar corona. Coronal features, such as CMEs can be observed due to Thomson scattering of photons from the photosphere on free electrons in the solar corona. Consequently, features observed by coronagraphs depend on the column electron density in the plane of sky near the Sun (Hayes et al., 2001). This way, CMEs can be observed in white light as they propagate in the middle and upper corona. An example of one CME observed with Large Angle and Spectrometric Coronagraph (LASCO) coronagraphs (Brueckner et al., 1995) onboard a SOHO spacecraft on the second of December 2002 is shown in Figure 1.6. The left panel shows CME observed with LASCO-C2 coronagraph with field of view (FOV) 1.5-6 R_S , and on the right is the same CME approximately two hours later as seen within the LASCO-C3 with FOV 3.7-30 R_S . The figure was obtained with the JHeliowiever visualization tool (Müller et al., 2017). Traditionally, the bright core represents the erupting prominence, the magnetic

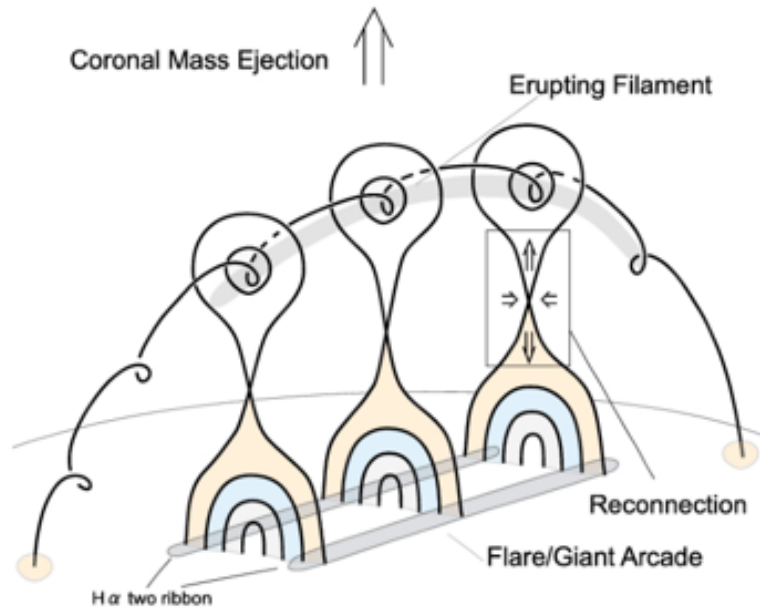


Figure 1.5: Illustration of the main features of the CSHKP model. The CME is represented by the FR erupting structure along with the erupting filament. The region of reconnection is shown below the erupting FR, as are the flare ribbons as a direct result of the reconnection process. The figure was adapted from Owens & Forsyth (2013).

cavity represents the FR of the CME, and the bright front is the ambient plasma being piled up in front of the propagating and expanding FR part. More recently, this traditional interpretation of observed three-part structure in white light coronagraphic images has been challenged. For details see Howard et al. (2017), Song et al. (2023), and references therein.

Once CMEs erupt, they propagate and expand through the interplanetary medium. Typically, CMEs observed using instruments like heliospheric imagers or in-situ devices aboard spacecraft placed throughout the heliosphere are labeled as Interplanetary CMEs (ICMEs). However, this conventional separation between CMEs and ICMEs has come into question recently. Thanks to missions like the Parker Solar Probe and Solar Orbiter, we can now collect measurements of CMEs/ICMEs simultaneously, both from the upper corona and up close in the innermost part of the heliosphere. Even though, already with the Solar TERrestrial RELations Observatory (Russell, 2008, STEREO) mission one could undouble link CME and ICMEs using the heliospheric imagers, these simultaneous measurements from PSP and SoIo have additionally blurred the line between CMEs and ICMEs, making it increasingly difficult to distinguish between the two. In in-situ measurements of ICMEs, frequently, a distinct three-part pattern can be observed in these events: a shock, a sheath, and a magnetic obstacle (MO) i.e. the FR part. The shock onset is marked by a sudden increase in the magnetic field strength, the speed of the

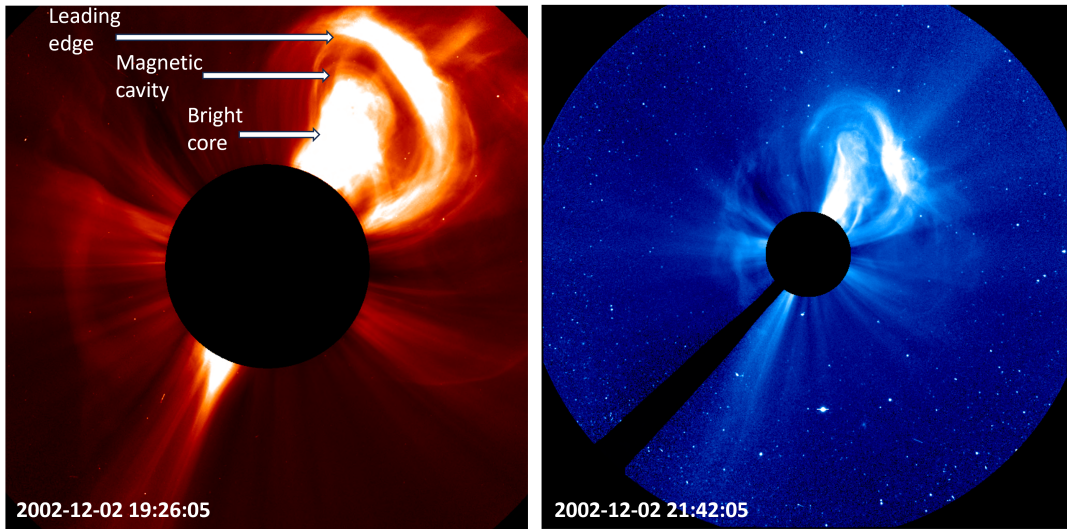


Figure 1.6: White light image of a CME that occurred on the second of December 2002, observed by the LASCOC2 coronagraph (left) and by the LASCOC3 coronagraph (right). CME displays a typical three-part structure, additionally marked on the left part of the figure.

solar wind, and the temperature. Moving into the sheath region, we encounter a zone of high turbulence. Here, the solar wind becomes denser and hotter, while the IMF gets compressed and wraps around the FR of the ICME. Additionally, the sheath region typically displays more significant fluctuations in all measured parameters and has a smaller radial extent compared to the FR section of the ICME (as reviewed in Kilpua et al., 2017). After the sheath part, the in-situ spacecraft encounters the magnetic structure. The magnetic structure is usually denoted as a magnetic obstacle (MO) and a special subgroup of MO consists of the so-called magnetic clouds (MC). MCs are notable for their intensified and smooth rotation of the magnetic field, lower proton temperatures, and reduced plasma beta as first described by Burlaga et al. (1981). Gosling (1990) and Cane & Richardson (2003) have shown that approximately one-third of all in-situ observed CMEs display MC characteristics. Figure 1.7 displays schematically an ICME (left panels) and in-situ signatures of an ICME that appeared on the 14th of July 2012 as observed by the WIND spacecraft (Ogilvie & Parks, 1996) (right panels) located at L1 Lagrangian point near Earth. The panels on the right show, magnetic field magnitude, magnetic field components in the Geocentric Solar Ecliptic (GSE) coordinate system, proton number density, thermal velocity as a measure of temperature, plasma beta parameter, and solar wind velocity, from top to bottom, respectively. The black vertical line denotes the shock onset time, after which the sheath region follows. Two dotted green lines mark the beginning and end of the MC part of the ICME. Although remotely observed CMEs are undeniably linked to their interplanetary counterparts observed in-situ, establishing a solid connection between the two

remains a significant challenge in scientific research. It's crucial to acknowledge that there are instances where the associations made by different researchers do not align. The task of linking in-situ measurements of ICMEs with their solar origins is complex. This complexity arises from the complex and not fully comprehended kinematic evolution of CMEs. One of the currently, most frequently used CME-ICME association lists are Richardson & Cane (2010), The Space Weather Database Of Notifications, Knowledge, Information (DONKI, ⁷), and Heliospheric Cataloguing, Analysis and Techniques Service (HELCASTS, ⁸).

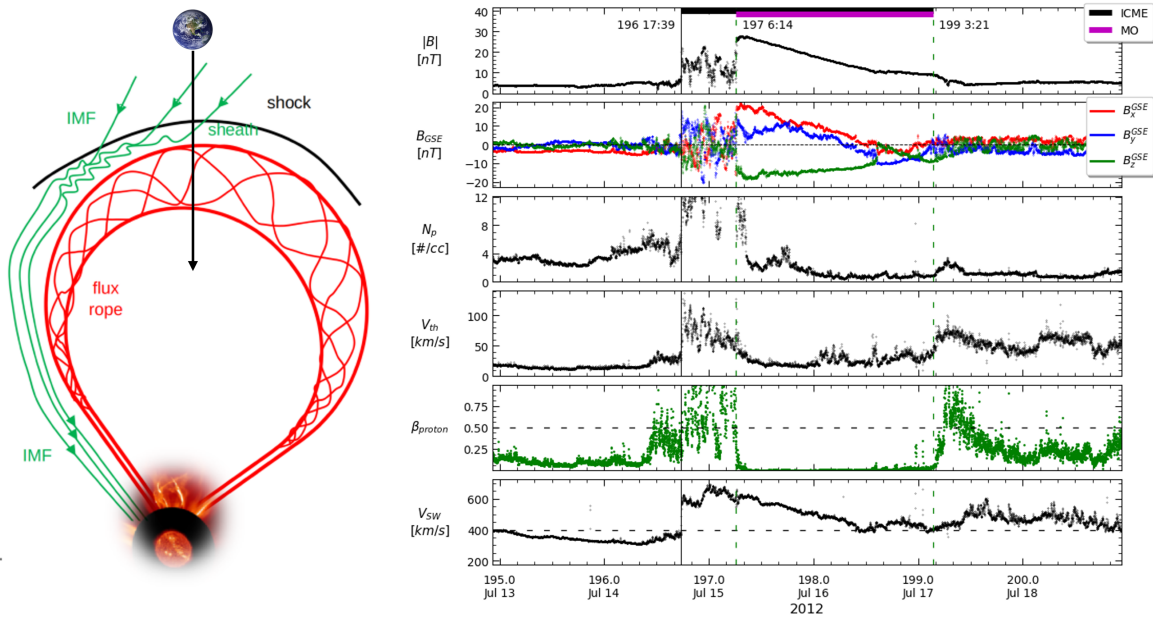


Figure 1.7: Left: A schematic representation of an ICME including, a shock front, turbulent sheath region, and magnetic structure. The figure was adapted from Zhang et al. (2021b) Right: In-situ measurements of 14th July 2012 ICME observed by Wind spacecraft at L1 Lagrange point in the near-Earth environment. Given are, magnetic field magnitude, magnetic field components in the GSE coordinates, proton number density, thermal speed, plasma beta parameter, and solar wind speed, from top to bottom, respectively. The first vertical line denotes shock onset, the second is the MC onset, and the third is the MC end, from left to right, respectively. The figure was adapted from Nieves-Chinchilla et al. (2018).

1.2.3 CME modelling and arrival predictions

CMEs are one of the main space weather drivers (Gosling, 1993; Zhang et al., 2003; Zhang et al., 2004 Koskinen & Huttunen, 2006; Hudson et al., 2006), and thus it is crucial to predict

⁷<https://kauai.cmc.gsfc.nasa.gov/DONKI/>

⁸<https://www.helcats-fp7.eu/products.html>

the time of their arrival at Earth, as well as their potential influence on the near-Earth environment, i.e. geoeffectiveness. Numerous case studies and extensive sample investigations have yielded a diverse range of proposed methods and models. These approaches encompass empirical methods (e.g. Gopalswamy et al., 2001), physics-based analytical models (e.g. Vrřnak et al., 2014; Möstl et al., 2017; Dumbović et al., 2018) and MHD models (e.g. Odstrcil et al., 2004; Pomoell & Poedts, 2018), as well as machine-learning models (e.g. Sudar et al., 2016; Liu et al., 2018). A central location for the space weather scientific research community to submit their forecast in near real-time and compare forecasting methods when the event has arrived is Community Coordinated Modeling Center (CCMC) CME Scoreboard⁹. The most recent analysis of the CCMC CME Scoreboard can be found in Kay et al. (2024). Details, recent advances, and comparisons between the different models' performances can be found in Vourlidas et al. (2019) and Verbeke et al. (2019), and references therein. In summary, models are able to predict the shock-sheath arrival within ± 10 hours and with a standard deviation often exceeding 20 hours. As nicely highlighted in Temmer (2021) the community needs to strive for a better understanding of model limitations and work towards joint effort from the modeling and observational community to improve knowledge on CME-solar wind coupling and to improve space weather forecast.

Drag-based models

Drag-based models are founded on the observational findings that fast CMEs decelerate, while slow CMEs accelerate in the ambient solar wind (Sheeley et al., 1999; Gopalswamy et al., 2001; Vrřnak et al., 2004; Manoharan, 2006; Vrřnak et al., 2008). Meaning, that the drag force dominates the CME dynamics after a certain distance in the heliosphere (Sachdeva et al., 2015). All drag-based models are based on a simple analytical equation:

$$a_d = -\gamma(v - w)|v - w| \quad (1)$$

v is the speed of the CME, w is the solar wind speed, and γ is drag based parameter, given by the following equation:

$$\gamma = C_d \frac{A \rho_w}{M + M_V}, \quad (2)$$

⁹<https://kauai.ccmc.gsfc.nasa.gov/CMEscoreboard/>

where C_d is the dimensionless drag coefficient, A , is the CME cross section, ρ_w is the solar wind density, M is CME mass, and M_V is the so-called virtual mass that accounts for the mass displaced by the CME during its propagation. Even though the drag in interplanetary space is represented with an equation that also resembles the drag in an aerodynamic case, it should be noted that the above-given equations do not account for viscosity or particle collision, but rather resemble the interaction of CME with an ambient magnetic field such as the production of MHD waves (Cargill et al., 1996) and magnetic field line draping (Gosling & McComas, 1987), which is known as magnetohydrodynamic-aerodynamic drag, i.e. MHD drag.

Drag-based models usually employ the fundamental drag equation in a consistent manner, adapting it to different CME geometries and different dimensions. Summary of existing Drag-based models can be found in Dumbović et al. (2021): "...1D Drag-Based Model (DBM, Vršnak et al., 2013, 2014) and Enhanced DBM (Hess & Zhang, 2014, 2015), 2D Drag-Based Model (Žic et al., 2015), the 2D Ellipse Evolution Model (ElEvo, Möstl et al., 2015) and a version of ElEvo using data from Heliospheric Imagers (ElEvoHi, Rollett et al., 2016), and 3D flux rope models such as ANother Type of Ensemble Arrival Time Results (ANTEATR, Kay and Gopalswamy, 2018) or 3-Dimensional Coronal ROpe Ejection (3DCORE, Möstl et al., 2018). Since DBMs use an analytical equation to describe the time-dependent evolution of the CME, they are computationally efficient and thus widely used in probabilistic/ensemble modeling approaches (e.g., Amerstorfer et al., 2018, 2021; Dumbović et al., 2018, Kay and Gopalswamy, 2018; Napoletano et al., 2018; Kay et al., 2020)." In Dumbović et al. (2021) and reference therein, one can find a comprehensive overview of five versions of drag-based models that have been developed by Hvar Observatory in close collaboration with the solar and heliospheric group at the University of Graz. Vourlidas et al. (2019) found that Drag-based models by Dumbović et al. (2018) and by Vršnak et al. (2014) perform on par with much more complex, and computationally much more expansive 3D MHD models.

European Heliospheric Forecasting Information Asset

The European Heliospheric Forecasting Information Asset (EUHFORIA) was introduced by Pomoell & Poedts (2018). It is a 3D model that comprises two key components: a coronal model and a heliosphere model that includes the propagation of CMEs. The coronal model is a semi-empirical background solar wind model that is based on a semi-empirical relationship between topological properties of the coronal magnetic field and measured solar wind parameters. The basis for the coronal model are hourly updated synoptic magnetograms, data provided by the Global Oscillation Network Group (GONG) of the National Solar Observatory (Harvey et al., 1996). In this coronal model, similar to Wang & Sheeley (1990) and Riley et al. (2001), solar

wind speed is given only as a function of the flux tube expansion factor and the distance of the foot points of the flux tube to the nearest coronal hole. This semi-empirical coronal model itself can be divided into two important magnetic field models. In the lower corona, it consists of a potential field source model (PFSS, Altschuler & Newkirk, 1969) in which the magnetic field is assumed to be current-free and is set to be purely radial at a given source surface. In the upper corona, the magnetic field is given by the Schatten current sheet model (SCH, Schatten et al., 1969) whose main purpose is to extend the magnetic field model in a nearly radial fashion and at the same time retain thin HCS. For more details on the semi-empirical coronal model, we refer the reader to Pomoell & Poedts (2018). The inner boundary of the heliospheric propagation model is at 0.1 AU, the model solves the following ideal MHD equations with gravity included:

$$\begin{aligned}\frac{\partial \rho}{\partial t} &= -\nabla \cdot (\rho \mathbf{v}) \\ \frac{\partial(\rho \mathbf{v})}{\partial t} &= -\nabla \cdot \left[\rho \mathbf{v} \mathbf{v} + \left(P + \frac{B^2}{2\mu_0} \right) \mathbf{f} - \frac{1}{\mu_0} \mathbf{B} \mathbf{B} \right] + \rho \mathbf{g} \\ \frac{\partial \mathbf{B}}{\partial t} &= \nabla \times (\mathbf{v} \times \mathbf{B}) \\ \frac{\partial E}{\partial t} &= -\nabla \cdot \left[\left(E + P - \frac{B^2}{2\mu_0} \right) \mathbf{v} + \frac{1}{\mu_0} \mathbf{B} \times (\mathbf{v} \times \mathbf{B}) \right] + \rho \mathbf{v} \times \mathbf{g}\end{aligned}$$

where, ρ , \mathbf{v} , \mathbf{B} , P are the density, velocity, magnetic field, and thermal pressure of the plasma. E is the total energy density and is given by the following equation:

$$E = \frac{P}{\gamma - 1} + \frac{1}{2} \rho v^2 + \frac{B^2}{2\mu_0}$$

where γ is the polytropic index set to 1.5. The CMEs are introduced as a time-dependent boundary condition at the inner radial boundary of the heliospheric model, at 0.1 AU. Some of the most used CME models are the CME cone model (Odstrčil & Pizzo, 1999), linear force-free spheromak model (Verbeke et al., 2019), and most recent FRi3D model (Isavnin, 2016; Maharana et al., 2022). A linear force-free spheromak is a compact toroidal plasma structure in which the magnetic field, generated by plasma currents, satisfies the condition $\mathbf{J} \times \mathbf{B} = 0$, resulting in a force-free equilibrium.

1.3 Motivation

As CMEs propagate through the heliosphere, they interact with the surrounding magnetic field and ambient solar wind plasma. This interaction involves the occurrence of the MHD waves and magnetic field draping (Cargill et al., 1996; Gosling & McComas, 1987). For fast CMEs traveling through slower ambient plasma, this interaction results in accelerations and deflections of the plasma in front of the ICME's FR part. This happens because the ambient solar wind cannot easily penetrate the magnetized FR part of the CME due to high electrical conductivity. This occurs within the CME sheath region, particularly near the FR part. The IMF draping pattern is heavily influenced by the relative velocity between the CME and the solar wind, as well as the CME's size, shape, and the configuration of the surrounding magnetic field (Gosling & McComas, 1987; McComas et al., 1988; McComas et al., 1989). Consequently, differently oriented CMEs, even if embedded in similar ambient solar wind and IMF configurations, might show different plasma flows and draping patterns.

Figure 1.8 illustrates a low-inclination CME in panel a) and a high-inclination CME in panel b) that are embedded in the surrounding magnetic field (red arrows). Only the meridional plane (the xz -plane) of the GSE coordinate system is shown, while the Parker spiral configuration of the magnetic field is considered in the xy -plane (not shown here, for reference see Figure 8 in Martinić et al., 2022). The blue arrows in Figure 1.8 schematically represent plasma flows in front of the CMEs FR part. The larger pressure gradient resulting from the pileup of magnetized solar wind enables the ambient plasma to easily bypass the obstacle in the direction where the extent of the obstacle is smaller. Consequently, for a low-inclination CME, plasma flow is expected to be more pronounced in the xz -plane of the Geocentric Solar Ecliptic (GSE) coordinate system than in a high-inclination ICME. Conversely, in a high-inclination CME, more pronounced plasma flows are expected in the yz -plane (into and out of the plane shown in Figure 1.8). The draped ambient field that follows the Parker spiral configuration eventually slides past the obstacle, following the plasma motion due to the frozen-in condition. We expect this process to be more efficient for a low-inclination CME since its extent in the xz -plane is smaller.

Vandas et al. (1995) and Vandas et al. (1996) studied the propagation of two CMEs with different inclinations represented by Lundquist's cylindrical force-free solution (Lundquist, 1950) in the inner heliosphere using the 2.5D MHD model by Wu et al. (1983). They found that the propagation of these CMEs does not depend on the inclination of their axes with respect to the ecliptic plane (one lies in the ecliptic, and the other has an axis perpendicular to it). However, it is important to note that the MHD model they used was limited to the equatorial plane of

the Sun and did not provide a comprehensive 3D MHD representation. This has recently been done by Martinić et al. (2024). Moreover, we emphasize that this inclination effect, to our best knowledge, has not been observationally studied before Martinić et al. (2022) and Martinić et al. (2023).

This research contributes to a better understanding of the draping pattern and ambient plasma flows as crucial indicators of the interaction between the magnetized CME core and ambient solar wind and magnetic field. Understanding of which is of great importance for space weather prediction improvement.

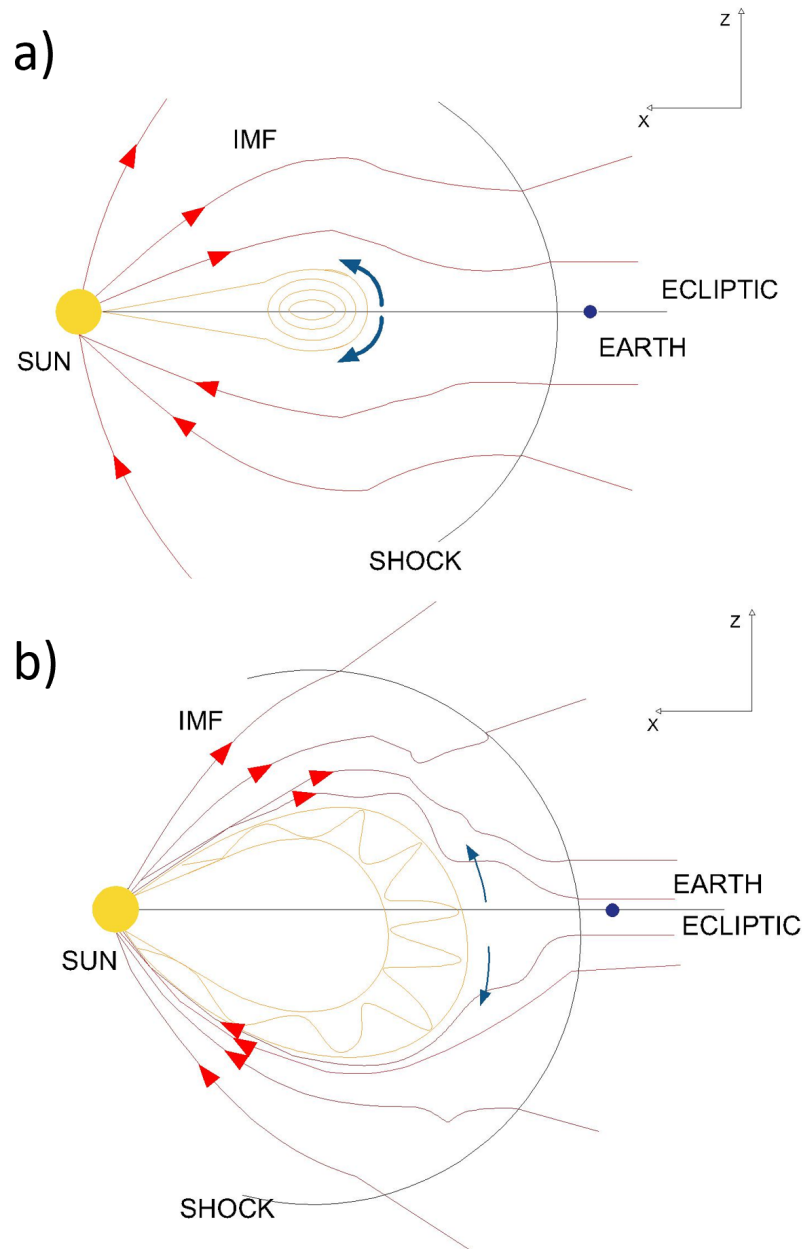


Figure 1.8: Idealized IMF in the meridional plane, xz -plane of GSE coordinate system, and its interaction with embedded ICME with low inclination (upper panel) and high inclination (bottom panel). The non-radial flows are shown with blue arrows where its width and length suggest the pronouncement of the plasma flows in front of the embedded ICME. The figure is taken from Martinić et al. (2023).

Chapter 2

Scientific Papers

2.1 Determination of coronal mass ejection orientation and consequences for their propagation

Determination of coronal mass ejection orientation and consequences for their propagation

K. Martinić¹, M. Dumbović¹, M. Temmer², A. Veronig^{2,3}, and B. Vršnak¹

¹ Hvar Observatory, Faculty of Geodesy, University of Zagreb, Zagreb, Croatia
e-mail: kmartinic@geof.hr

² Institute of Physics, University of Graz, Graz, Austria

³ Kanzelhöhe Observatory for Solar and Environmental Research, University of Graz, Graz, Austria

Received 28 February 2022 / Accepted 12 April 2022

ABSTRACT

Context. The configuration of the interplanetary magnetic field and features of the related ambient solar wind in the ecliptic and meridional plane are different. Therefore, one can expect that the orientation of the flux-rope axis of a coronal mass ejection (CME) influences the propagation of the CME itself. However, the determination of the CME orientation, especially from image data, remains a challenging task to perform.

Aim. This study aims to provide a reference to different CME orientation determination methods in the near-Sun environment. Also, it aims to investigate the non-radial flow in the sheath region of the interplanetary CME (ICME) in order to provide the first proxy to relate the ICME orientation with its propagation.

Methods. We investigated 22 isolated CME-ICME events in the period 2008–2015. We determined the CME orientation in the near-Sun environment using the following: (1) a 3D reconstruction of the CME with the graduated cylindrical shell (GCS) model applied to coronagraphic images provided by the STEREO and SOHO missions; and (2) an ellipse fitting applied to single spacecraft data from SOHO/LASCO C2 and C3 coronagraphs. In the near-Earth environment, we obtained the orientation of the corresponding ICME using in situ plasma and field data and also investigated the non-radial flow in its sheath region.

Results. The ability of GCS and ellipse fitting to determine the CME orientation is found to be limited to reliably distinguish only between the high or low inclination of the events. Most of the CME-ICME pairs under investigation were found to be characterized by a low inclination. For the majority of CME-ICME pairs, we obtain consistent estimations of the tilt from remote and in situ data. The observed non-radial flows in the sheath region show a greater y direction to z direction flow ratio for high-inclination events, indicating that the CME orientation could have an impact on the CME propagation.

Key words. Sun: coronal mass ejections (CMEs) – magnetohydrodynamics (MHD) – Sun: heliosphere

1. Introduction

Coronal mass ejections (CMEs) are expulsions of magnetic field and plasma from the solar atmosphere into the interplanetary medium. They are known as the main drivers of geomagnetic storms and can cause great damage in the near-Earth environment (Zhang et al. 2003). After a certain distance from the solar surface, the CME dynamics becomes mostly governed by magneto-hydrodynamic “aerodynamic” drag (Cargill et al. 1996; Vršnak 2001). This means that CMEs slower than the ambient solar wind are accelerated, while the ones that are faster than the ambient solar wind are decelerated. More recent work on this subject is given by Temmer et al. (2011), Vršnak et al. (2013), and Sachdeva et al. (2015).

Coronal mass ejections can be observed remotely using white-light coronagraphs. Coronagraphs situated at different vantage points provide a stereoscopic view and 3D reconstruction of the CME. The graduated cylindrical shell (GCS) model was developed by Thernisien et al. (2006) to perform 3D reconstructions of the CMEs using white-light images from coronagraphs on-board the SOHO and STEREO missions. In the GCS model, the flux-rope (FR) structure is represented with a croissant-like shape that consists of two segments: conical legs and a curved front. Conversely, the cross section of the croissant is circular. Each CME is fully defined by six GCS parameters, these are as follows: (1) the longitude of the apex; (2) the latitude

of the apex; (3) the height of the apex; (4) the half-angle, that is a measure of the distance from the leg’s central axis to the apex; (5) the aspect ratio, in other words the measure of the width of the leg; and (6) the tilt, that is the inclination of the FR axis with respect to the solar equator. The GCS implementation for the 3D CME reconstruction as described in Thernisien (2011) has been widely used (e.g., Temmer et al. 2021; Singh et al. 2018; Shi et al. 2015). The orientation of the CME can be obtained using a 2D geometry as well. Chen et al. (1997) suggested that an ellipse can be used to characterize a two-dimensional projection of the CME FR. This was later applied by Krall & St. Cyr (2006) and Byrne et al. (2009), for example, who characterized the observed CME front with an ellipse. By changing the ellipse’s position, axes’ length, and tilt, one derives the CME angular width and inclination. To our knowledge, a comparison of the results for CME inclination obtained by these two methods has not been investigated yet.

When crossing the spacecraft, interplanetary coronal mass ejections (ICMEs) show specific signatures. Often a characteristic three-part structure can be observed: shock, sheath, and ejecta/magnetic cloud (MC). The shock arrival is characterized by a sudden increase in the magnetic field, solar wind speed, and temperature. The sheath region is characterized by high turbulence, dense hot plasma of the ambient solar wind, and an interplanetary magnetic field that is compressed and draped around the FR part of the ICME. Also, the sheath region typically

shows higher fluctuations in all measured parameters and a smaller radial extension than in the FR part of the ICME (Kilpua et al. 2017). The sheath region in addition shows evidence of non-radial flows (NRFs). Gosling & McComas (1987) detected a systematic westward flow in the sheath region and concluded that it is due to the magnetic stress of the Parker spiral acting on the west flank of the ICMEs. Later, Owens & Cargill (2004) investigated five MCs with relatively uncomplicated upstream NRFs. They found that the deflected flows are more or less parallel to the surface of the MC and that they can be used as a proxy for the local axis orientation and the point of interception of the spacecraft with the ICME. More recently, Al-Haddad et al. (2021) performed a statistical research that was focused on NRFs throughout the first 13 years of the STEREO mission. They found that the majority of NRFs are associated with CMEs and that the largest NRFs inside the CME are related to deflections in the sheath region.

Following the sheath, in situ spacecraft detect the ejected magnetic structure, which occasionally shows clear FR properties. These “magnetic clouds” were first described by Burlaga et al. (1981) and Klein & Burlaga (1982), and they are characterized by an enhanced and smoothly rotating magnetic field, a depressed proton temperature, and a decreased plasma beta. It has been shown that approximately only one-third of ICMEs show these in situ signatures (Gosling 1990; Cane & Richardson 2003). In the first approximation, we can describe the FR part of an ICME as a cylindrical tube that contains a helical magnetic field component which wraps around the tube’s central axis and an axial field component which follows the tube’s central axis (Lundquist 1950). FRs can have left-handed or right-handed chirality depending on the relative orientation of the helical magnetic field to the axial magnetic field. Inclination and chirality allows us to classify each FR as one of eight basic types (Mulligan et al. 1998; Bothmer & Schwenn 1998; Palmerio et al. 2018).

In this study, we analyze the CME orientation obtained by different methods using remote and in situ measurements and the possible impact it could have on the CME propagation. The properties of the interplanetary magnetic field (IMF) and related ambient solar wind differ in the ecliptic and meridional planes (Schwenn 2006). CMEs can have inclinations from extremely low (the ones that lie in the ecliptic plane), to extremely high (the ones that lie in the meridional plane). Consequently, it is reasonable to assume that the interaction of the CME and ambient solar wind are conditioned by the CME’s inclination. Non-radial flows in the sheath region are a result of the CME interaction with the ambient solar wind and thus they could indicate different interactions depending on the inclination of the CME propagating through the interplanetary space. The connection between CME inclination and propagation was studied by Vandas et al. (1995, 1996). They performed simulations of magnetic cloud propagation in the inner heliosphere for a high inclination magnetic cloud in the ecliptic plane and for a low inclination magnetic cloud in the meridional plane. They found no significant time arrival difference in these two cases. However, they did not study the propagation of a high inclination magnetic cloud in the meridional plane and a low inclination magnetic cloud in the ecliptic plane.

2. Data and method

We analyzed CME-ICME orientation using remote and in situ observations. For that purpose, we compiled a list of reliably associated CME-ICME pairs. In order to derive the FR type

from the in situ data, we analyzed only the events with a clear MC signature. Moreover, we analyzed only the events that had been remotely observed from at least two vantage points. We performed GCS and ellipse fit analysis only to those events with clearly seen fronts and where image artifacts and/or bright streamers did not affect the front determination.

We searched for associated CME-ICME pairs in Palmerio et al. (2018) for period 2010–2013, in Maričić et al. (2020) for period 2010–2015, in Temmer et al. (2021) for period 2008–2015, and in Nitta & Mulligan Skov (2017) for period 2010–2016. Altogether, we investigated 63 associated CME-ICME pairs in the time period 2008–2016. Events showing complex (non-MC) in situ signatures that had an unclear CME-ICME association or uncertain GCS reconstruction were discarded. The remaining 22 events have a clear CME-ICME association, clear MC signatures, and the GCS reconstruction was performed with at least two vantage points, that is to say using at least two spacecraft. We note that the majority of the remaining events have a latitude and longitude within $\pm 30^\circ$ from the center of the solar disk as obtained by GCS. This, along with a clear MC structure observed in situ, indicates a nose hit (Maričić et al. 2020).

The associated CMEs were analyzed in white light observations from the SOHO/LASCO (Brueckner et al. 1995) C2 and C3 coronagraphs, STEREO-A(ST-A)/SECCHI, and STEREO-B(ST-B)/SECCHI (Howard et al. 2008) COR1 and COR2 coronagraphs. In situ data were provided by the OMNI database (King & Papitashvili 2005). The CME orientation was determined using remote observations and two different methods (Sects. 2.1.1 and 2.1.2), whereas the ICME orientation was determined using in situ measurements (Sect. 2.2). Finally, we used in situ measurements to determine the NRFs in the sheath region (Sect. 2.3).

2.1. Tilt determination in the near-Sun environment

2.1.1. Graduated cylindrical shell model

We first estimated the CME orientation by performing a 3D FR reconstruction using the GCS model (Thernisien et al. 2006). We used low coronal signatures to better constrain the latitude, longitude, and tilt of the CME. We used JHelioviewer (Müller et al. 2017) as a visualization tool to analyze 171, 211, 193, and 304 Å filtergrams from SDO/AIA (Lemen et al. 2012) and SDO/HMI (Scherrer et al. 2012) magnetogram data; additionally, when SDO/AIA and/or SDO/HMI data were not available, we used all (E)UV filters from SOHO/EIT (Delaboudinière et al. 1995) and SOHO/MDI (Scherrer et al. 1995) magnetogram data. We searched for post-flare loops (PFLs) whose orientation suggests the orientation of the FR (Palmerio et al. 2018; Yurchyshyn 2008). Also, we searched for coronal dimmings, sigmoids, and flare ribbons which are known as “by-eye” indicators of the polarity inversion line (PIL) whose orientation roughly matches the orientation of the FR (Palmerio et al. 2018; Marubashi et al. 2015; Möstl et al. 2008). In the case of the quiet Sun eruptions, we searched the position and orientation of the corresponding erupting filament.

An example of how we constrained the latitude, longitude, and tilt of the CME that occurred on 3 April 2010 is shown in Fig. 1. The pre-eruption SOHO/EIT 195 Å filtergram, as well as SOHO/MDI, are shown. The active region AR 11059 is marked by the red rectangle on the solar disk as a source of the eruption (Lat $\approx -18^\circ$ and Lon $\approx 3^\circ$). In Fig. 1 we also see that the EUV post-flare loops and the PIL in the magnetogram suggest a high-inclination FR as indicated by the red lines determined “by eye”.

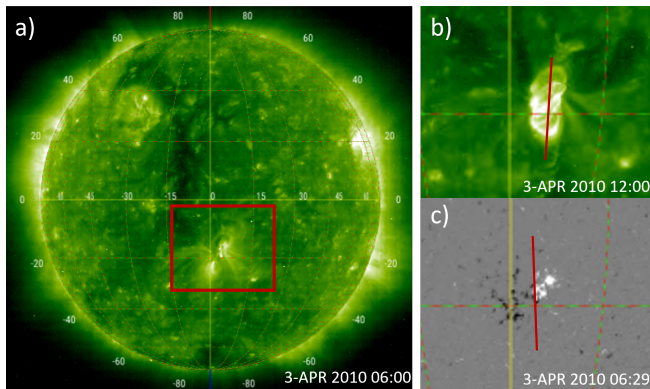


Fig. 1. Source region, magnetogram, and low coronal signatures of a CME that occurred on 3 April 2010. *Panel a:* Source of the eruption (AR 11059) as seen by SOHO/EIT 195 Å just before the eruption. *Panel b:* Zoomed-in region indicated by the red rectangle in panel a, showing post flare loops observed by SOHO/EIT 195 Å. *Panel c:* Same zoomed-in region showing the SOHO/MDI magnetogram. Red lines show tilt estimation.

We performed GCS reconstruction only for the events for which coronagraphic images were available from at least two different vantage points. We reconstructed each event for at least four different heights (i.e., at different times), starting with the lowest heights using coronagraphs COR1-A (STEREO-A), COR1-B (STEREO-B), and C2 (SOHO). We ended the reconstruction at the altitude corresponding to the image of the CME where the front of the FR was last seen unambiguously, using coronagraphs COR2-A (STEREO-A), COR2-B (STEREO-B), and C3 (SOHO).

Figure 2 shows the GCS reconstruction (yellow mesh) for event 2 from the list (Table 1, the CME occurred on 3 April 2010). This is an example of a low inclination event and the GCS reconstruction was obtained using coronagraphic images from three different vantage points.

We see that the inclination derived from GCS greatly differs from the inclination estimated from post-flare loops and magnetogram for the same event. This is not unusual since the evidence for rotation and deflection in the low and middle corona has been presented many times (Fan & Gibson 2004; Green et al. 2007; Lynch et al. 2009; Vourlidis et al. 2011; Kay et al. 2017). However, it is beyond the scope of our study to further analyze possible rotations of each event. We emphasize once more that the priority was given to the GCS-obtained inclination and that orientation estimation with low coronal signatures and magnetogram data was taken only as a possible constraint.

2.1.2. Ellipse fit

The projection of an Earth-directed, GCS-obtained croissant, in the yz plane (Earth view) of the Heliocentric Earth Equatorial (HEEQ) coordinate system can be approximated with an ellipse. An example of the ellipse approximation of the GCS-obtained croissant of the event that occurred on 3 April 2010 is shown with the red-colored ellipse in Fig. 3. Led by this idea, we performed the ellipse fit on data provided by C2 and C3 coronagraphs on board the SOHO spacecraft. The front of each Earth-directed CME observed with C2 and C3 coronagraphs are represented with an ellipse and the inclination of the ellipse's major axis to the equator is taken as the CME tilt.

Figure 4 shows the ellipse fit results for the same event that is shown in Figs. 2 and 3. The panel on the left (Fig. 4) shows

the ellipse fit obtained with LASCO(C2) at the same time as the GCS reconstruction. The panel on the right (Fig. 4) shows the ellipse fit obtained with LASCO(C3) for the same event, but at a later time. It is important to note that the relative size of the occulting disk compared to the overall size of the observed structure (CME) may influence the ellipse fitting. The greater the size of the occulting disk of the coronagraph compared to the size of the CME, the harder it is to perform the fit. Understandably, this is more pronounced when doing the ellipse fit with the LASCO(C2) than with the LASCO(C3) images. On the other hand, the CME front for some events becomes faint in the C3 field of view (FOV) and thus is more difficult and unreliable to fit. Therefore, we performed an ellipse fit using both C2 and C3 data. The robustness of two different methods applied to different data sets used to determine the tilt in the near-Sun environment (GCS, ellipse-C2, and ellipse-C3) is presented and discussed in Sect. 3.

It is worth emphasizing that we did not introduce the ellipse fit method in order to increase the reliability of the GCS reconstruction, but rather to compare the results of the two methods. GCS and the ellipse fit both use morphological features of a CME for the reconstruction, but GCS uses a 3D geometry (croissant) whereas the ellipse fit uses a 2D geometry (ellipse). Thus, we can not a priori know whether the methods will give similar tilt results. The main motivation for testing this is to provide a reference for future work so that we can study a larger statistical sample of CME-ICME associations by searching through the whole SOHO era.

2.2. Tilt determination in the near-Earth environment

As a next step, we determined the tilt of the ICME in the near-Earth environment using in situ data obtained from the WIND and ACE spacecraft and provided through the OMNI database (King & Papitashvili 2005). First, we determined the ICME and MC boundaries. In order to achieve consistency as the main criterion for ICME arrival, we used the sudden increase in the magnetic field, density, temperature, and velocity to mark the ICME shock or sheath arrival. To consistently determine MC boundaries, we used magnetic field smooth rotation as the main criteria for all studied events. The determined end of the MC was taken as the end of the ICME as well.

We determined if the event is dominantly high or low inclined from its characteristic in situ signatures. FRs that have their central axis more or less parallel to the ecliptic plane are called low-inclination FRs (the B_z component represents the helical field and thus its sign changes as the FR is crossed). FRs that have their central axis more or less perpendicular to the ecliptic plane are called high-inclination FRs (the B_z component represents the axial field and thus its sign does not change as the FR is crossed, see e.g., Palmerio et al. 2018). Early work by Mulligan et al. (1998) and Bothmer & Schwenn (1998) suggested the existence of eight different types of the magnetic FR with different magnetic configurations of MCs which can be observed during the cloud's passage. The FR-type determination in the near-Earth environment according to the abovementioned "eight-type" classification also allows us to distinguish between a high (ESW, ENW, WSE, and WNE) and low (NES, NWS, SEN, and SWN) inclination. The determination of 22 observed events according to this eight-type classification is shown in the last column of Table 2.

We note that this classification of a FR only provides us with information on whether it has high or low inclination. There are various FR reconstruction methods one could apply to in situ

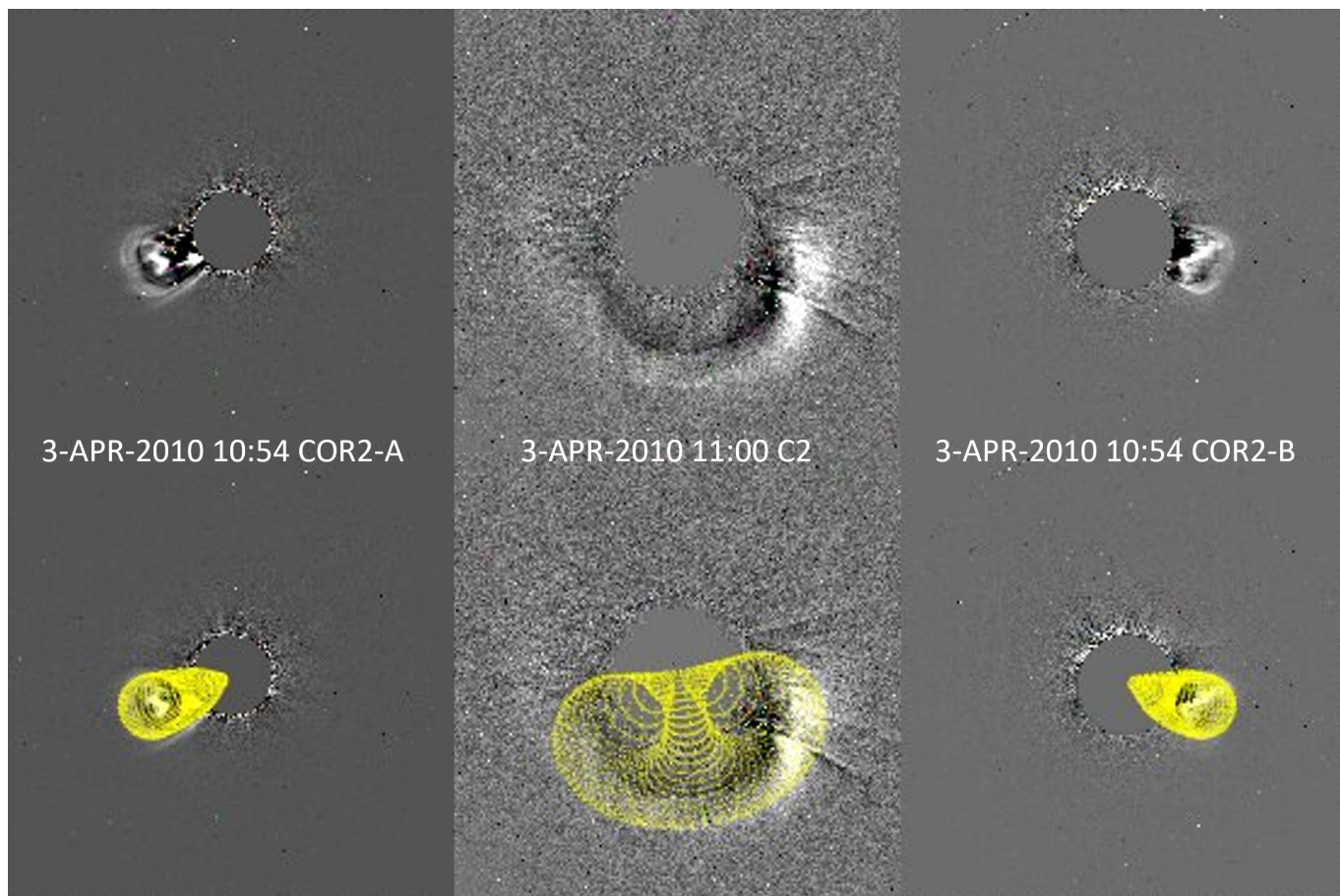


Fig. 2. CME that occurred on 3 April 2010. The *upper panel* shows the running difference images in STEREO(COR2) and SOHO(LASCO-C2), while in the *bottom panel* the GCS reconstruction is superposed (yellow wire).

data to obtain the value of the FR tilt. However, it was shown by Al-Haddad et al. (2013) that the determination of the value of the FR tilt can be quite unreliable. They performed four different reconstruction and fitting methods on 59 ICMEs observed in situ. All four methods gave an orientation of the FR axis within $\pm 45^\circ$ for only one event. They also found that other results, besides inclination, obtained with different techniques usually did not match. Therefore, we constrained our estimation to high and low inclination from the in situ data for each event.

Figure 5 shows the same CME that was launched from the Sun on 3 April 2010, as seen two days later in the in situ data. This event was classified as a low inclined event due to clear rotation of the B_z component in the marked MC region.

2.3. Non-radial flows in the sheath region

We analyzed NRFs in the sheath region of the in situ observed ICMEs. One would expect NRFs to be locally, approximately parallel to the surface of the ICME, thus the properties of the NRFs should reflect the ICME geometry (Owens & Cargill 2004). Since we considered only CME-ICME pairs that were approximate nose hits, we might expect low inclined ICMEs to have more pronounced NRFs in the $\pm z$ direction of the GSE coordinate system in comparison to high inclined ICMEs. We derived the NRFs in the z direction and y direction of the GSE coordinate system by calculating the average values of v_z and v_y absolute values in the sheath region, respectively. In order to test the hypothesis that low inclined events have more profound

flows in the z direction, we define the NRF ratio θ as follows:

$$\theta = \frac{\overline{|v_y|}}{\overline{|v_z|}},$$

where $\overline{|v_y|}$ and $\overline{|v_z|}$ are the mean values of the magnitude of the velocity in the sheath region in the y direction and z direction, respectively.

3. Results and discussion

Table 1 lists 22 events and the results of the GCS reconstruction: longitude, latitude, tilt, aspect ratio, and half-angle. The first column shows the ordinal number of the event and the upper index indicates from which CME-ICME list the association was taken; P stands for Palmerio et al. (2018), M stands for Maričić et al. (2020), T stands for Temmer et al. (2021), and N stands for Nitta & Mulligan Skov (2017). The second column shows the time when the GCS reconstruction was performed.

Due to the subjectiveness of the GCS reconstruction, we compared these results to the tilt results obtained using GCS by Temmer et al. (2021), Sachdeva (2019), and the HELCATS catalog¹, shown in Table 2. Also, in Table 2 the tilt results obtained by the ellipse fitting performed on coronagraphic images provided by the SOHO/LASCO C2 and C3 mission are shown. Events 5, 14, 16, and 18 have very faint leading-edge fronts in

¹ https://www.helcats-fp7.eu/catalogues/wp3_kincat.html

Table 1. Results of the GCS modeling.

NO	Reconstruction time	Long [°]	Lat [°]	Tilt [°]	Height [R_s]	Aspect ratio	Half-angle [°]
1 ^T	2008-12-12 11:54	0	6	38	11.8	0.28	18
2 ^{M,T}	2010-04-03 10:55	5	-26	10	7.7	0.35	30
3 ^P	2010-05-23 21:54	0	5	35	12.1	0.27	21
4 ^{T,N}	2010-06-16 19:24	351	5	-23	10.8	0.29	17
5 ^{T,N}	2011-01-30 17:39	0	-17	0	10.9	0.35	30
6 ^{P,M,N}	2011-03-25 10:39	333	-3	-23	6.6	0.21	17
7 ^N	2011-05-25 13:54	3	9	58	9.2	0.13	13
8 ^{P,T}	2011-06-02 08:39	352	-5	17	7.3	0.35	30
9 ^{P,M,T}	2011-09-14 01:24	17	22	-36	7.8	0.34	25
10 ^{P,T}	2012-01-19 15:10	323	48	90	3.9	0.32	29
11 ^{P,M}	2012-05-12 00:48	330	-8	90	10.1	0.27	18
12 ^{P,M,T}	2012-06-14 14:08	0	-20	38	4.2	0.31	18
13 ^{P,T,N}	2012-10-05 07:24	12	-14	46	14.9	0.24	31
14 ^P	2012-10-09 07:39	1	5	4	13.7	0.32	29
15 ^T	2012-11-09 16:24	356	-13	19	9.1	0.33	30
16 ^P	2013-01-13 15:54	1	-1	-6	12.4	0.34	11
17 ^{P,M,T}	2013-04-11 08:24	343	-7	66	9.0	0.30	21
18 ^N	2013-06-02 22:54	0	-3	12	12.1	0.35	28
19 ^{P,M,T}	2013-07-09 15:12	1	2	0	12.3	0.46	31
20 ^{M,T}	2013-09-29 22:39	7	27	-67	6.6	0.32	34
21 ^{P,T}	2014-08-15 17:48	9	15	-52	12.7	0.22	20
22 ^N	2016-10-09 04:54	0	10	-23	8.9	0.35	31

Notes. We provide the event number with an indication from where the CME-ICME association was taken, reconstruction time, Stonyhurst longitude, latitude, CME tilt, aspect ratio, and half-angle.

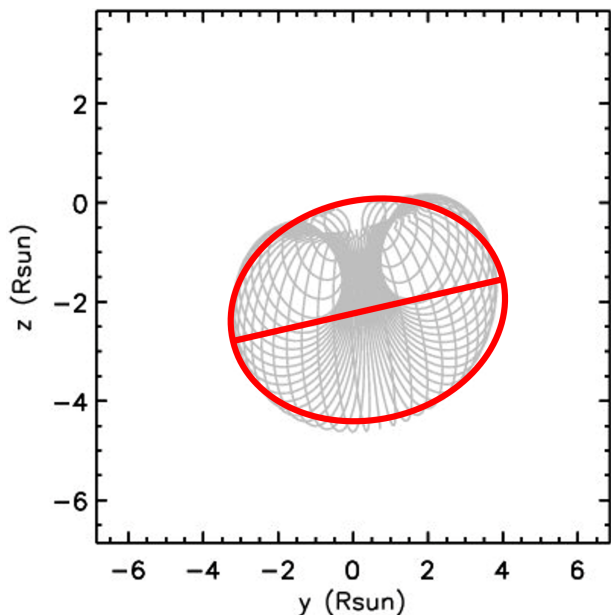


Fig. 3. Projection of the GCS croissant of the 3 April 2010 CME in the yz plane of the Heliocentric Earth Equatorial (HEEQ) coordinate system (i.e., Earth view). A possible ellipse representation is marked by the red line along with the ellipse's major axis.

the C2 and C3 FOV, so the GCS reconstruction was obtained only using STEREO-A and STEREO-B data, and the ellipse fit was not performed at all. Events 4, 6, 7, 19, and 22 lost the clear leading edge front from the C2 to C3 FOV, so we were not able to perform the ellipse fitting on C3 coronagraphic images.

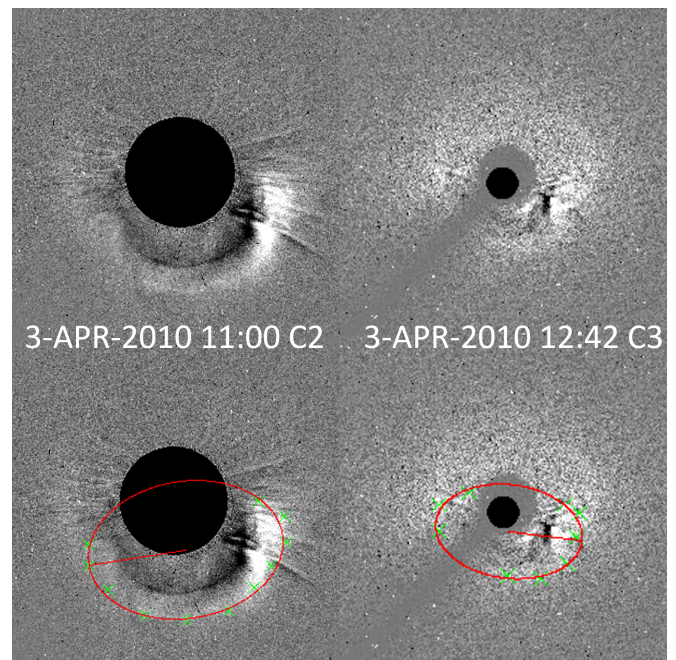


Fig. 4. CME that occurred on 3 April 2010. The *upper panel* shows the running difference images in SOHO (LASCO-C2 and LASCO-C3). The *bottom left panel* shows the results of the ellipse C2 fitting at the same time when the GCS was performed. The *bottom right panel* shows the results of the ellipse fitting when using data from C3. The ellipse is represented with the red line and green crosses mark the points outlined on the CME front used to obtain the fit.

From Table 1 we can see that there are 50% more low than high inclined events in the near-Sun environment. From Table 2

Table 2. Comparison of CME tilt results from different techniques and studies.

NO	GCS	Ellipse C2	Ellipse C3	Temmer+2021	Sachdeva PHD	HELcats
1 ^T	38°(L)	19°(L)	-23°(L)	51°(H)	/	51°(H)
2 ^{M,T}	10°(L)	20°(L)	-7°(L)	2°(L)	22°(L)	/
3 ^P	35°(L)	27°(L)	29°(L)	/	/	-10°(L)
4 ^{T,N}	-23°(L)	19°(L)	/	-55°(H)	-15°(L)	-8°(L)
5 ^{T,N}	0°(L)	/	/	-20°(L)	/	-20°(L)
6 ^{P,M,N}	-23°(L)	19°(L)	/	/	9°(L)	0°(L)
7 ^N	58°(H)	50°(L/H)	/	/	/	/
8 ^{P,T}	17°(L)	-49°(L/H)	-19°(L)	-55°(H)	/	55°(H)
9 ^{P,M,T}	-36°(L)	-32°(L)	-39°(L)	-6°(L)	/	-6°(L)
10 ^{P,T}	90°(H)	-22°(L)	-43°(L/H)	90°(H)	90°(H)	/
11 ^{P,M}	90°(H)	-14°(L)	-21°(L)	/	/	/
12 ^{P,M,T}	38°(L)	26°(L)	30°(L)	67°(H)	-87°(H)	/
13 ^{P,T,N}	46°(L/H)	45°(L/H)	72°(H)	41°(L/H)	37°(L)	54°(H)
14 ^P	4°(L)	/	/	/	/	/
15 ^T	19°(L)	31°(L)	22°(L)	6°(L)	7°(L)	22°(L)
16 ^P	-6°(L)	/	/	/	/	/
17 ^{P,M,T}	66°(H)	-37°(L)	41°(L/H)	66°(H)	90°(H)	/
18 ^N	12°(L)	/	/	/	/	/
19 ^{P,M,T}	0°(L)	15°(L)	/	/	/	/
20 ^{M,T}	-67°(H)	-54°(H)	-66°(H)	90°(H)	90°(H)	-67°(H)
21 ^{P,T}	-52°(H)	-40°(L/H)	-44°(L/H)	/	/	/
22 ^N	-23°(L)	-25°(L)	/	-23°(L)	/	/

Notes. The first column shows the event number with indications wherefrom the CME-ICME association was taken. Next are the results for the tilt obtained by GCS (same as in Table 1), ellipse fit C2 tilt results, ellipse fit C3 tilt results, tilt results from Temmer et al. (2021), tilt results from Sachdeva (2019), and tilt results from the HELcats catalog². We note that *L* stands for a low inclination result, *H* stands for a high inclination result, and *L/H* stand for a tilt result that could be considered low and high.

it is obvious that different methods give different results for the same event and we cannot say that a certain event has a certain tilt. In order to at least conclude as to whether an event is dominantly low or high inclined, we added an *L(H)* mark near each tilt result presented in Table 2. We note that *L* was given for results $\tau \in [\pm 0^\circ, \pm 44^\circ]$ and *H* was given for results $\tau \in [\pm 45^\circ, \pm 90^\circ]$. The events with $\tau \in [\pm 40^\circ, \pm 50^\circ]$ are indicated as *L/H* because those could be considered as both high and low inclined.

From now on, the results obtained with different methods that are the same in terms of high and low inclination are referred to as “consistent” results. We also emphasize that events marked as *H/L* for a certain method were not taken into account for the statistics as either high or low inclination events. When comparing our GCS tilt result with C2- and C3-ellipse fitting, we see that for seven out of 13 events (54%) for which we were able to perform GCS, ellipse-C2, and ellipse-C3 fitting methods, the obtained tilt was consistent. Moreover, the GCS and C2-ellipse fit gave consistent results for 12 out of 18 events (67%). When comparing the GCS and C3-ellipse fit, we obtained consistent results for eight out of 13 events (62%). We note that C2- and C3-ellipse fitting gave consistent results for nine out of 13 events (70%). In regards to a comparison between our results, GCS results, those of Temmer et al. (2021) as well as Sachdeva (2019), and the HELcats catalog³, we see that in 11 out of 15 (73%) events our GCS results were consistent with the majority of the studies listed above. In four out of 15 (27%) events, our GCS results differed from the majority of other research results listed in Table 2, again in the scope of high and low inclination.

³ https://www.helcats-fp7.eu/catalogues/wp3_kincat.html

To summarize, we see that in the majority of events, the C2- and C3-ellipse fit provide the same results. Also, the majority of these C2- and C3-ellipse fit results are in agreement with the GCS results. However, the methods are robust only in the scope of determining whether a certain event has either a high or low inclination, but not in terms of a specific value.

When determining the FR type using the magnetic field components’ rotation from in situ data, we found that the majority of events have a low inclination (see Table 3). Only eight out of 22 events (36%) were considered as high inclined.

When comparing the results for inclination derived with GCS (Table 2) and the results for inclination from in situ data (Table 3), we found that 14 out of 22 (63%) events have a consistent tilt estimation from remote and in situ measurements. We also see that there are slightly more events that were classified as low inclined from remote observations and as high inclined from in situ data (18%) than vice versa (14%). This is in agreement with the results from Xie et al. (2021). They compared the orientations of 102 CMEs at a near-Sun environment obtained from the EFR model (Krall & St. Cyr 2006) with the orientations obtained at L1 using a simple cylindrical force-free FR model. They found that only 25% of the studied events show rotations greater than 40° and that the majority of these rotational events occurred within the COR2 FOV, that is to say the middle corona.

As stated above, nearly one-third of the events under study have an inconsistent inclination as derived remotely (GCS) and in situ. We identify four possible reasons for this: (1) wrong association; (2) wrong tilt estimation remote; (3) wrong tilt estimation in situ; and (4) real tilt angle change during propagation (outside of the COR2 FOV).

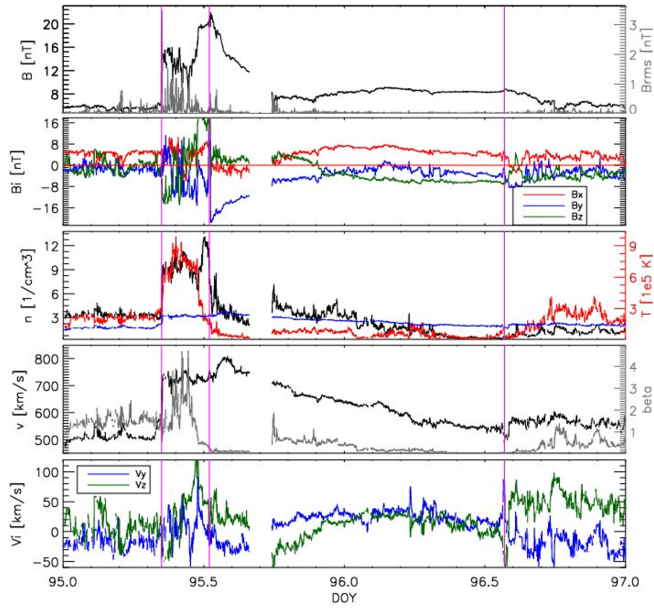


Fig. 5. ICME observed in situ measurements on 5 April 2010. The parameters shown, *from top to bottom*, are the magnetic field magnitude (black) and magnetic field fluctuations (gray); magnetic field components in the GSE coordinate system (red, B_x ; blue, B_y ; green, B_z); the proton density (black) and temperature (red) along with the calculated expected temperature (blue); the solar wind speed (black) and plasma beta (gray); and finally the y (blue) and z (green) velocity component in the GSE coordinate system. The vertical magenta lines indicate, from left to right, shock-sheath arrival, the leading edge of the MC, and finally the trailing edge of the MC which is the same as the end of the whole ICME.

During the event selection, we took care to consider only events with good CME-ICME associations, so this is unlikely to be the cause of the inconsistency. The intrinsic features of methods for tilt determination come into question as well, especially the difference between remote sensing and in situ tilt determination. Namely, we are looking at the global structure of the CME remotely, while in situ we can see only local features of the FR across the spacecraft crossing line. Furthermore, it has been shown that CME rotations occur frequently during the eruption and in the first few solar radii of the CME propagation (Fan & Gibson 2004; Green et al. 2007; Lynch et al. 2009; Vourlidis et al. 2011; Kay et al. 2017), but some authors have also presented evidence of CME rotation outside of the corona (Isavnin et al. 2014). From this perspective, we can conclude that rotations in interplanetary space are possible, but not very likely. However, it is beyond the scope of this study to explain the tilt inconsistency as seen remotely and in situ.

The bar chart in Fig. 6 shows how many high and low inclination events were observed using the GCS model in the near-Sun environment, how many high and low incline events were observed using in situ data in the near-Earth environment, and how many events have consistently measured low and high tilts in both remote and in situ measurements. We found that in all three cases, the majority of events are characterized by a low inclination.

The calculated NRF ratio θ for each event is given in the last column of Table 4. Figure 7 shows the relative number of events (i.e., occurrence frequency) separately for high (orange) and low (blue) inclination events, with respect to the calculated θ ratios. We can see that the majority of events have a θ ratio close to 1, regardless of inclination. However, we can also see that the

frequency for small θ ratios ($\theta < 0.75$) is higher for low inclination events, more precisely there is no high inclination event with a θ ratio smaller than 0.75. Also, the frequency for high θ ratios ($\theta > 1.25$) is higher for high inclination events. This indicates that NRFs in the sheath region are more pronounced in the $\pm y$ direction for high inclination events and that NRFs are more pronounced in the $\pm z$ direction for low inclination events. We calculated the mean value, the standard deviation, the median, and the 95% percentiles of the θ ratios separately for low and high inclined events. The results are presented in Table 4. We can see that the calculated mean and median are slightly higher for high inclination events; however, we cannot confirm the statistical significance due to the very low number of high inclination events.

Nevertheless, there is an indication that in the sheath region NRFs might be more pronounced in the $\pm y$ direction for high inclination events, whereas for low inclination events they are more pronounced in the $\pm z$ direction. This asymmetry could have an implication for the CME propagation. Namely the difference in NRF flows indicates a difference in the pileup and draping of the IMF for differently oriented CMEs, which is directly related to the MHD drag. This concept is presented in Fig. 8 and is based on the previous work by Gosling & McComas (1987).

Gosling & McComas (1987) argued that the IMF draping around CMEs should depend on the CME size and shape and that it can result in the enhancement of the out-of-ecliptic component (B_z) at the expense of the ecliptic components (B_x and B_y). To visualize the complex 3D draping of the IMF, they considered the IMF draping in the ecliptic and out-of-ecliptic (meridional) planes separately using simplified IMF configurations of a spiral and dipole (i.e., purely radial IMF), respectively (see top panels of Fig. 8). We expand on this interpretation by including the CME orientation. Assuming that the CME geometry can be represented as that of a toroidal FR, the shape and size of the CME front is expected to be different in the ecliptic and meridional planes and also depend on the FR orientation. This is shown in the middle and bottom panels of Fig. 8.

In each panel of Fig. 8, the yx plane represents the meridional plane, whereas the xz plane represents the ecliptic plane. The viewing plane is marked in the upper right corner of each panel. The top panels in Fig. 8 show the idealized configuration of the IMF (red arrows) in the ecliptic (left) and meridional (right) plane. The middle panels show a low inclination CME embedded in an idealized IMF in the ecliptic (left) and meridional (right) plane. The bottom panels show a high inclination CME embedded in an idealized IMF, again, in the ecliptic (left) and meridional (right) plane. The blue arrows in the middle and bottom panels mark the direction of the deflection of the ambient plasma away from the path of the CME in the east-west and north-south direction for ecliptic and meridional planes, respectively.

Fast CMEs interact with the ambient solar wind plasma and the IMF as they propagate. A slower moving ambient plasma ahead of the CME is accelerated and deflected from its path. Assuming a toroidal shape for the FR, its leading surface is characterized by two curvatures: (1) an axial curvature due to the rooting of the footpoints of the CME at the Sun; and (2) a cross-sectional curvature due to its internal magnetic field structure. Axial curvature is greater in extent which means it has smaller curvature radii in comparison to the cross-sectional curvature which is smaller in extent and has greater curvature radii. The ambient plasma is expected to be more easily deflected via cross-sectional curvature due to its smaller extent (greater curvature radii) in comparison to the axial curvature. For better

Table 3. Results of the in situ event determination are listed.

NO	LE date	LE DOY	MC DOY	TE DOY	FR type	Inclination	θ
1 ^T	2008-12-16	351.48	352.13	352.8	NWS	<i>L</i>	1.27
2 ^{M,T}	2010-04-05	95.35	95.52	96.57	NWS	<i>L</i>	0.4
3 ^P	2010-05-28	148.11	148.85	149.7	WSE	<i>H</i>	1.01
4 ^{T,N}	2010-06-20	171.95	172.35	173.7	NES	<i>L</i>	1.76
5 ^{T,N}	2011-02-04	35.2	35.58	35.82	NES	<i>L</i>	0.44
6 ^{P,M,N}	2011-03-29	88.4	89.01	91.4	NES	<i>L</i>	2.36
7 ^N	2011-05-28	147.69	148.28	148.88	SWN	<i>L</i>	1.04
8 ^{P,T}	2011-06-05	155.85	156.05	156.8	WNE	<i>H</i>	0.97
9 ^{P,M,T}	2011-09-17	260.15	260.69	261.49	SEN	<i>L</i>	0.89
10 ^{P,T}	2012-01-22	22.25	22.52	22.77	NWS	<i>L</i>	0.87
11 ^{P,M}	2012-05-16	137.5	137.75	138.75	SWN	<i>L</i>	0.57
12 ^{P,M,T}	2012-06-16	168.5	169.05	169.51	NES	<i>L</i>	1.12
13 ^{P,T,N}	2012-10-08	282.22	282.8	283.35	ESW	<i>H</i>	1.83
14 ^P	2012-10-12	286.4	286.7	387.43	WSE	<i>H</i>	1.13
15 ^T	2013-11-12	317.95	318.4	319.15	NES	<i>L</i>	0.66
16 ^P	2013-01-17	17	17.71	15.8	SWN	<i>L</i>	0.58
17 ^{P,M,T}	2013-04-13	103.95	104.75	105.8	ENW	<i>H</i>	2.5
18 ^N	2013-06-06	157.1	157.96	159	WSE	<i>H</i>	1.08
19 ^{P,M,T}	2013-07-12	193.65	194.25	195.35	NWS	<i>L</i>	1.1
20 ^{M,T}	2013-10-02	275.07	275.96	276.95	ENW	<i>H</i>	0.78
21 ^{P,T}	2014-08-19	231.3	231.85	233	WNE	<i>H</i>	0.96
22 ^N	2016-10-12	286.92	287.25	288.62	SEN	<i>L</i>	1.21

Notes. From left to right, the table shows the following: leading-edge (LE) date appearance, LE day of the year (DOY) time appearance, MC DOY time appearance, trailing-edge (TE) DOY time appearance, flux-rope (FR) type, and the classification according to the tilt of the event.

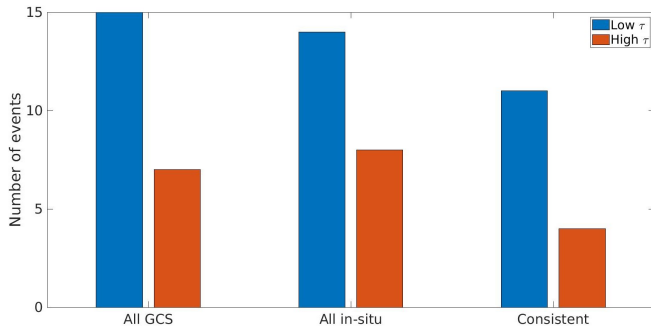


Fig. 6. Depiction of how many high and low inclination events were observed using the GCS model in the near-Sun environment, how many high and low inclination events were observed using in situ data in the near-Earth environment, and how many consistent events were classified as low and high inclination.

understanding, we can draw an analogy with a ship on the water. Namely, the front part of every ship is very small in extent, and this is to allow the water in front of the ship to flow more easily around it.

Under the assumption that the IMF is “frozen” in the ambient solar wind, a draping of the IMF occurs. IMF draping around the traveling transients in the heliosphere, such as CMEs, is essentially a consequence of the fact that magnetized plasma cannot significantly penetrate into the transient, and thus it is forced to flow around it (Gosling & McComas 1987). As a result, for a low inclination CME, we might expect the ambient plasma to be more easily deflected in the north-south direction where the CME extent is smaller, that is we might expect $\theta < 1$. The more complex spiral-structured IMF can thus, following the deflected plasma, more easily escape via the meridional extent of the CME

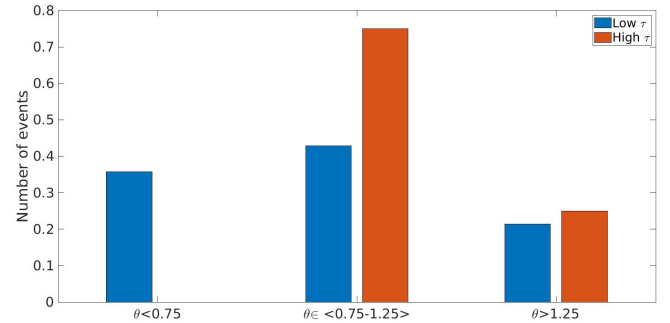


Fig. 7. Occurrence frequency of events with respect to θ ratio. The events are divided into three groups, $\theta < 0.75$, $\theta \in [0.75, 1.25)$, and $\theta > 1.25$. The occurrence frequency for high inclination events is shown in orange, and for low inclination it is shown with blue bars.

Table 4. Statistical results (mean value, median, and standard deviation) derived separately for high inclination and low inclination event samples.

	High	Low
Mean	1.3	1.0
Std	0.6	0.5
Median	1.1	1.0
95% percentile	2.5	2.2

and thus be out of the CME’s path. Consequently, there would be less draping of the more complex spiral-structured IMF across the CME front. For high inclined CMEs, the situation is the reverse as they have a much wider spread in the meridional plane

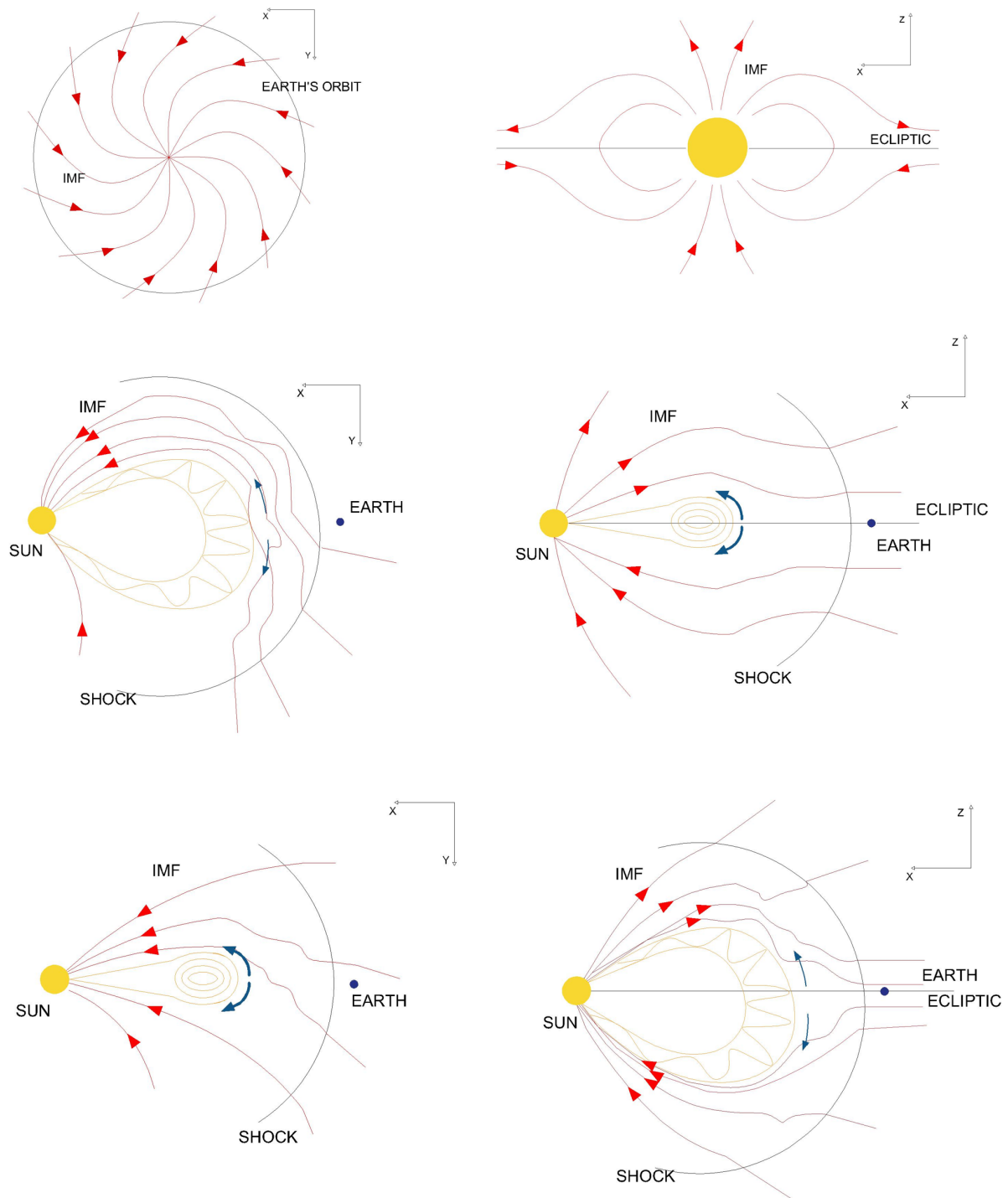


Fig. 8. Idealized IMF in the ecliptic and meridional plane (*top panels*) and its interaction with embedded CME with low (*middle panels*) and high (*bottom panels*) inclination shown schematically. Each panel has a 2D coordinate system drawn in the upper right corner that notes either a yx plane or an xz plane of the GSE coordinate system. The panels also marks the NRF with blue arrows; its width and length suggest the pronouncement of the flow. The figure was adapted from [Gosling & McComas \(1987\)](#).

compared to the ecliptic plane. Here we might expect the ambient plasma to be more easily deflected in the east-west direction where the CME size is smaller, that is we might expect $\theta > 1$. The more complex spiral-structured IMF cannot easily escape via the meridional extent of the CME and thus it is out of the CME's path. Consequently, there would be more draping of the more complex spiral-structured IMF across the CME front. Colloquially put, the CME should be able to “swim” more easily when it has a low inclination.

However, as shown in [Schwenn \(2006\)](#), the velocity of the ambient solar wind is lower near the ecliptic plane than in the higher latitude regions. Consequently, when considering fast CMEs, the relative velocity of a CME and ambient solar wind is larger in low latitude regions. Since the drag force increases as the relative velocity increases ([Cargill 2004](#); [Vršnak 2001](#); [Chen & Garren 1993](#)), it is to be expected that low inclination events experience greater drag force due to a much wider spread in the ecliptic plane than high inclination events.

4. Summary and conclusions

We analyzed 22 well-associated CME-ICME pairs during the rising and the maximum phase of solar cycle 24. We determined their inclination, both at Sun and in situ at the Lagrange L1 point. We derived the CME tilt close to the Sun using three different techniques: GCS, C2-ellipse fitting, and C3-ellipse fitting. GCS was performed when images from at least two spacecraft were available for the 3D reconstruction, while the ellipse fit was performed using the single LASCO-C2 and LASCO-C3 coronagraphic images. The in situ FR type was determined by visual inspection of the magnetic field components in the GSE coordinate system.

Comparing our GCS and ellipse fit results for the FR inclination with results from the HELCATS catalog⁴, Temmer et al. (2021), and Sachdeva (2019), we concluded that the methods are only robust enough to determine whether the FR is of a dominantly high or low inclination. In accordance with this, we only distinguished low and high incline events from the in situ data. When comparing the results for high and low inclination at the near-Sun and at the near-Earth environment, we found that the majority of the events, 68%, have a consistent estimation for the tilt from remote and in situ data. Also, we found that the majority, 73%, have a low inclination. We showed that the CMEs' tilt obtained by GCS varies greatly when determined by different observers, as well as that GCS results are different from the results obtained by the C2- and C3-ellipse fitting technique. These results show that the CMEs' tilt determination still remains a challenge.

Our analysis of the NRFs in the sheath region indicates that high inclination events (as observed in situ) show a slightly higher velocity ratio of the y to z direction. This suggests that the NRFs in the sheath region of high inclined CMEs are more profound in the east-west direction than in the case of low inclined events. Thus, for low inclined events, we might expect the more complex spiral-structured IMF to more easily escape via the meridional extent of the CME and thus be out of the CME's path. This result shows the potential for further research on the relation between an ICME's inclination and propagation. However, in order to do so, much larger sample sizes are needed to provide results of high statistical significance. Due to all the restrictions imposed by different tilt determination methods, sample size increment is certainly not an easily achievable task. However, we have shown here that the C2- and C3-ellipse fit techniques provide results for inclination in good agreement with 3D CME reconstruction using GCS. Thus, the sample sizes can be significantly increased in future work by analyzing CME-ICME pairs before the STEREO era.

Acknowledgements. We acknowledge the support by the Croatian Science Foundation under the project IP-2020-02-9893(ICOHOSS). K.M. acknowledges support by Croatian Science Foundation in the scope of Young Researches Career Development Project Training New Doctoral Students. The SOHO/LASCO data used here are produced by a consortium of the Naval Research Laboratory (USA), Max-Planck-Institut fuer Aeronomie (Germany), Laboratoire d'Astronomie (France), and the University of Birmingham (UK). SOHO is a project of international cooperation between ESA and NASA. We acknowledge the STEREO/SECCHI consortium for providing the data. The SECCHI data used here were produced by an international consortium of the Naval Research Laboratory (USA), Lockheed Martin Solar and Astrophysics Lab (USA), NASA Goddard Space Flight Center (USA), Rutherford Appleton Laboratory (UK), University of Birmingham (UK), Max-Planck-Institute for Solar System Research (Germany), Centre Spatiale de Liege (Belgium), Institut d'Optique Theorique et Appliquee (France), Institut d'Astrophysique Spatiale (France). We acknowledge use of NASA/GSFC's Space Physics Dana Facility's OMNIWeb (or CDAWeb or ftp) service, and OMNI data. B.V. also acknowledges

support by the Croatian Science Foundation under the project 7549 "Millimeter and sub-millimeter observations of the solar chromosphere with ALMA."

References

- Al-Haddad, N., Nieves-Chinchilla, T., Savani, N. P., et al. 2013, *Sol. Phys.*, **284**, 129
- Al-Haddad, N., Galvin, A. B., Lugaz, N., Farrugia, C. J., & Yu, W. 2021, *ApJ*, submitted, [arXiv:2110.10682]
- Bothmer, V., & Schwenn, R. 1998, *Ann. Geophys.*, **16**, 1
- Brueckner, G. E., Howard, R. A., Koomen, M. J., et al. 1995, *Sol. Phys.*, **162**, 357
- Burlaga, L., Sittler, E., Mariani, F., & Schwenn, R. 1981, *J. Geophys. Res.*, **86**, 6673
- Byrne, J. P., Gallagher, P. T., McAteer, R. T. J., & Young, C. A. 2009, *A&A*, **495**, 325
- Cane, H. V., & Richardson, I. G. 2003, *J. Geophys. Res. (Space Phys.)*, **108**, 1156
- Cargill, P. J. 2004, *Sol. Phys.*, **221**, 135
- Cargill, P. J., Chen, J., Spicer, D. S., & Zalesak, S. T. 1996, *J. Geophys. Res.*, **101**, 4855
- Chen, J., & Garren, D. A. 1993, *Geophys. Res. Lett.*, **20**, 2319
- Chen, J., Howard, R. A., Brueckner, G. E., et al. 1997, *ApJ*, **490**, L191
- Delaboudinière, J. P., Artzner, G. E., Brunaud, J., et al. 1995, *Sol. Phys.*, **162**, 291
- Fan, Y., & Gibson, S. E. 2004, *ApJ*, **609**, 1123
- Gosling, J. T. 1990, in *Coronal Mass Ejections and Magnetic Flux Ropes in Interplanetary Space*, eds. C. T., Russell, E. R., Priest, L. C., Lee (*Geophysical Monograph Series*), **58**, 343
- Gosling, J. T., & McComas, D. J. 1987, *Geophys. Res. Lett.*, **14**, 355
- Green, L. M., Kliem, B., Török, T., van Driel-Gesztelyi, L., & Attrill, G. D. R. 2007, *Sol. Phys.*, **246**, 365
- Howard, R. A., Moses, J. D., Vourlidas, A., et al. 2008, *Space Sci. Rev.*, **136**, 67
- Isavnin, A., Vourlidas, A., & Kilpua, E. K. J. 2014, *Sol. Phys.*, **289**, 2141
- Kay, C., Gopalswamy, N., Xie, H., & Yashiro, S. 2017, *Sol. Phys.*, **292**, 78
- Kilpua, E., Koskinen, H. E. J., & Pulkkinen, T. I. 2017, *Liv. Rev. Sol. Phys.*, **14**, 5
- King, J. H., & Papitashvili, N. E. 2005, *J. Geophys. Res. (Space Phys.)*, **110**, A02104
- Klein, L. W., & Burlaga, L. F. 1982, *J. Geophys. Res.*, **87**, 613
- Krall, J., & St. Cyr, O. C. 2006, *ApJ*, **652**, 1740
- Lemen, J. R., Title, A. M., Akin, D. J., et al. 2012, *Sol. Phys.*, **275**, 17
- Lundquist, S. 1950, *Ark. Fys.*, **2**, 361
- Lynch, B. J., Antiochos, S. K., Li, Y., Luhmann, J. G., & DeVore, C. R. 2009, *ApJ*, **697**, 1918
- Maričić, D., Vršnak, B., Veronig, A. M., et al. 2020, *Sol. Phys.*, **295**, 91
- Marubashi, K., Akiyama, S., Yashiro, S., et al. 2015, *Sol. Phys.*, **290**, 1371
- Möstl, C., Miklenic, C., Farrugia, C. J., et al. 2008, *Ann. Geophys.*, **26**, 3139
- Müller, D., Nicula, B., Felix, S., et al. 2017, *A&A*, **606**, A10
- Mulligan, T., Russell, C. T., & Luhmann, J. G. 1998, *Geophys. Res. Lett.*, **25**, 2959
- Nitta, N., & Mulligan, T. 2017, *AGU Fall Meeting Abstracts*, SH51E-04
- Owens, M., & Cargill, P. 2004, *Ann. Geophys.*, **22**, 4397
- Palmerio, E., Kilpua, E. K. J., Möstl, C., et al. 2018, *Space Weather*, **16**, 442
- Sachdeva, N. 2019, Ph. D. Thesis, ArXiv e-prints [arXiv:1907.12673]
- Sachdeva, N., Subramanian, P., Colaninno, R., & Vourlidas, A. 2015, *ApJ*, **809**, 158
- Scherrer, P. H., Bogart, R. S., Bush, R. I., et al. 1995, *Sol. Phys.*, **162**, 129
- Scherrer, P. H., Schou, J., Bush, R. I., et al. 2012, *Sol. Phys.*, **275**, 207
- Schwenn, R. 2006, *Space Sci. Rev.*, **124**, 51
- Shi, T., Wang, Y., Wan, L., et al. 2015, *ApJ*, **806**, 271
- Singh, T., Yalim, M. S., & Pogorelov, N. V. 2018, *ApJ*, **864**, 18
- Temmer, M., Rollett, T., Möstl, C., et al. 2011, *ApJ*, **743**, 101
- Temmer, M., Holzkecht, L., Dumbović, M., et al. 2021, *J. Geophys. Res. (Space Phys.)*, **126**
- Thernisien, A. 2011, *ApJS*, **194**, 33
- Thernisien, A. F. R., Howard, R. A., & Vourlidas, A. 2006, *ApJ*, **652**, 763
- Vandas, M., Fischer, S., Dryer, M., Smith, Z., & Detman, T. 1995, *J. Geophys. Res.*, **100**, 12285
- Vandas, M., Fischer, S., Dryer, M., Smith, Z., & Detman, T. 1996, *J. Geophys. Res.*, **101**, 2505
- Vourlidas, A., Colaninno, R., Nieves-Chinchilla, T., & Stenborg, G. 2011, *ApJ*, **733**, L23
- Vršnak, B. 2001, *Sol. Phys.*, **202**, 173
- Vršnak, B., Žic, T., Vrbanec, D., et al. 2013, *Sol. Phys.*, **285**, 295
- Xie, H., Gopalswamy, N., & Akiyama, S. 2021, *ApJ*, **922**, 64
- Yurchyshyn, V. 2008, *AGU Fall Meeting Abstracts*, SH13B-1551
- Zhang, J., Dere, K. P., Howard, R. A., & Bothmer, V. 2003, *ApJ*, **582**, 520

⁴ https://www.helcats-fp7.eu/catalogues/wp3_kincat.html

2.2 Effects of coronal mass ejection orientation on its propagation in the heliosphere

Effects of coronal mass ejection orientation on its propagation in the heliosphere

K. Martinić¹, M. Dumbović¹, J. Čalogović¹, B. Vršnak¹, N. Al-Haddad³, and M. Temmer²

¹ Hvar Observatory, Faculty of Geodesy, University of Zagreb, Kačićeva ulica 26, 10000 Zagreb, Croatia
e-mail: kmartinic@goef.hr

² Institute of Physics, University of Graz, Universitätsplatz 5, 8010 Graz, Austria

³ University of New Hampshire, Space Science Center, Morse Hall, Durham, NH 03824, USA

Received 10 May 2023 / Accepted 5 September 2023

ABSTRACT

Context. In the scope of space weather forecasting, it is crucial to be able to more reliably predict the arrival time, speed, and magnetic field configuration of coronal mass ejections (CMEs). From the time a CME is launched, the dominant factor influencing all of the above is the interaction of the interplanetary CME (ICME) with the ambient plasma and interplanetary magnetic field.

Aims. Due to a generally anisotropic heliosphere, differently oriented ICMEs may interact differently with the ambient plasma and interplanetary magnetic field, even when the initial eruption conditions are similar. For this, we examined the possible link between the orientation of an ICME and its propagation in the heliosphere (up to 1 AU).

Methods. We investigated 31 CME-ICME associations in the period from 1997 to 2018. The CME orientation in the near-Sun environment was determined using an ellipse-fitting technique applied to single-spacecraft data from SOHO/LASCO C2 and C3 coronagraphs. In the near-Earth environment, we obtained the orientation of the corresponding ICME using in situ plasma and magnetic field data. The shock orientation and nonradial flows in the sheath region for differently oriented ICMEs were investigated. In addition, we calculated the ICME transit time to Earth and drag parameter to probe the overall drag force for differently oriented ICMEs. The drag parameter was calculated using the reverse modeling procedure with the drag-based model.

Results. We found a significant difference in nonradial flows for differently oriented ICMEs, whereas a significant difference in drag for differently oriented ICMEs was not found.

Key words. Sun: coronal mass ejections (CMEs) – Sun: evolution – Sun: heliosphere

1. Introduction

A coronal mass ejection (CME) is a large-scale ejection of plasma and magnetic field from the solar corona into the interplanetary medium. When it reaches Earth, it can cause large disturbances in the near-Earth environment (i.e., it can trigger geomagnetic storms). It is relatively widely accepted that CMEs consist of a so-called flux rope (FR) structure (Chen 1996; Bothmer & Schwenn 1998; Moore et al. 2001) that may drive sheaths and shocks. An FR, in its simplest form, is a cylindrical structure in which a poloidal magnetic field component rotates about an axial magnetic field component that follows the central axis of the cylinder (Lundquist 1950).

Coronal mass ejections have been observed remotely with white-light coronagraphs. A CME FR reconstruction can be performed using stereoscopic coronagraph images. Thernisien et al. (2006) developed a 3D model for CME FR reconstruction, referred to as the graduated cylindrical shell (GCS) model, in which an FR is represented as a “hollow croissant” consisting of two conical legs and a curved front. One of the six main parameters to fully describe the FR in the GCS reconstruction is tilt. The tilt of an FR is defined as the angle between the solar equator and the central axis of the FR. It is measured from solar west to solar north (positive values) and from solar west to solar south (negative values). Defined in this way, the tilt essentially gives the inclination of the CME with respect to the solar equator. Another way to determine the inclination of a CME is

based on a 2D CME reconstruction, first proposed by Chen et al. (1997), where the observed CME front is represented with an ellipse. In this model, changing the position of the ellipse, the length of the axes, and the inclination of the major axis of the ellipse can account for the angular width and inclination of the CME (Krall & St. Cyr 2006; Byrne et al. 2009; Martinić et al. 2022). Martinić et al. (2022) showed that GCS and ellipse fitting give comparable results for the inclination of CMEs when using remote data from coronagraphs aboard the SOHO and STEREO spacecraft for 22 Earth-directed events.

Commonly, there is a distinction between the CMEs observed remotely in the corona and the interplanetary CMEs, or ICMEs, measured in situ by spacecraft. Recently, however, in situ measurements of CMEs in the upper corona and innermost heliosphere taken with the Parker Solar Probe and Solar Orbiter have caused this traditional distinction between CMEs and ICMEs to become less clear. In this study, we use the term “ICME” in the context of in situ measurements and interplanetary interaction with the ambient; for the rest, the “CME” term is used.

Typically, the three-part structure (the shock, the sheath, and the magnetic obstacle) can be well-measured as the spacecraft passes an ICME. First, a fast-forward shock front is usually detected, characterized by an abrupt increase in magnetic field, solar wind speed, and temperature. After the shock front, a so-called ICME sheath region is measured. This is a special case of plasma sheaths where both expansion and propagation

properties are observed (Siscoe & Odstrčil 2008). The ICME sheaths are turbulent and compressed, as evidenced by elevated values and strong fluctuations of the magnetic field, density, velocity, and plasma beta parameter (Kilpua et al. 2017). After the sheath is the driver, the FR part of the ICME, that is, the magnetic obstacle (MO). A subset of well-defined MOs is called a magnetic cloud (MC), which is characterized by a smoothly rotating magnetic field, decreased plasma beta parameter, and decreased temperature (Burlaga 1991). As a first approximation, and based on their chirality and orientation, ICMEs can be classified into eight basic types, as described in Bothmer & Schwenn (1998), Mulligan et al. (1998), and recently by Palmerio et al. (2018). Four of these eight types are low-inclined ICMEs, and the remaining four are high-inclined ICMEs.

Three forces are active during different CME propagation phases. In the early acceleration phase, the Lorentz and gravitational forces compete with each other. Later, the magnetohydrodynamic (MHD) drag force from the solar wind acts on the CME. Observations have shown that CMEs faster than the solar wind slow down, while CMEs slower than the solar wind accelerate (Sheeley et al. 1999; Gopalswamy et al. 2000; Vršnak et al. 2004; Manoharan 2006).

Drag in interplanetary space (MHD drag) is not primarily caused by viscosity and particle collisions but is rather related to the interaction of the ICME with the surrounding magnetic field, such as MHD waves (Cargill et al. 1996) and magnetic field draping (Gosling & McComas 1987), as described in Martinić et al. (2022). Interplanetary CMEs interact with the surrounding plasma and magnetic field as they propagate in the heliosphere. For fast ICMEs embedded in the slow ambient plasma, accelerations and deflections of the ambient plasma occur in front of the ICME FR part. Due to the high electrical conductivity, the ambient solar wind cannot easily penetrate the magnetized ICME structure, but it is accelerated and deflected around the obstacle. This occurs in an ICME sheath region and is particularly pronounced near the ICME FR part. A direct consequence of this plasma motion is the draping of the IMF around the ICME FR. Apart from the relative velocity between the ICME and the surrounding solar wind, the draping pattern depends strongly on the size and shape of the ICME and on the configuration of the surrounding magnetic field (Gosling & McComas 1987; McComas et al. 1988, 1989). Consequently, for differently oriented ICMEs, even if embedded in similar configurations of the ambient magnetic field and solar wind, one might expect a different plasma flow and consequently a different draping pattern, as theorized by Martinić et al. (2022). Figure 1 shows a low-inclination ICME in panel a and a high-inclination ICME embedded in the surrounding magnetic field in panel b. Only the meridional plane, the xz -plane of the Geocentric Solar Ecliptic (GSE) coordinate system, is shown in Fig. 1, and one should consider the Parker spiral (i.e., the Parker spiral configuration of the magnetic field in the xy -plane). In the case of ICMEs with high inclination, more draping occurs due to the interaction with the broader extent of the ICME front. The blue arrows in Fig. 1 schematically represent the plasma flows in front of the obstacle. Due to the larger pressure gradient associated with the pileup of the magnetized solar wind, the ambient plasma is expected to pass the obstacle more easily in the direction in which the extent of the obstacle is smaller. Thus, in an ICME with low inclination, the plasma flow in the xz -plane of the GSE coordinate system is more pronounced than in an ICME with high inclination. In contrast, for an ICME with high inclination, one would expect more pronounced plasma flows in the yz -plane (into and out of the plane shown in Fig. 1). The ambient

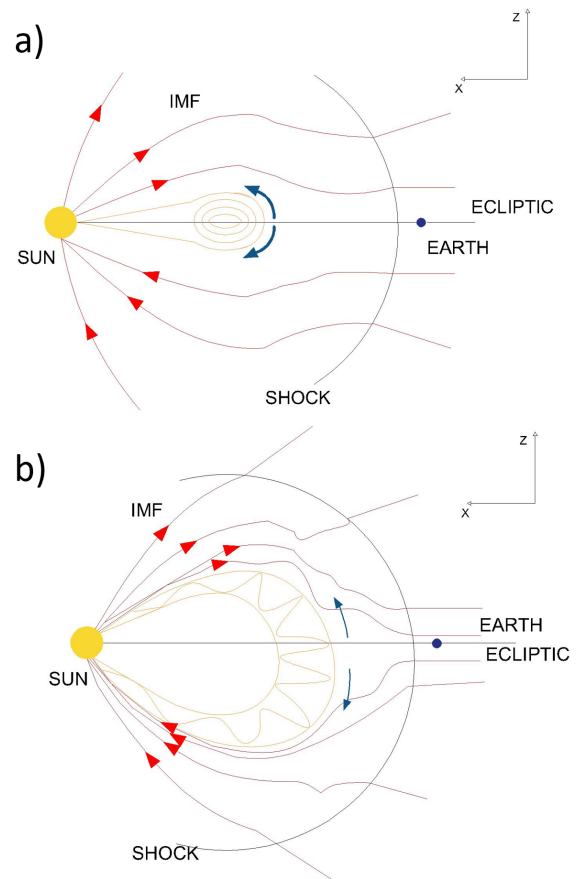


Fig. 1. Idealized IMF in the meridional plane, xz -plane of GSE coordinate system, and its interaction with embedded ICME with low inclination (upper panel) and high inclination (bottom panel). The NRF is shown with blue arrows where its width and length suggest the pronouncement of the plasma flows in front of the embedded ICME. The figure is adapted from Martinić et al. (2022).

field that is draped eventually slides past the obstacle. This process should be more efficient for an ICME with a low inclination since the expansion in the xz -plane is smaller, and the ICME can push the draped field around the obstacle more easily than an ICME with high inclination.

Vandas et al. (1995, 1996) studied the propagation of two MCs, one low inclined and one high inclined, represented by Lundquist's cylindrical force-free solution (Lundquist 1950) in the inner heliosphere using the 2.5D MHD model. Details of this model can be found in Wu et al. (1979; 2D) and Wu et al. (1983; 2.5D). They found that the propagation of these MCs does not depend on the inclination of their axes with respect to the ecliptic plane (one lies in the ecliptic, and the other has an axis perpendicular to it). The MHD model used in these studies was confined to the solar equatorial plane and therefore does not provide a complete 3D MHD representation. In order to provide a better forecast of ICME arrivals, the influence of field line draping and associated nonradial flows (NRFs) on the ICME propagation from the observational perspective needs to be investigated on a statistically relevant sample of events. To our knowledge, this influence was first studied by observation in Martinić et al. (2022). In this present study, we extend the data sample to provide better statistical coverage and investigate the effects of NRFs and field line draping on the propagation behavior of the CME. In Sect. 2, we describe the method by

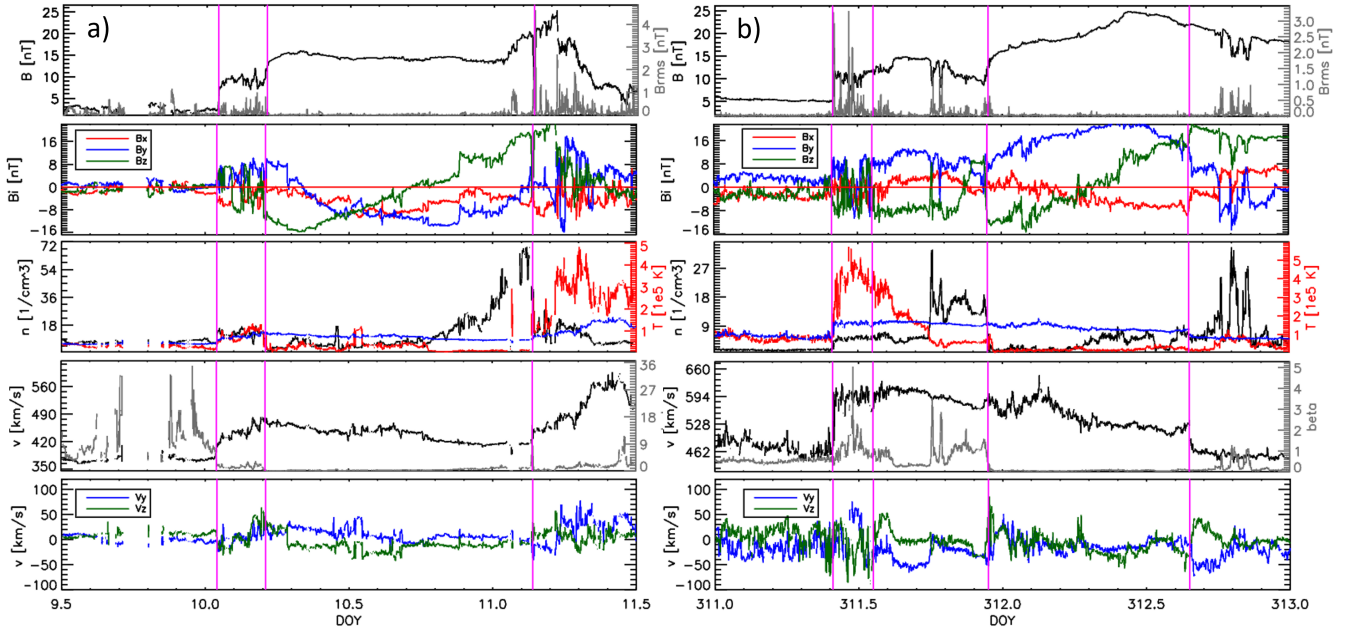


Fig. 2. Interplanetary CME measured in situ on 10 January 1997 (left panels) and 3 November 2000 (right panels). From top to bottom, the following parameters are shown: Magnetic field magnitude in black and magnetic field fluctuations in gray (right scale); GSE magnetic field components (red, B_x ; blue, B_y ; green, B_z); proton density in black, temperature in red, and expected temperature in blue; solar wind speed in black and plasma beta parameter in gray; GSE velocity components (blue, B_y ; green, B_z). From left to right, the vertical magenta lines mark the shock arrival, the end of the clear sheath, and the MO end time. In the right panels, the end of the clear sheath part does not coincide with the MO onset time, and there is an additional vertical magenta line present.

expanding on the study by [Martinić et al. \(2022\)](#). We highlight several dynamical features used to study the interaction between differently oriented ICMEs and the environment. In terms of the plasma flows in front of the ICME FR, we studied NRFs and shock orientation; and in terms of the overall drag, we studied drag parameter and ICME transit time. The main findings are presented in Sect. 3, and our conclusions are in Sect. 4.

2. Data and method

We searched for associated CME-ICME pairs from 1996 to 2020. The lists we used to create our sample can be found in the following studies: [Nitta & Mulligan Skov \(2017; abbr. NM\)](#), [Palmerio et al. \(2018; abbr. P\)](#), [Temmer et al. \(2021; abbr. T\)](#), and [Xie et al. \(2021; abbr. X\)](#).

In total, 113 CME-ICME pairs were found, but only 31 were used in our analysis. Most events were excluded for two reasons: insufficiently developed sheath region (32 excluded) and unclear MO boundary determination (30 excluded). The former relates to missing signatures of a clear sheath region ahead of the MO (for a discussion of CMEs with and without sheath regions, see [Salman et al. 2020](#)). As highlighted in [Kilpua et al. \(2017\)](#), the sheath thickness depends on the velocity and physical properties of the driving MO and the ambient solar wind, but sheath thickness has also been shown to increase from the nose toward the flanks. Unclear MO boundary determination is related to the subjectivity in determining the boundaries of the MO. There are some MO examples where there are clearly multiple rotations of the same or different magnetic field components, and in such cases, it is not straightforward to establish the MO boundaries and associate the example with a simple FR categorization of eight types. Other reasons why some of the events were excluded are as follows: faint CME front and multiple eruptions within the LASCO field of view (11 excluded); possible ICME interac-

tions with other ICMEs or high-speed streams (4 excluded); no clear magnetic field rotation, that is ejecta-ICME, (1 excluded); no in situ data (1 excluded); possible incorrect CME-ICME association (1 excluded); and inconsistent dominant inclination derived from remote observations and in situ measurements (2 excluded). Ultimately, 31 CME-ICME pairs in the period from 1997 to 2018 with clear MO signatures were left.

2.1. Dominant inclination determination

We derived the dominant inclination for the CME-ICME pairs from both the remote and in situ data. For the remote data, we used SOHO/LASCO ([Brueckner et al. 1995](#)) coronagraph images and performed an ellipse fit. This method assumes that the outer edge of the (partial) halo CME can be represented by an ellipse whose major axis inclination indicates the dominant inclination of the CME. An example of the application of the ellipse-fitting technique to event number eight is shown in Fig. 3. The top row shows running difference images in the LASCO-C2 and LASCO-C3 field of view (FOV). In the bottom row, the ellipse fitting is overlaid with a red line.

In situ data was obtained from the WIND and ACE space probes, available through the OMNI database ([King & Papitashvili 2005](#)). The dominant inclination from the in situ data was derived from the rotation of the magnetic field components in the MO part of the ICME using the GSE system. If the rotation of the B_z component was observed to change sign but the B_y component retained its sign, we considered the event to be a dominantly low-inclined event (see Fig. 2). On the other hand, if a sign change was observed in the B_y component but the B_z component remained the same throughout the MO, the event was considered to be dominantly high inclined. We divided all events into eight basic categories. Four of these eight categories are dominantly high inclined (ESW,

ENW, WSE, and WNE), and the other four are dominantly low inclined (SWN, NWS, SEN, and SWN). Here, E stands for east, W for west, N for north, and S for south. The ESW type has an axis directed toward the south and a helical field rotating from east to west. The ENW type has the same helical field rotation, but the axial field is directed toward the north. The same applies to the others. The results of the classification are shown in Table 2. Al-Haddad et al. (2013) found that FR reconstruction shows different inclinations for different FR reconstruction techniques, and this varies greatly with the MO boundary set. This is the reason why we only distinguish between dominantly high- and dominantly low-inclined events, rather than deriving the exact inclination for each event (see Martinić et al. 2022).

In summary, we divided all events into two groups: events with predominantly low inclination and those with predominantly high inclination. Events with predominantly low inclination are those with an inclination of less than 40° , as determined from the ellipse fit, and with a rotation in the B_z magnetic field component (ESW, ENW, WSE, and WNE), as observed in situ. Events with predominantly high inclination are those with an inclination greater than 45° , as determined from the ellipse fit, and with rotation in the B_y magnetic field component (SWN, NWS, SEN, and NES), as seen in situ. We considered the events with an inclination between 40° and 45° to be intermediate inclination events and did not include them in the analysis.

For two CME-ICME pairs that were excluded, we found inconsistencies in the dominant inclination inferred from the in situ and remote data. Xie et al. (2021) showed that 25% of the events studied had a rotation of more than 40° from the near-Sun to L1. They also showed that 56% of these events exhibited rotation in the STEREO/SECCHI-COR2 FOV (i.e., in the mid-corona). Isavnin et al. (2013) showed that about one-third of the events studied showed a change in inclination from predominantly low to high, or vice versa. In our sample of 33 events, we found only two events where this was true. This could be due to the fact that we excluded over 30 CME-ICME pairs because of ambiguous rotation of the magnetic field components within the MO part of the ICME. Of the remaining 31 events, 19 are dominantly low inclined, while 12 are dominantly high inclined. These 31 CMEs are listed in Table 1, and their interplanetary counterparts, ICMEs, are listed in Table 2. The first column of Table 1 shows the event number accompanied by an abbreviation indicating which study the CME-ICME association was taken. The second column shows the first C2 appearance time as reported in the SOHO/LASCO CME catalog¹. The third and fourth columns show the time at which the ellipse fit reconstruction was performed in the LASCO-C2 and LASCO-C3 FOV, respectively. This is followed by the columns showing the obtained tilt, in LASCO-C2 FOV and LASCO-C3 FOV, respectively. The last column shows whether the event is dominantly high or dominantly low inclined, as obtained from the ellipse fit in the LASCO-C2 and LASCO-C3 FOV. The letter “L” indicates that the event is dominantly low inclined and that the average of the absolute tilt values obtained from the ellipse fit reconstruction in LASCO-C2 and LASCO-C3 FOV is less than 40° . The letter “H” indicates that the event is dominantly high inclined. Analogously, such events are those whose average absolute tilt values are higher than 45° .

In Table 1, one can see that the inclination derived from LASCO-C2 may differ from the inclination derived from the LASCO-C3 coronagraphic images. The CME evolves through the entire FOV of C2 and C3, and by marking slightly different

leading edges (green crosses in Fig. 3) at different times, we can infer slightly different inclinations for the same event. We note that this is not necessarily related to strong rotations and deflections in the LASCO-C2 or LASCO-C3 FOV (Yurchyshyn et al. 2009; Vourlidas et al. 2011; Kay et al. 2017) but to simple ambiguities inherent in the measurements. This is also visible in Fig. 3, where in LASCO-C3 FOV the ellipse is slightly less inclined than in the LASCO-C2 FOV. This is one of the reasons why we focus only on the dominant inclination.

2.2. Sheath region nonradial flows and shock orientation

The boundaries of the MO and sheath region were determined manually for each event. We note that the selection of ICME boundaries involves a degree of uncertainty. In the first instance, the boundaries of the MO were chosen to cover the entire magnetic field rotation. When this was not possible due to the rotation of several magnetic field components, the events were excluded. As mentioned earlier, there were 30 events where this was the case. From left to right, the columns in Table 2 show the event number, the date of the MO onset, shock-clear sheath occurrence time SH_{start} , clear sheath end time SH_{end} , the MO onset time, the MO end time, the derived FR type, the NRF ratio, the shock orientation θ_B , the observed transit time TT, and γ parameter. The sheath region was divided into two parts in some cases. The first part is the region where only clear sheath signatures can be seen (i.e., a strongly fluctuating magnetic field and plasma with increased density, temperature, and plasma beta). The second part of the envelope has fewer high plasma parameters and/or a not as strongly fluctuating magnetic field. This part shows no clear sheath and no clear MO properties. We identified this second part in 14 out of 31 events, as shown in Table 2 (see column SH_{end}). In these 14 events, the end of the clear sheath region does not correspond to the beginning of the MO part. This part between the clear sheath and the clear MO was studied by Kilpua et al. (2013), who recognized it as the disturbed front part of the FR known as the MO front region. More recently, Temmer & Bothmer (2022) recognized this as compressed ambient solar wind and noted it as a leading edge structure. An example of a sheath with clear sheath properties is shown in the left panels of Fig. 2, while an example of a more complex sheath where the clear sheath is observed after the shock but then toward the MO part of the ICME one can also see a region with both sheath and MO properties is shown in the right panels of Fig. 2. There, one can observe a region that shows a stronger magnetic field with fewer fluctuations than in the clear sheath part. The density and plasma beta parameter show a further increase accompanied by a decrease in the temperature.

Interplanetary CMEs are usually associated with NRFs in (1) the sheath region and (2) the expanding magnetic ejecta part. The first association is due to the plasma motion of the ambient solar wind escaping around the ICME ejecta part, and the second is related to the expansion of the magnetic ejecta in the nonradial direction, as described in Al-Haddad et al. (2022). The NRF in the sheath region was previously studied by Gosling & McComas (1987). They discovered a westward flow related to the magnetic stress of the Parker spiral acting on ICMEs. Later, Owens & Cargill (2004) showed that the NRF in the sheath region can be used as an indicator of the local axis orientation of ICMEs and the point at which spacecraft and ICMEs meet. Additionally, Liu et al. (2008) investigated whether NRFs in the sheath could relate to the curvature of the MO.

Similarly, Martinić et al. (2022) showed how differently oriented ICMEs may have different NRFs. We calculated the NRF

¹ https://cdaw.gsfc.nasa.gov/CME_list/

Table 1. Remote features of the observed CMEs.

Nr.	First C2 appearance	Ellipse fit in C2	Ellipse fit in C3	Tilt C2 [°]	Tilt C3 [°]	Inclination
1 ^X	1997-01-06 15:10	No data	1997-01-07 01:59		3	L
2 ^X	1997-10-06 15:28	1997-10-06 18:44	1997-10-07 02:31	20	20	L
3 ^X	1997-11-04 06:10	1997-11-04 06:42	1997-11-04 09:40	-87	74	H
4 ^X	1998-01-02 23:28	1998-01-03 01:28	1998-01-03 03:40	-51	-89	H
5 ^X	2000-08-09 16:30	2000-08-09 17:04	2000-08-09 21:18	33	30	L
6 ^X	2000-11-03 18:26	2000-11-03 22:26	2000-11-04 01:42	-33	-27	L
7 ^X	2001-04-26 12:30	2001-04-26 13:29	2001-04-26 14:15	35	8	L
8 ^X	2002-03-15 23:00	2002-03-15 23:52	2002-03-16 01:42	71	67	H
9 ^X	2002-04-15 03:50	2002-04-15 04:50	2002-04-15 05:18	21	24	L
10 ^X	2003-08-14 20:06	2003-08-14 21:53	2003-08-15 02:40	55	50	H
11 ^X	2005-05-13 17:12	2005-05-13 17:22	No data	54		H
12 ^{T,X}	2008-12-12 08:54	2008-12-12 11:54	2008-12-12 15:42	-35	-37	L
13 ^{T,X}	2010-04-03 10:33	2010-04-03 10:50	2010-04-03 12:42	6	-18	L
14 ^{T,NM,X}	2010-06-16 14:54	2010-06-16 20:06	No data	-30		L
15 ^{P,T,X}	2011-06-02 08:12	2011-06-02 08:48	2011-06-02 09:54	-57	-57	H
16 ^{P,X}	2011-09-14 00:00	2011-09-14 01:36	2011-09-14 03:06	-15	-5	L
17 ^{P,T,X}	2011-10-22 01:25	2011-10-22 02:24	2011-10-22 04:18	-53	-55	H
18 ^{P,T}	2012-01-19 14:36	2012-01-19 15:48	2012-01-19 16:42	-2	-20	L
19 ^{P,T,X}	2012-06-14 14:12	2012-06-14 14:36	2012-06-14 16:18	18	11	L
20 ^{P,T,X}	2012-07-12 16:48	2012-07-12 17:24	No data	50		H
21 ^{P,T,NM,X}	2012-10-05 02:48	2012-10-05 05:24	2012-10-05 08:42	45	45	H
22 ^{T,X}	2012-11-09 15:12	2012-11-09 16:00	2012-11-09 18:20	31	22	L
23 ^{P,X}	2013-01-13 12:00	2013-01-13 15:54	Faint LE	-6	0	L
24 ^{P,T,X}	2013-04-11 07:24	2013-04-11 08:24	2013-04-11 10:30	84	90	H
25 ^{NM,X}	2013-06-23 22:36	2013-06-24 02:48	Faint LE	59		H
26 ^{P,T,X}	2013-07-09 15:12	2013-07-09 16:24	Faint LE	12		L
27 ^{P,T,X}	2014-08-15 17:48	2014-08-15 20:24	Faint LE	-52		H
28 ^X	2015-11-04 14:48	2015-11-04 15:24	2015-11-04 17:30	23	37	L
29 ^X	2016-10-09 02:24	2016-10-09 06:24	2016-10-09 10:18	-15	-35	L
30 ^X	2017-05-23 05:00	2017-05-23 08:24	2017-05-23 13:29	15	-3	L
31 ^X	2018-03-06 01:25	2018-03-06 03:48	Faint LE	20		L

Notes. The first column is the event number with the indication of where the CME-ICME association was taken from and is followed by the CME's first C2 appearance time. The third column corresponds to the time the ellipse fit was performed in LASCO-C2 FOV, and the fourth column is the time the ellipse fit was performed in LASCO-C3 FOV. The fifth and sixth columns show the tilt results derived from LASCO-C2 and LASCO-C3, respectively. The last column shows the dominant inclination obtained from Tilt C2 and Tilt C3 values (see text for details); "L" stands for low inclination, "H" stands for high inclination, and "LE" stands for the leading edge.

ratio between the plasma flow in the y and z directions of the GSE coordinate system. The NRF flow is defined as the average of the absolute flow of the plasma in the y or z direction in GSE. The NRF ratio for each event is given in Table 2, Col. 8. We emphasize that the NRF ratio was determined from the part of the sheath where we observed only unique sheath features. For the 14 events mentioned above with complex sheath structures, this means that only the first part of the sheath was considered. In addition to the NRF in the sheath region, the shock orientation θ_B , that is, the angle between the shock normal vector \hat{n} and the upstream magnetic field B_{up} :

$$\theta_B = \frac{180^\circ}{\pi} \arccos\left(\frac{|B_{\text{up}} \cdot \hat{n}|}{\|B_{\text{up}}\| \|\hat{n}\|}\right). \quad (1)$$

The shock normal vector \hat{n} was calculated by the mixed-mode method Abraham-Shrauner & Yun (1976), and in the cases where the data gap of velocity components was present, magnetic coplanarity from Colburn & Sonett (1966) was used. (For more detail on the \hat{n} calculation, we refer the reader to the database of interplanetary shocks from which the θ_B were

obtained²). The shock orientation θ_B values are given in Table 2. One can notice that not all events from Table 2 have a corresponding θ_B . These events (3, 12, 14, 23, and 31) do not meet the shock criterion given in the database of interplanetary shock documentation. However, they have a sheath developed enough to compute NRFs, as indicated above.

2.3. Transit time

The transit time (TT) was calculated as the time difference between the time of onset of the ICME MO in the in situ data and the CME start time at $20 R_s$ (solar radii). We note that this transit time is not the same as the one typically given in databases that corresponds to the arrival time of the shock. The CME start time at a starting radial distance of $20 R_s$ was taken from the second order fit of the altitude-time measurements provided by SOHO/LASCO CME catalog³. When measurements were only available for starting radial distances less than $20 R_s$, an

² <http://ipshocks.fi/database>

³ https://cdaw.gsfc.nasa.gov/CME_list/

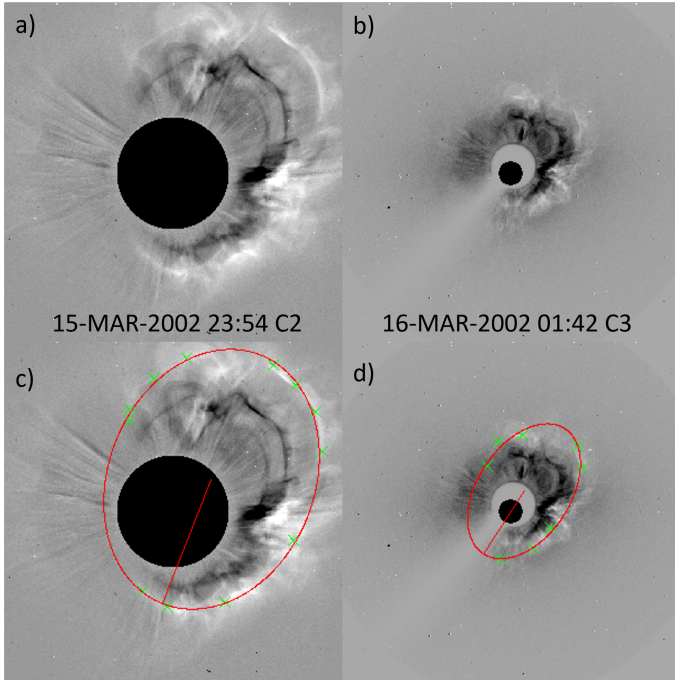


Fig. 3. Coronal mass ejection that occurred on 15 March 2002. The upper panels show the running difference images in LASCO-C2 (left) and LASCO-C3 (right). The bottom panels show the corresponding ellipse fitting. The ellipse is indicated with a red line, whereas green crosses mark the points outlined on the CME front used to obtain the fit.

interpolation was performed using the acceleration corresponding to the same second order fit.

2.4. Drag-based model and γ parameter determination

Observational studies have derived that drag force dominates ICME propagation after a certain distance in the heliosphere. Results from these studies have formed the basis of numerous drag-based CME models (Vršnak et al. 2013; Hess & Zhang 2015; Möstl et al. 2015; Kay & Gopalswamy 2018), which apply the simple analytical equation:

$$F_d = \gamma(v - w)|v - w|, \quad (2)$$

where v is the CME velocity, w is the solar wind velocity, and γ is the so-called drag parameter given by the following equation (Vršnak et al. 2013):

$$\gamma = C_d \frac{A\rho_w}{M + M_V}. \quad (3)$$

Here, A is the cross-sectional area of the CME, ρ_w is the solar wind density, M is the CME mass, M_V is the mass corresponding to the volume of the fluid displaced by the movement of the body (the so-called virtual mass), and C_d is the dimensionless drag coefficient. We emphasize that C_d is usually taken as one and as a constant during the propagation of the ICME. However, Cargill (2004) has shown that the value of C_d depends on the relative density and velocity of the CME with respect to the density and velocity of the solar wind. Cargill also showed that the value of C_d increases from one for dense CMEs to as high as three for low-density CMEs and that C_d has a significant radial dependence for the latter.

The drag parameter γ is a very important parameter in the context of the drag force acting on a CME. Due to its dependence on CME cross section, mass, virtual mass, and solar wind density, obtaining the drag parameter γ through direct measurements is currently unreliable (see e.g., Vršnak et al. 2013; Dumbović et al. 2021). To derive the most reliable gamma value for our data sample, we used a reverse modeling method with the drag-based ensemble version v3 tool (DBEMv3 tool; Čalogović et al. 2021). In DBEMv3, input parameters (CME start time, CME source region longitude, CME half-width, solar wind speed, starting speed of CME, and γ parameter) with their uncertainties follow a normal distribution, with the observation input value set as the mean and three standard deviations as the uncertainty. The DBEMv3 tool creates 100 000 ensemble members from these input parameters and performs a single DBM run for each of them. For more detail on the creation of ensemble members using the DBEMv3 tool, the reader is referred to Čalogović et al. (2021), and for a comprehensive description of the basic DBM and later developed versions, such as this ensemble version, to Dumbović et al. (2021). The reverse modeling method with DBEM has also been used by Paouris et al. (2021) to find the optimal γ parameters and solar wind speed for a different subset of CME-ICME pairs.

For this particular study, the input parameters of CME start time, CME source region longitude, and CME half-width were set without uncertainties. These values are given in Table 3. The derivation of the CME start time is described in Sect. 2.3. The CME source region was determined from low coronal signatures: post-flare loops, coronal dimmings, sigmoids, flare ribbons, and filament eruptions. For this, we used the JHeliowiever (Müller et al. 2017) visualization tool. We analyzed 171, 211, 193, and 304 Å filtergrams from SDO/AIA (Lemen et al. 2012) and SDO/HMI (Scherrer et al. 2012) magnetogram data. When these data were not available, we used SOHO/EIT (Delaboudinière et al. 1995) and SOHO/MDI (Scherrer et al. 1995) magnetogram data. The CME half-width, λ , was set to 89° because all events were (partial) halo events as seen in the LASCO-C2 and LASCO-C3 FOV. The solar wind speed w and the starting speed of CME v_0 follow a normal distribution, with the mean value being an observed value given in Table 3. The solar wind speed was obtained from in situ plasma measurements provided by the OMNI database King & Papitashvili (2005), and it was determined as the mean velocity of the solar wind over an undisturbed period of several hours prior to the arrival of the CME shock. The CME start speed was taken as a second order speed given in SOHO/LASCO CME catalog⁴. The uncertainty (i.e., 3σ value) for both the CME start speed and solar wind speed was set to 10% of the mean value. For the purpose of reverse modeling with DBEMv3, we set the allowed gamma range to $0.01-10 \times 10^{-7} \text{ km}^{-1}$ with an equal probability for all γ parameters in this range (i.e., the γ parameter followed a uniform distribution in this range). As part of the reverse modeling procedure, we searched for the optimal γ parameters where the forecast transit time is within one hour of the actual observed transit time. The median values of these obtained γ parameters are listed in Table 2.

Events 1, 10, 26, 27, 29, and 31 in Table 3 are marked with an asterisk. For these events, the original DBEMv3 input was changed because there were no transit times matching the observed transit time within one hour (i.e., no γ parameters were found). We studied those events in more detail, and we found that for events 1, 10, 29, and 31, the radial takeoff distance needed to

⁴ https://cdaw.gsfc.nasa.gov/CME_list/

Table 2. In-situ derived features of ICMs, shock angle θ , and γ parameter obtained with the reverse modelling procedure.

Nr.	In situ date	SH_{start}	SH_{end}	MO_{start}	MO_{end}	FR type	NRF ratio	θ_B [°]	TT [h]	γ [10^{-7} km^{-1}]
1	1997-01-10	10.04		10.21	11.14	SWN	0.56	51	46.46	0.096
2	1997-10-10	283.68	283.92	284.15	285	SWN	0.88	89	98.33	8.901
3	1997-11-07	310.95	311.26	311.68	312.57	WNE	1.85	No data	78.4	0.431
4	1998-01-07	6.58	6.98	7.11	8.4	ENW	1.28	59	90.31	0.418
5	2000-08-12	224.8		225.25	226.25	SEN	1.02	64	59.92	0.125
6	2000-11-06	311.4	311.55	311.95	312.65	SEN	1.06	46	68.3	1.141
7	2001-04-28	118.2	118.48	119.08	119.6	SEN	1	48	58.34	0.460
8	2002-03-19	77.55		78.24	79.52	WNE	0.96	39	75.59	0.355
9	2002-04-17	107.47	107.7	108.02	109.15	SWN	0.92	66	64.23	0.137
10	2003-08-18	229.58		230.12	231.25	ESW	1.13	62	53.9	2.332
11	2005-05-15	135.12	135.26	135.4	136.1	ENW	2.39	62	38.58	0.180
12	2008-12-17	351.5		352.2	352.8	NWS	1.22	No data	102.34	4.782
13	2010-04-05	95.35	95.48	95.53	96.57	NWS	0.43	54	45.31	
14	2010-06-21	171.95		172.35	173.7	NES	1.76	No data	99.07	4.169
15	2011-06-05	155.85		156.05	156.42	WNE	0.98	69	61.7	0.239
16	2011-09-17	260.15	260.35	260.69	261.49	SEN	1.02	87	80.39	0.227
17	2011-10-25	297.78	297.91	298.05	298.67	ENW	0.57	64	66.03	0.106
18	2012-01-22	22.25		22.52	22.77	NWS	0.87	85	66.73	0.465
19	2012-06-16	168.84	168.95	169.05	169.51	NES	1.76	60	55.95	0.135
20	2012-07-15	196.77		197.3	199.1	ESW	1.09	33	70.28	0.627
21	2012-10-08	282.22		282.76	283.35	ESW	1.84	74	81.32	0.502
22	2012-11-13	317.97		318.4	319.15	NES	0.66	68	84.6	0.276
23	2013-01-17	17		17.71	18.5	SWN	0.58	No data	88.54	7.762
24	2013-04-14	103.95		104.75	105.95	ENW	2.5	40	78.91	1.118
25	2013-06-28	178.6		179.1	180.5	WSE	2.23	74	88	0.831
26	2013-07-13	193.72		194.25	195.35	NWS	1.14	79	78.43	0.087
27	2014-08-19	231.28	231.77	231.9	233.48	WNE	1.2	85	90.06	
28	2015-11-07	310.75	311.08	311.3	312.48	SWN	0.82	46	59.28	0.222
29	2016-10-13	286.92		287.25	288.62	SEN	1.21	16	68.47	0.195
30	2017-05-28	147.65	147.9	147.98	149	SWN	1.33	81	101.1	0.065
31	2018-03-10	68.75		69	69.8	SWN	0.42	No data	54.89	0.164

Notes. First column shows the event number. Next is the date of MO onset followed by sheath onset time (SH_{start}); sheath end time (SH_{end}); MO onset time (MO_{start}); and MO end time (MO_{end}), all given in day of the year (DOY). The following columns show the FR type, NRF ratio, shock orientation θ_B , observed transit time (TT) in hours. Finally, the gamma parameter is given in the last column.

be changed. For events 26 and 27, the takeoff speed and speed uncertainty needed to be increased.

The height at which the drag force begins to dominate is not universal and varies greatly from event to event (Vršnak 2001; Sachdeva et al. 2015, 2017). For events 1, 10, 29, and 31, we found that a starting radial distance of $20R_s$ is not suitable as a DBEM input because the CME is still accelerating at this distance, and its propagation is therefore not dominated by the drag force. To improve our input for these events, the starting distance was increased by the trial-and-error method until a suitable initial distance was found that provided a “perfect transit time” (similar to Sachdeva et al. 2015). For events 1, 10, and 31, this distance was found to be $70R_s$, and we found it to be $50R_s$ for event 29.

For events 26 and 27, we found that the initial CME speed at $20R_s$ may be underestimated. This speed underestimation might come from the use of the second order fit of the height-time measurements. The second order fit shows a very small deceleration in the LASCO FOV. A linear fit yielded slightly different velocity estimates that provided physical solutions to find an optimal γ with DBEM for event 26. The uncertainties of the CME launch speed were also increased to 20% in order to better compensate for the initial underestimation of velocity. For event 27, even after considering the linear speed and after

increasing the uncertainties of the initial velocity, the optimal γ parameter was not found. It could be that the DBM does not capture the physics of this event well. The same is true for event 13. This CME was launched on 3 April 2010 and is a well-studied event (Rodari et al. 2018; Zhou et al. 2014; Rollett et al. 2012; Temmer et al. 2011; Liu et al. 2011). Temmer et al. (2011) reported quite complex CME dynamics in the LASCO FOV and later in the heliosphere. This CME initially strongly accelerated up to 1100 km s^{-1} and then had an abrupt deceleration down to 800 km s^{-1} (all below $20R_s$). Later, the CME again accelerated and decelerated in the heliosphere, possibly due to a high-speed stream crossing. Due to its complex dynamics, this event is not suitable for reverse modeling with the DBEM or DBM in general. We find that it is also important to emphasize that even more sophisticated 3D MHD models such as ENLIL were not able to correctly represent the propagation of this CME (Temmer et al. 2011).

We note that some of the obtained γ values lay outside of an expected range, $0.2\text{--}2 \cdot 10^{-7} \text{ km}^{-1}$, as given by Vršnak et al. (2013). This is most prominent for events 2, 12, 14, and 23 (see Table 2). We also emphasize that such high γ values might be unreal, but testing such an assumption is beyond the scope of this paper. This would require meticulous analysis of the pre-eruption state of the heliosphere as well as detailed eruption

Table 3. DBEM input parameters.

Nr.	t_0	v_0 [km s ⁻¹]	ϕ_{CME} [°]	w [km s ⁻¹]
1*	1997-01-08 06:34	625	6	375
2	1997-10-07 01:16	620	0	407
3	1997-11-04 09:55	700	25	335
4	1998-01-03 08:20	515	40	309
5	2000-08-09 21:05	720	-15	416
6	2000-11-04 02:30	643	0	475
7	2001-04-26 15:35	1084	20	444
8	2002-03-16 02:10	917	7	293
9	2002-04-15 08:15	731	7	331
10*	2003-08-15 15:14	630	0	471
11	2005-05-13 19:00	1689	0	415
12	2008-12-12 20:47	432	-10	339
13	2010-04-03 15:10	661	20	509
14	2010-06-17 05:20	397	2	370
15	2011-06-02 11:30	996	6	337
16	2011-09-14 08:10	457	7	413
17	2011-10-22 07:10	663	25	323
18	2012-01-19 17:45	1390	-24	326
19	2012-06-14 17:15	983	-7	297
20	2012-07-12 18:55	2265	-20	326
21	2012-10-05 08:55	804	15	318
22	2012-11-09 21:00	603	-20	284
23	2013-01-14 00:33	339	-22	403
24	2013-04-11 11:05	819	-15	390
25	2013-06-24 10:10	513	40	373
26*	2013-07-09 23:34	450	-20	386
27*	2014-08-16 03:00	342	5	295
28	2015-11-04 19:55	708	5	465
29*	2016-10-10 09:31	495	-17	355
30	2017-05-23 16:30	367	0	303
31*	2018-03-07 17:06	538	-8	366

Notes. The number of the CME is indicated under Nr.; t_0 is the CME start date and time in UT at $20R_{\text{SUN}}$; v_0 is the CME start speed at $20R_{\text{SUN}}$ given in km s⁻¹; ϕ_{CME} is the longitude of the CME source position in degrees; and w is the solar wind speed in km s⁻¹.

analysis (see Žic et al. 2015 and Temmer et al. 2012). We also highlight that from a theoretical point of view (see Eq. (2)), for cases when the CME launch speed is close to the solar wind speed, the corresponding optimal γ obtained by the reverse modeling with drag-based models can easily take on very large values that may not be physically plausible. However, we also note that the reverse modeling procedure gave results close to the expected range of values for the majority of events, (i.e., for 25 out of 31 events).

3. Results and discussion

Dominant inclination results obtained from remote and in situ data are given in the last column of Table 1 and the sixth column of Table 2, respectively. In Fig. 4, we show the occurrence frequency of dominantly low- and high-inclined events with respect to NRF, transit time, shock orientation, and γ parameter. One can see that most of the high- and low-inclination events have NRF ratios close to one. However, there is a greater number of low-inclination events with low NRF ratios and a greater number of high-inclination events with high NRF ratios. This is consistent with the results of Martinić et al. (2022), where a similar procedure was applied to a smaller sample of events.

This suggests that NRFs are more pronounced in the $\pm y$ direction for events with high inclination and in the $\pm z$ direction for events with low inclination. The mean, median, standard deviation, and 95th percentile for NRF ratios are shown in Table 4. The mean, median, and 95th percentile show larger values for high-inclination events, confirming the results of the distribution plot in Fig. 4a. We observed that the standard deviation for high-inclination events is almost twice the standard deviation of low-inclination events, which is related to the spread of NRF values. Namely, low-inclination events can be found in the 95th percentile interval [0.42, 1.76], while high-inclination events have a 95th percentile interval [0.78, 2.44].

As stated earlier, the NRF ratios were calculated from the velocity in the y and z directions of the GSE coordinate system in the clear sheath part of the ICME and are a consequence of ambient plasma interacting with the FR part of the ICME. However, we note that the deflection of plasma due to fast-forward shock may also contribute to the NRF and this contribution cannot be easily disentangled from the contribution due to draping. In order to confirm that the above-stated dependence of NRF ratios on ICME inclination comes from plasma being deflected around the ICME FR part rather than from plasma that is being deflected on the shock front, we calculated the shock orientation and studied the dependence of shock orientation on inclination. This dependence can be seen in the distribution of θ_B in Fig. 4c. Unlike NRF ratios, the shock orientation (which determines the shocked plasma deflection right behind the shock front) does not show dependence on ICME inclination. From Table 2, we also observed that most events have θ_B greater than 45°, which means that most of the events studied have a quasi-perpendicular shock front.

In order to quantitatively test the difference between low- and high-inclination samples, we performed the Welch's test (in case of different sample variances) and the student t -test (in case of similar sample variances). First, in order to choose an adequate test for the means of the populations, we had to test the sample variances. To see whether two samples have similar or different variances we used a statistical F -test. According to the F -test, with a 95% confidence level, the shock orientation θ_B and transit time have similar variances for high- and low-inclination groups of events; however, for NRF ratio and gamma parameter γ , these two groups of events show statistically significant variances. High-inclination events (orange bars in Fig. 4) have a wider spread in NRF ratios in comparison to low-inclination events (blue bars), shifting the distribution toward higher NRF ratio values. Regarding the γ parameter, low-inclination events (blue bars in Fig. 4d) have a wider spread. The same is not valid for transit time and shock orientation.

Welch's test null hypothesis is that the NRF ratios for low- and high-inclination events come from random samples from normal distributions with equal means and unequal variances. Welch's test was performed under the assumption that (1) the NRF ratio/ γ parameter for high- and low-inclination events are independent, (2) the NRF ratio/ γ parameter distributions for low- and high-inclination samples are normal, and (3) the NRF ratio/ γ parameter variances for low-inclination and high-inclination events are different (according to the F -test).

The result of Welch's test for NRF ratios is that the null hypothesis should be rejected at the 95% significance level (i.e., the NRF ratios for high- and low-inclination events come from populations with unequal means). The interpretation of the different NRFs observed for ICMEs with different inclinations comes from the fact that the ambient plasma in front of the ICME bypasses the obstacle (ICME FR) in a way where the

Table 4. Statistical results.

	Low inclination				High inclination			
	NRF ratio	θ_B [°]	TT [h]	γ [$\times 10^{-7}$ km $^{-1}$]	NRF ratio	θ_B [°]	TT [h]	γ [$\times 10^{-7}$ km $^{-1}$]
Mean	0.98	62.67	72.7	1.63	1.5	60.09	72.8	0.65
Median	1.00	64	68.3	0.22	1.24	62	76.99	0.43
Std	0.37	19.31	18.63	2.80	0.61	15.64	15.02	0.60
Perc[5,95]	[0.42,1.76]	[37,87.6]	[46.35,101.22]	[0.08,7.93]	[0.78,2.44]	[36,79.5]	[47.00,90.44]	[0.14,1.72]

Notes. Mean, median, standard deviation, and 5. and 95. percentiles for low- and high-inclination events (reported separately).

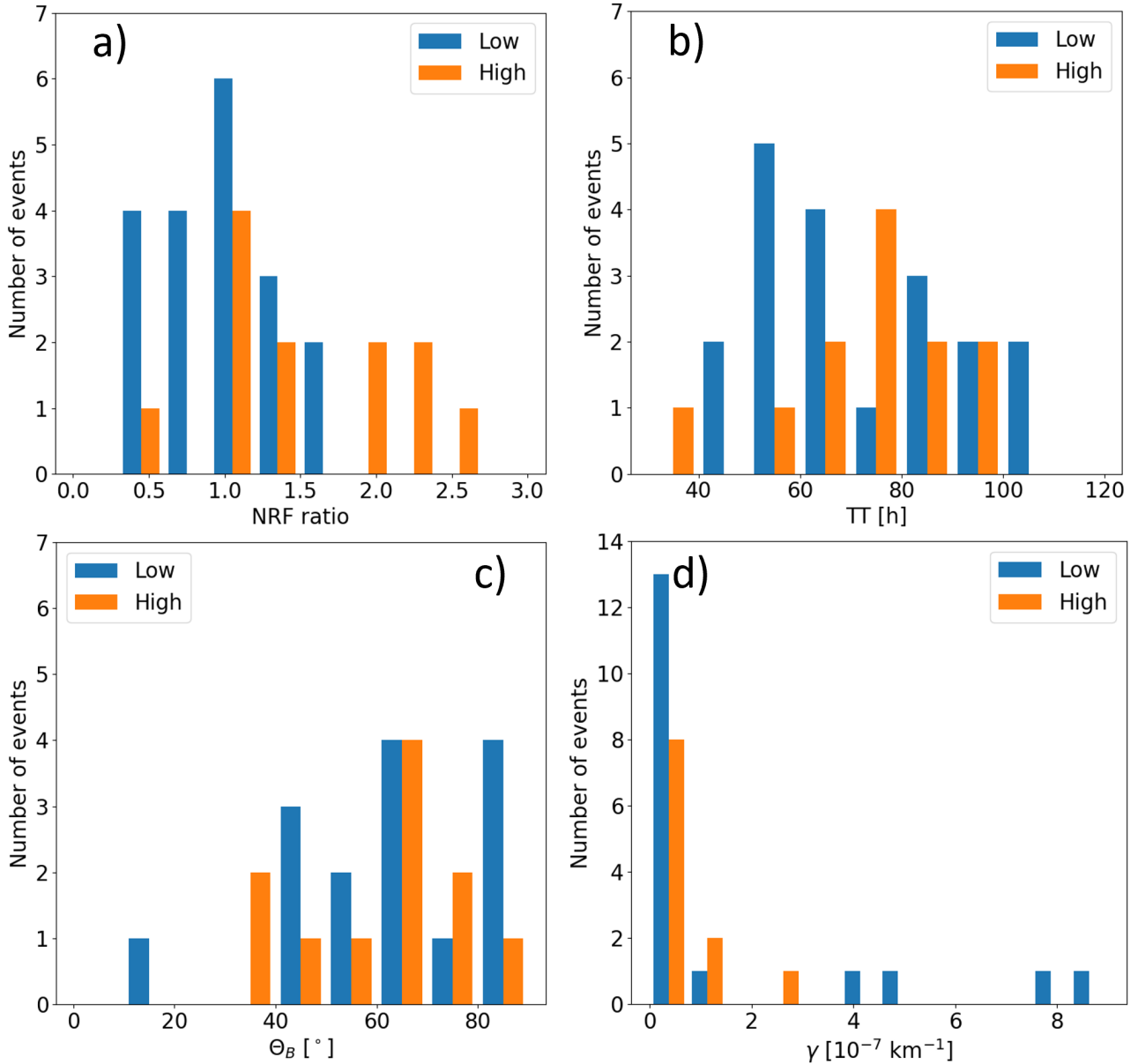


Fig. 4. Distributions for NRF ratio, transit time (TT), shock orientation (θ_B), and drag parameter γ for high-inclination events (orange) and low-inclination events (blue).

extent of the obstacle is smaller. For ICMEs with low inclination, the extent of the ICME FR part in the $\pm z$ direction is smaller than in the $\pm y$ direction, and therefore the NRF ratio is smaller for ICMEs with low inclination. In contrast, the extent of the ICME with high inclination is smaller in the $\pm y$ direction, so the plasma flows mainly in this direction. A sketch of

the various NRFs in terms of the different inclinations of CMEs is shown in Martinić et al. (2022). The result of Welch's test for the γ parameter is that the null hypothesis should not be rejected (i.e., the γ parameter for high- and low-inclination events comes from populations with equal means). Welch's test is based on the normality assumption, which is hardly satisfied for γ values

(see histogram in Fig. 4d). The Kolmogorov–Smirnov test and Mann–Whitney U -test, as nonparametric significance tests, were also performed. However, we note that both tests confirmed the results from Welch’s test at the same confidence interval (95%), meaning that there is no significant difference between low- and high-inclination events regarding γ values.

For shock orientation and transit time, the F -test confirmed similar variances for low- and high-inclination samples. Thus, instead of Welch’s test, the student t -test was performed under the assumption that (1) the shock orientation/transit time for high- and low-inclination events are independent, (2) the shock orientation/transit time distributions for low- and high-inclination samples are normal, and (3) the shock orientation/transit time variances for low-inclination and high-inclination events are similar (according to the F -test).

The t -test confirmed the null hypothesis at the 95% significance level, meaning that the samples of shock inclination and transit time for low- and high-inclination events come from populations with equal means. In other words, there is no statistically significant difference between low- and high-inclination groups of events.

The fact that there is no difference in the γ parameter and transit time for differently oriented CMEs suggests that the orientation of the CME does not affect the overall drag of the CME. However, we note that the drag depends primarily on the difference between the velocity of the CME and the ambient solar wind speed. In addition, the γ parameter depends on the CME cross section, the ambient solar wind density, the mass of the CME, and the virtual mass. It is possible that the effect of inclination is small enough to be “masked” by all these contributions, even though we selected the sample in order to minimize them. As described in Martinić et al. (2022), the inclination effect on the drag should be most pronounced at the minimum of the solar cycle, where the configuration of the IMF most closely matches that of a simple magnetic dipole. While our sample of events includes some that occurred near the minimum of solar activity (event numbers 11, 12, 13, 14, and 31), the majority of events correspond to the maximum, when the IMF configuration is very complex. Due to the very small sample of events at the minimum of solar activity, no analysis of the difference between events at the minimum and maximum of activity was performed.

Except for inclination influence, Vandas et al. (1995, 1996) also emphasized the importance of the chirality of the CME for its propagation, which is not captured by our study. This was later tackled by Chané et al. (2006), who studied the propagation of two CMEs: one in which the initial magnetic field and the background magnetic field had the same polarity and another where they had opposite polarities. Their simulations showed that the initial magnetic polarity significantly affects the evolution of CMEs. We note here that the study of Chané et al. (2006) did not examine the effects of CME inclination but rather the effects of initial chirality on propagation in the inner heliosphere. More recently, Shen et al. (2021) studied the effects of different initial CME densities, masses, sizes, and magnetic field configurations on simulation results for observers near Earth and Mars. Nevertheless, to our knowledge, there are no 3D MHD studies aimed specifically at investigating the effects of (I)CME inclination and its interaction with the environment, such as IMF draping and plasma flows ahead of the ICME. Such a study could beneficially complement our findings based on observations.

4. Summary and conclusions

Altogether, 31 Earth-directed CME-ICME pairs with distinct magnetic obstacle (MO) properties and pronounced sheath

regions during the period from 1997 to 2018 were studied. We inferred the dominant inclination from the ellipse fitting of LASCO-C2 and LASCO-C3 coronagraphic images. The dominant inclination was also derived from in situ data of the rotation of magnetic field components in the MO part of the ICME. Of the 31 CME-ICME pairs, 19 are low-inclination events, and 12 are high-inclination events.

Some basic features of the ICME propagation in terms of the inclination of the event were analyzed. We investigated the NRFs in the sheath region along with the shock orientation, transit time, and γ parameter. We found a significant difference in NRFs for differently oriented ICMEs. Low-inclination events were found to have lower NRF ratios, while high-inclination events were found to have higher NRF ratios. This implies that low-inclination events are more likely to have ambient plasma escape via the meridional plane, while high-inclination events are more likely to have plasma escape via the ecliptic plane (see Martinić et al. 2022).

The plasma deflection on the fast-forward shock could also contribute to the measured NRF ratios. To confirm that the above-stated difference between low- and high-inclination events is indeed due to the deflection of the plasma around the obstacle (ICME FR part) and not due to the deflection of the plasma by the shock front, we examined the dependence of the NRF ratios on the shock orientation. We found no differences in the NRF occurrence frequency with respect to the shock orientation, thus confirming the result stated above.

No significant difference was found in the transit time and γ parameter for differently oriented ICMEs. This suggests that the predominant inclination of the ICME has no effect on the drag due to the interaction with the ambient solar wind and IMF. We note that by inclination we mean tilt, that is, the angle between the elliptic plane and ICME flux rope axis, not the magnetic field orientation. We also emphasize that most of the studied events occurred near solar maximum, which is when the IMF has a very complex configuration. It is also possible that the influence of the inclination on the drag force is much smaller than the contributions of other features, such as the difference between the speed of the CME and the solar wind, the CME mass, the CME cross section, and the ambient density, and therefore the inclination effect is very difficult to decipher.

Acknowledgements. We acknowledge the support by the Croatian Science Foundation under the project IP-2020-02-9893 (ICOHOSS). K.M. acknowledges support by the Croatian Science Foundation in the scope of Young Researchers Career Development Project Training New Doctoral Students. N.A. acknowledges grants NSF AGS1954983 and NASA-ECIP 80NSSC21K0463. We also acknowledge the support from the Austrian-Croatian Bilateral Scientific Projects “Comparison of ALMA observations with MHD-simulations of coronal waves interacting with coronal holes” and “Multi-Wavelength Analysis of Solar Rotation Profile”. This paper uses data from the Heliospheric Shock Database, generated and maintained at the University of Helsinki. The SOHO/LASCO data used here are produced by a consortium of the Naval Research Laboratory (USA), Max-Planck-Institut fuer Aeronomie (Germany), Laboratoire d’Astronomie (France), and the University of Birmingham (UK). SOHO is a project of international cooperation between ESA and NASA. We acknowledge use of NASA/GSFC’s Space Physics Dana Facility’s OMNIWeb (or CDAWeb or ftp) service, and OMNI data.

References

- Abraham-Shrauner, B., & Yun, S. H. 1976, *J. Geophys. Res.*, **81**, 2097
- Al-Haddad, N., Nieves-Chinchilla, T., Savani, N. P., et al. 2013, *Sol. Phys.*, **284**, 129
- Al-Haddad, N., Galvin, A. B., Lugaz, N., Farrugia, C. J., & Yu, W. 2022, *ApJ*, **927**, 68
- Bothmer, V., & Schwenn, R. 1998, *Ann. Geophys.*, **16**, 1
- Breeckner, G. E., Howard, R. A., Koomen, M. J., et al. 1995, *Sol. Phys.*, **162**, 357

- Burlaga, L. F. E. 1991, in *Physics of the Inner Heliosphere II. Particles, Waves and Turbulence*, eds. R. Schwenn, & E. Marsch (Berlin: Springer), *Phys. Chem. Space*, 21, 1
- Byrne, J. P., Gallagher, P. T., McAteer, R. T. J., & Young, C. A. 2009, *A&A*, 495, 325
- Čalogović, J., Dumbović, M., Sudar, D., et al. 2021, *Sol. Phys.*, 296, 114
- Cargill, P. J. 2004, *Sol. Phys.*, 221, 135
- Cargill, P. J., Chen, J., Spicer, D. S., & Zalesak, S. T. 1996, *J. Geophys. Res.*, 101, 4855
- Chané, E., van der Holst, B., Jacobs, C., Poedts, S., & Kimpe, D. 2006, *A&A*, 447, 727
- Chen, J. 1996, *J. Geophys. Res.*, 101, 27499
- Chen, J., Howard, R. A., Brueckner, G. E., et al. 1997, *ApJ*, 490, L191
- Colburn, D. S., & Sonett, C. P. 1966, *Space Sci. Rev.*, 5, 439
- Delaboudinière, J. P., Artzner, G. E., Brunaud, J., et al. 1995, *Sol. Phys.*, 162, 291
- Dumbović, M., Čalogović, J., Martinić, K., et al. 2021, *Front. Astron. Space Sci.*, 8, 58
- Gopalswamy, N., Lara, A., Lepping, R. P., et al. 2000, *Geophys. Rev. Lett.*, 27, 145
- Gosling, J. T., & McComas, D. J. 1987, *Geophys. Rev. Lett.*, 14, 355
- Hess, P., & Zhang, J. 2015, *ApJ*, 812, 144
- Isavnin, A., Vourlidas, A., & Kilpua, E. K. J. 2013, *Sol. Phys.*, 284, 203
- Kay, C., & Gopalswamy, N. 2018, *J. Geophys. Res. Space Phys.*, 123, 7220
- Kay, C., Gopalswamy, N., Xie, H., & Yashiro, S. 2017, *Sol. Phys.*, 292, 78
- Kilpua, E. K. J., Isavnin, D., Vourlidas, A., Koskinen, H. E. J., & Rodriguez, L. 2013, *Ann. Geophys.*, 31, 1251
- Kilpua, E., Koskinen, H. E. J., & Pulkkinen, T. I. 2017, *Liv. Rev. Sol. Phys.*, 14, 5
- King, J. H., & Papitashvili, N. E. 2005, *J. Geophys. Res. Space Phys.*, 110, A02104
- Krall, J., & St. Cyr, O. C. 2006, *ApJ*, 652, 1740
- Lemen, J. R., Title, A. M., Akin, D. J., et al. 2012, *Sol. Phys.*, 275, 17
- Liu, Y., Manchester, W. B., Richardson, J. D., et al. 2008, *J. Geophys. Res. Space Phys.*, 113, A00B03
- Liu, Y., Luhmann, J. G., Bale, S. D., & Lin, R. P. 2011, *ApJ*, 734, 84
- Lundquist, S. 1950, *Ark. Fys.*, 2, 361
- Manoharan, P. K. 2006, *Sol. Phys.*, 235, 345
- Martinić, K., Dumbović, M., Temmer, M., Veronig, A., & Vršnak, B. 2022, *A&A*, 661, A155
- McComas, D. J., Gosling, J. T., Winterhalter, D., & Smith, E. J. 1988, *J. Geophys. Res.*, 93, 2519
- McComas, D. J., Gosling, J. T., Bame, S. J., Smith, E. J., & Cane, H. V. 1989, *J. Geophys. Res.*, 94, 1465
- Moore, R. L., Sterling, A. C., Hudson, H. S., & Lemen, J. R. 2001, *ApJ*, 552, 833
- Möstl, C., Rollett, T., Frahm, R. A., et al. 2015, *Nat. Commun.*, 6, 7135
- Müller, D., Nicula, B., Felix, S., et al. 2017, *A&A*, 606, A10
- Mulligan, T., Russell, C. T., & Luhmann, J. G. 1998, *Geophys. Rev. Lett.*, 25, 2959
- Nitta, N., & Mulligan Skov, T. 2017, *AGU Fall Meeting, Abstract SH51E-04*
- Owens, M., & Cargill, P. 2004, *Ann. Geophys.*, 22, 4397
- Palmerio, E., Kilpua, E. K. J., Möstl, C., et al. 2018, *Space Weather*, 16, 442
- Paouris, E., Čalogović, J., Dumbović, M., et al. 2021, *Sol. Phys.*, 296, 12
- Rodari, M., Dumbović, M., Temmer, M., Holzknecht, L., & Veronig, A. 2018, *Cent. Eur. Astrophys. Bull.*, 42, 11
- Rollett, T., Möstl, C., Temmer, M., et al. 2012, *Sol. Phys.*, 276, 293
- Sachdeva, N., Subramanian, P., Colaninno, R., & Vourlidas, A. 2015, *ApJ*, 809, 158
- Sachdeva, N., Subramanian, P., Vourlidas, A., & Bothmer, V. 2017, *Sol. Phys.*, 292, 118
- Salman, T. M., Lugaz, N., Farrugia, C. J., et al. 2020, *ApJ*, 904, 177
- Scherrer, P. H., Bogart, R. S., Bush, R. I., et al. 1995, *Sol. Phys.*, 162, 129
- Scherrer, P. H., Schou, J., Bush, R. I., et al. 2012, *Sol. Phys.*, 275, 207
- Sheeley, N. R., Walters, J. H., Wang, Y. M., & Howard, R. A. 1999, *J. Geophys. Res.*, 104, 24739
- Shen, F., Liu, Y., & Yang, Y. 2021, *ApJS*, 253, 12
- Siscoe, G., & Odstrcil, D. 2008, *J. Geophys. Res. Space Phys.*, 113, A00B07
- Temmer, M., & Bothmer, V. 2022, *A&A*, 665, A70
- Temmer, M., Rollett, T., Möstl, C., et al. 2011, *ApJ*, 743, 101
- Temmer, M., Vršnak, B., Rollett, T., et al. 2012, *ApJ*, 749, 57
- Temmer, M., Holzknecht, L., Dumbović, M., et al. 2021, *J. Geophys. Res. Space Phys.*, 126, e28380
- Thernisien, A. F. R., Howard, R. A., & Vourlidas, A. 2006, *ApJ*, 652, 763
- Vandas, M., Fischer, S., Dryer, M., Smith, Z., & Detman, T. 1995, *J. Geophys. Res.*, 100, 12285
- Vandas, M., Fischer, S., Dryer, M., Smith, Z., & Detman, T. 1996, *J. Geophys. Res.*, 101, 2505
- Vourlidas, A., Colaninno, R., Nieves-Chinchilla, T., & Stenborg, G. 2011, *ApJ*, 733, L23
- Vršnak, B. 2001, *Sol. Phys.*, 202, 173
- Vršnak, B., Ruždjak, D., Sudar, D., & Gopalswamy, N. 2004, *A&A*, 423, 717
- Vršnak, B., Žic, T., Vrbanec, D., et al. 2013, *Sol. Phys.*, 285, 295
- Wu, S. T., Han, S. M., & Dryer, M. 1979, *Planet Space Sci.*, 27, 255
- Wu, S. T., Dryer, M., & Han, S. M. 1983, *Sol. Phys.*, 84, 395
- Xie, H., Gopalswamy, N., & Akiyama, S. 2021, *ApJ*, 922, 64
- Yurchyshyn, V., Abramenko, V., & Tripathi, D. 2009, *ApJ*, 705, 426
- Zhou, Y., Feng, X., & Zhao, X. 2014, *J. Geophys. Res. Space Phys.*, 119, 9321
- Žic, T., Vršnak, B., & Temmer, M. 2015, *ApJS*, 218, 32

2.3 Probing coronal mass ejections inclination effects with EUHFORIA



Probing Coronal Mass Ejection Inclination Effects with EUHFORIA

Karmen Martinić^{1,5} , Eleanna Asvestari^{2,5} , Mateja Dumbović¹ , Tobias Rindlisbacher³ , Manuela Temmer⁴ , and Bojan Vršnak¹ 

¹ Hvar Observatory, Faculty of Geodesy, University of Zagreb, Kačićeva ulica 26, 10 000 Zagreb, Croatia

² Faculty of Science, Department of Physics, University of Helsinki, Gustaf Hällströmin katu 2, Helsinki, Finland

³ Albert Einstein Center for Fundamental Physics, Institute for Theoretical Physics, University of Bern, Sidlerstrasse 5, CH-3012 Bern, Switzerland

⁴ Institute of Physics, University of Graz, Universitätsplatz 5, 8010 Graz, Austria

Received 2024 May 17; revised 2024 July 22; accepted 2024 August 23; published 2024 October 14

Abstract

Coronal mass ejections (CMEs) are complex magnetized plasma structures in which the magnetic field spirals around a central axis, forming what is known as a flux rope (FR). The central FR axis can be oriented at any angle with respect to the ecliptic. Throughout its journey, a CME will encounter interplanetary magnetic fields and solar winds that are neither homogeneous nor isotropic. Consequently, CMEs with different orientations will encounter different ambient medium conditions and, thus, the interaction of a CME with its surrounding environment will vary depending on the orientation of its FR axis, among other factors. This study aims to understand the effect of inclination on CME propagation. We performed simulations with the EUHFORIA 3D magnetohydrodynamic model. This study focuses on two CMEs modeled as spheromaks with nearly identical properties, differing only by their inclination. We show the effects of CME orientation on sheath evolution, MHD drag, and nonradial flows by analyzing the model data from a swarm of 81 virtual spacecraft scattered across the inner heliospheric. We have found that the sheath duration increases with radial distance from the Sun and that the rate of increase is greater on the flanks of the CME. Nonradial flows within the studied sheath region appear larger outside the ecliptic plane, indicating a “sliding” of the interplanetary magnetic field in the out-of-ecliptic plane. We found that the calculated drag parameter does not remain constant with radial distance and that the inclination dependence of the drag parameter cannot be resolved with our numerical setup.

Unified Astronomy Thesaurus concepts: Solar coronal mass ejections (310); Magnetohydrodynamical simulations (1966); Solar physics (1476); Heliosphere (711)

1. Introduction

Coronal mass ejections (CMEs) are massive expulsions of plasma and magnetic fields from the solar corona into interplanetary space (IPS). While traveling through the IPS, CMEs are also referred to as interplanetary CMEs (ICMEs) and are known for their potential geoeffectiveness (J. T. Gosling et al. 1990; J. Zhang et al. 2003; H. E. J. Koskinen & K. E. J. Huttunen 2006; M. Dumbović et al. 2015). The magnetic core of (I)CMEs is known to be a twisted flux rope (FR; L. Burlaga et al. 1981; R. P. Lepping et al. 1990; A. Vourlidas et al. 2013), namely, a cylindrical structure whose poloidal magnetic field component wraps around an axial magnetic field that follows the central axis of the cylinder (S. Lundquist 1950).

During their propagation in the corona and the heliosphere, (I)CMEs interact with the surrounding solar wind (SW) and the interplanetary magnetic field (IMF). As a result of this interaction, and in combination with the FR expansion, a so-called sheath region is formed ahead of the FR (G. Siscoe & D. Odstrčil 2008). This highly compressed and turbulent part of the (I)CME usually exhibits increased magnetic field, temperature, and density, which has strong fluctuations (E. Kilpua et al. 2017). (I)CME sheath regions are known for their

geoeffectiveness (B. T. Tsurutani et al. 1988; K. E. J. Huttunen et al. 2002; K. E. J. Huttunen & H. E. J. Koskinen 2004) and are therefore very important to study for advancing space weather forecasts.

Sheath regions consist of draped IMF and accumulated SW plasma in front of the FR driver. J. T. Gosling & D. J. McComas (1987) introduced a concept of IMF draping around (I) CMEs in IPS, analogous to the draping of IMF around planets and comets forming various plasma sheaths. They developed a theory based on the draping of the radial and transverse IMF components. In the case of the radial one, it is related to the Gosling–McComas rule according to which the amplification of the negative B_z perturbations occurs in the (I)CME sheath region. There are two cases when negative B_z occurs: (1) in front of a northward directed (I)CME that is embedded in sunward (inward pointing—negative) radial IMF (see Figure 3 in J. T. Gosling & D. J. McComas 1987) and (2) in front of the southward directed (I)CME that is embedded in antisunward (outward pointing—positive) IMF. D. J. McComas et al. (1989) reported a strong out-of-ecliptic magnetic field component in the sheath region of an observed (I)CME and discussed that this is a consequence of a draped magnetic field pattern following the deflection of the surrounding plasma in front of the FR driver. However, the draping is a complex 3D pattern in which both radial and transverse magnetic field components are draped around the embedded (I)CME. The draping of the transverse magnetic field component leads to two additional mechanisms: the eastward deflection of fast (I) CMEs (J. T. Gosling et al. 1987) and B_z perturbations due to the pressure gradient that shifts the accumulated field lines

⁵ These authors contributed equally to this work.



perpendicular to the direction of motion of the (I)CME. G. Siscoe et al. (2007) employed simulations to analyze the draping of the transverse IMF component for fast CMEs. They found that the magnetic field is weaker on the eastern side and stronger on the western side of the (I)CME front. They also concluded that, at higher latitudes, the latitudinal component of the magnetic field is stronger on the eastern side. This is a consequence of the existence of the Parker spiral, i.e., the draping of the transverse magnetic field component, where a stronger draping of the IMF occurs on the western side and a “slipping” of the field lines on the eastern side of the (I)CME front is a more probable process.

More recently, K. Martinić et al. (2022) and K. Martinić et al. (2023) studied different drag and the different plasma outflows (i.e., the different draping patterns) experienced by CMEs with different inclinations (CMEs inside and outside the ecliptic plane), assuming that IMF is “frozen-in” the SW plasma. They found observational evidence for differences in the nonradial flows in the CME sheath region for differently inclined CMEs. However, no evidence was found for a difference in drag for CMEs of different inclinations. M. Vandas et al. (1995) and M. Vandas et al. (1996) performed magnetohydrodynamic (MHD) simulations of two differently inclined magnetic clouds. Details of the MHD model used can be found in S. T. Wu et al. (1979; for 2D simulations) and in S. T. Wu et al. (1983; for 2.5D simulations). Their results show that the trajectory of these magnetic clouds is unaffected by the alignment of their axes with the ecliptic plane, regardless of whether one of the two axes lies within the ecliptic and the other has an axis perpendicular to it. However, it is important to note that the MHD model they used was limited to the equatorial plane of the Sun and did not provide a comprehensive 3D MHD representation.

This study aims to fill the gap in understanding the effects of inclination on propagation within the heliosphere by performing simulations using the European Heliospheric FORecasting Information Asset (EUHFORIA) 3D MHD model (J. Pomoell & S. Poedts 2018). Considering the limitations in observing and isolating the effects of CME inclination highlighted in K. Martinić et al. (2022) and K. Martinić et al. (2023), this research will simulate two CMEs with nearly identical properties, differing only in their inclination, using the spheromak CME representation in EUHFORIA (C. Verbeke et al. 2019). In Section 2, we first present the numerical setup for the simulations and discuss the determination of the spheromak boundaries in Section 3. In Sections 4 and 5, we discuss, respectively, the importance of the spheromak tilt instability and the drag parameter γ . The sheath evolution, nonradial flows, and the drag parameter γ for two differently inclined spheromaks are shown and discussed in Section 6. Finally, a summary of the main results is given in Section 7.

2. Numerical Setup

For this study, we generated simplistic solar wind plasma and IMF conditions with the EUHFORIA MHD model. At the inner boundary, set at 0.1 au, we input a uniform, weak, and outward-pointing (positive) radial IMF, of $B_r = 100$ nT. The selection of this weak IMF was chosen to minimize the tilting and deflecting effects of the IMF on the spheromak (see E. Asvestari et al. 2022, for more details on these phenomena). As argued in E. Asvestari et al. (2022), although this unidirectional IMF topology is not realistic for the global 3D

heliosphere, it can be a valid topology for the small region where an FR is injected and through which it propagates. The plasma parameters at the inner boundary are set at $v_r = 400.0$ km s⁻¹ for the radial velocity component and $P = 3.3$ nPa for the thermal pressure, a representative of the average properties of a slow solar wind at the inner boundary. Based on these two parameters the number density was calculated using Equation (4) in J. Pomoell & S. Poedts (2018) giving $n = 7.32 \cdot 10^8$ m⁻³. Subsequently, using the number density and plasma pressure, the plasma temperature was calculated and found to be at $T = 3.26 \cdot 10^5$ K. For the grid resolution of the 3D domain, we set 512 radial grid points from 0.1 au to 2.0 au, and 4° resolution in co-latitude and longitude. We performed two simulations, one with a spheromak inserted with a 0° tilt angle (low inclination), and one at a 90° tilt angle (high inclination). The tilt angle is defined as an angle between the solar equatorial plane and the toroidal axis of the spheromak. Both spheromak structures were set to have a positive helicity and were inserted at 0° longitude and latitude (Sun–Earth line), with a radius of $10 R_\odot$. For the magnetic flux and temperature of the spheromak, we opted to use default EUHFORIA values, which are $80 \cdot 10^{12}$ Wb and $0.8 \cdot 10^6$ K, respectively (C. Verbeke et al. 2019). To further minimize the rotation of the spheromak due to the ambient magnetic field we opted for modeling the spheromak having a relatively high density of $\rho = 0.5 \cdot 10^{-17}$ kg m³ (M. Temmer et al. 2021), thus more inertia/harder to rotate, and which are faster, $v = 1500.0$ km s⁻¹, thus escaping quickly from the inner heliosphere where the ambient field is stronger and has a greater impact (see E. Asvestari et al. 2022; R. Sarkar et al. 2024, for more details).

By choosing a simple, unidirectional configuration of the surrounding magnetic field, we avoid the occurrence of the heliospheric plasma sheath (HCS) in the simulation. E. J. Smith (2001) and M. Temmer et al. (2023) emphasize the complexity and importance of studying the interaction between the HCS and the CMEs. It is known that CMEs deflect toward the HCS (C. Kay et al. 2015; J. Wang et al. 2023), align their axis with the local orientation of the HCS (V. Yurchyshyn 2008; V. Yurchyshyn et al. 2009) and cause FR erosion through reconnection (e.g., S. Dasso et al. 2006; A. Ruffenach et al. 2015; S. Pal et al. 2021). As EUHFORIA is an ideal MHD model, we do not anticipate physical reconnection to take place. However, reconnection may occur in the simulation domain due to numerical diffusion caused by the grid resolution and/or the numerical solver. The grid resolution mainly affects the HCS, which, although it should be infinitesimal in thickness, is smeared, resulting in a numerical resistivity that can lead to reconnection. Additionally, the configuration of the ambient field (pointing radially outward) and helicity of the spheromaks (positive helicity) is chosen to minimize the occurrence of the antiparallel magnetic field lines of the spheromak’s poloidal field and the ambient magnetic field in the simulation.

To study the spheromak’s inclination effects on its evolution and on the draping of IMF at its sheath at different distances from the Sun and different locations at its front and flanks we inserted virtual spacecraft (VS) in the simulations. The spacecraft names do not reflect their location; they are just assigned to different lon-/lat-positions. Overall we inserted 81 VS, grouped into nine families. Each family consists of nine VS with identical longitudinal/latitudinal coordinates but

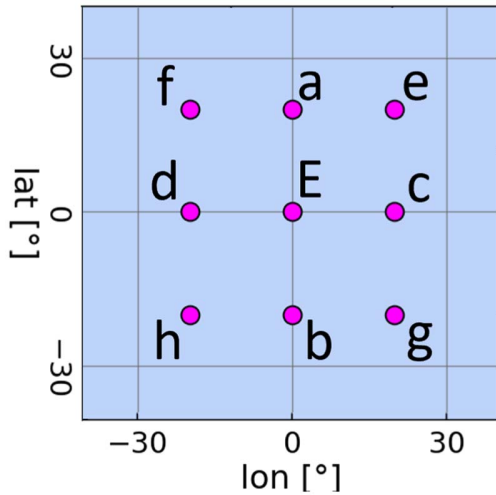


Figure 1. Longitudinal and latitudinal distribution of the virtual spacecraft swarm used in EUHFORIA simulations for particular radial distance.

having different radial distances from the Sun. The labeling scheme for the nine VS families is shown in Figure 1. As can be seen in this figure we placed one VS along the Sun–Earth line (0° in longitude and latitude), which is noted as VS-E, and eight VS (a–h) in a square grid around VS-E, using longitudinal and/or latitudinal separations of 20° (see Figure 1). This spacecraft constellation is repeated for radial distances of 0.32 au, 0.42 au, 0.52 au, 0.62 au, 0.72 au, 0.92 au, and 1.00 au, determined by the grid resolution. The coordinate system in the simulations is in Heliocentric Earth Equatorial (HEEQ).

3. Spheromak Boundary Determination

For our analysis, it was essential to determine, at each VS location, the boundaries between undisturbed solar wind, shock sheath, and FR regions, namely, the start and end time of the sheath region and of the FR, hereafter referred to as the magnetic obstacle (MO). To do that we employed two methods; the first was based on analyzing the plasma β parameter in the time series at each VS, similar to criteria observers use with in situ measurements. This approach is based on the fact that within the MO part of the (I)CME, the magnetic pressure dominates over the plasma pressure, while the opposite applies in the sheath region. The second method focused on analyzing the 3D structure in the modeling domain. More details on this approach are given later in this section.

In the first method, the onset time of the sheath is determined by the sudden increase of the plasma β parameter, i.e., a 50% increase in the plasma β values compared to the mean of the preceding 35 plasma β values in the solar wind. The end of the sheath is defined as a sudden increase in the plasma β parameter, relative to the mean of the trailing 35 plasma β values in the solar wind, when iterating from the back of the time series. We note that this sheath end boundary would be seen as a sudden decrease in the plasma β parameter, if we start from the beginning of the time series. This criterion for determining the sheath boundaries is based on evidence that the plasma β parameter in the sheath region increases in (I)CMEs examined in situ (E. Kilpua et al. 2017, and reference therein). The start of MO was determined at a point where the plasma β falls below one, and the end at the time at which it reaches a

value greater than one again. The same condition for obtaining MO boundaries based on the EUHFORIA simulation output with spheromak was applied in R. Sarkar et al. (2024).

Figure 2 shows the in situ profiles for VS-E and VS-d located at $r = 1$ au for a spheromak with high inclination (tilt = 90°). From top to bottom, the panels display the magnetic field magnitude and its components in the radial-tangential-normal (RTN) coordinate system (top row), the proton number density and the temperature (middle row), the velocity and the plasma β parameter (bottom row). The left column shows the values for VS-E and the right for VS-d. In addition, five (for right panels) and six (for left panels) vertical lines can be seen in the figure. These mark the boundaries of different (I)CME signatures. The sheath, which was derived solely on the basis of the plasma β parameter, is marked with two red vertical lines. The two blue vertical lines mark the beginning (left line) and end (right line) of the MO, again, solely based on the plasma β parameter. The green vertical line marks the start of the MO derived based on the second approach described below. The end of the MO, based on the second approach, is set only for VS-E because only this boundary is used in Section 5 to derive the drag parameter γ .

The second method focuses on analyzing the entire spheromak structure in the 3D simulation output. These boundaries are marked by the green vertical lines in Figure 2 which correspond to the beginning and the end of the MO derived by analyzing the 3D spheromak structure based on the magnetic field and magnitude of the plasma pressure gradient. More precisely we employed an improved version of the spheromak detection and tracking method described in E. Asvestari et al. (2022). As the different structures of the (I)CME were traversing a VS, the quantities of interest were monitored along three perpendicular cut planes, centered at the VS location and oriented to be parallel to the HEEQ coordinate planes. First, we looked into the magnitude of the pressure gradient $|\nabla P|$, an example of which is shown in Figure 3 for VS-d for a spheromak of low inclination. As can be seen, we can identify two thin shells of the increased magnitude of the plasma pressure gradient. In between these two shells, the pressure gradient vanishes (in the perpendicular direction to the shells’ surfaces), since the pressure itself peaks along the interface between CME and ambient solar wind, where they push directly against each other. The start of the first shell marks the start of the sheath region, while the start of the second shell marks the beginning of the MO. Therefore, tracking the arrival of each shell at the VS location, the center of the grid cross in all panels, helps us to extract the start times. It is important to mention that the wiggles these shells exhibit are due to the grid resolution and the manifestation of numerical artifacts. In the case of the MO, we looked also at the magnetic flux density as a vector field. An example is shown in Figure 4 for the same VS-d as in Figure 3. The moment at which the spheromak arrives at the VS is determined by picking the time at which the spheromak’s magnetic field becomes visible in all three panels (which are cut planes through the VS location). The example in Figure 4 shows such a moment since the spheromak’s poloidal field just started to appear in the top-right panel.

Using the same plot we could determine the end of the FR. To do that we need to consider that the spheromak FR structure is “ring-shaped,” which means that the leading FR is followed by a trailing one with a mirrored poloidal component and an

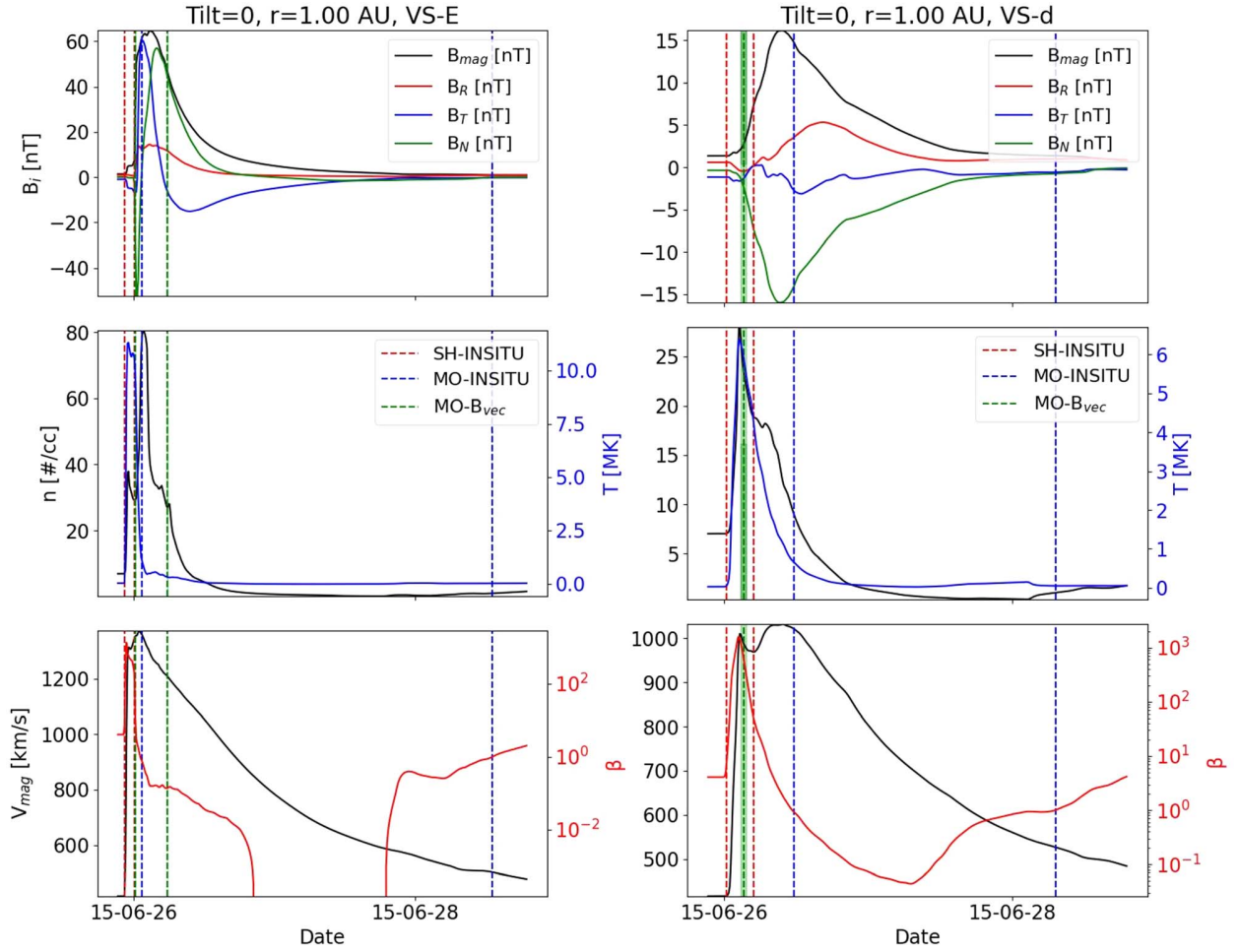


Figure 2. In situ data as seen by VS-E (left panels) and VS-d (right panels) for 1 au distance. The top panels show magnetic field magnitude and magnetic field components in the RTN coordinate system. Middle panels show proton number density and temperature. The bottom panels show velocity and plasma β parameters. The pair of red vertical boundaries mark the sheath region (SH-INSITU), the pair of blue vertical boundaries mark the MO part based on the plasma β parameter (MO-INSITU), first green vertical line marks the beginning of the MO part but based on the magnetic flux density as a vector field (MO-B_{vec}), while the second green vertical line (only present for VS-E, left panels) marks the end of the spheromak also derived on the basis of the magnetic flux density as a vector field (MO-B_{vec}).

antiparallel toroidal one. This double FR structure is known to not represent the commonly accepted geometry of the MO of (I)CMEs and thus we only want to consider the leading FR in our analysis. Consequently, to determine the end of the MO we consider the time the spacecraft crosses the poloidal field for the second time. The end of the MO was derived with a higher temporal resolution of the 3D simulation output, 5 minutes, but only for VS-E, as shown in Figure 2, left panels. The end of the spheromak was needed only for VS-E to derive the drag parameter γ as described in Section 5, and thus for other VS the end of the MO is not determined. The green shaded area around the green vertical line marking the beginning of the MO (for all VS, except for VS-E for which higher resolution simulation output was used) in Figure 2 represents the temporal resolution of the images we used to derive the beginning of the MO, i.e., it corresponds to ± 30 minutes from the set boundary time as shown in the right panels of Figure 2. To summarize, using the second method, the beginning of the MO was derived for all VS, while the end of the MO was derived only for VS-E. Also, for VS-E MO boundaries based on the second method were derived with higher simulation output cadence—5 minutes.

In Figure 2 (left panels), we can also see that the boundaries of the end of the MO, derived by the two different methods

explained, do not coincide. This is a direct consequence of the spheromak’s toroidal geometry. The end of the MO with the green vertical line is located in the center of the toroid of the spheromak and the rear part of the toroidal magnetic body is not considered, which is not the case when estimating the boundary of the MO solely based on the plasma β parameter in in situ time series (second blue vertical line). Note that in the simulations the spheromak does not retain its spherical geometry. Instead, it expands and pancakes as it interacts with the ambient solar wind, resulting in a compressed front and a sunward stretched trailing portion. This explains why the green line marking the end of the MO in Figure 2 (left panels) is close to the front and not at the midpoint of the spheromak FR signature in the time series.

The in situ profiles with all corresponding boundaries and for all spacecraft (overall the different radial distances in the simulation), for high- and low-inclination spheromaks, can be found at the following link: doi:[10.6084/m9.figshare.25849135](https://doi.org/10.6084/m9.figshare.25849135). We point out that for VS-a and VS-e, in the case of the high-inclination spheromak, and for VS-c and VS-g, in the case of the low-inclination spheromak, the end of the sheath (second red vertical line) has been manually derived due to simulation artifacts occurring just after the MO part of the spheromak.

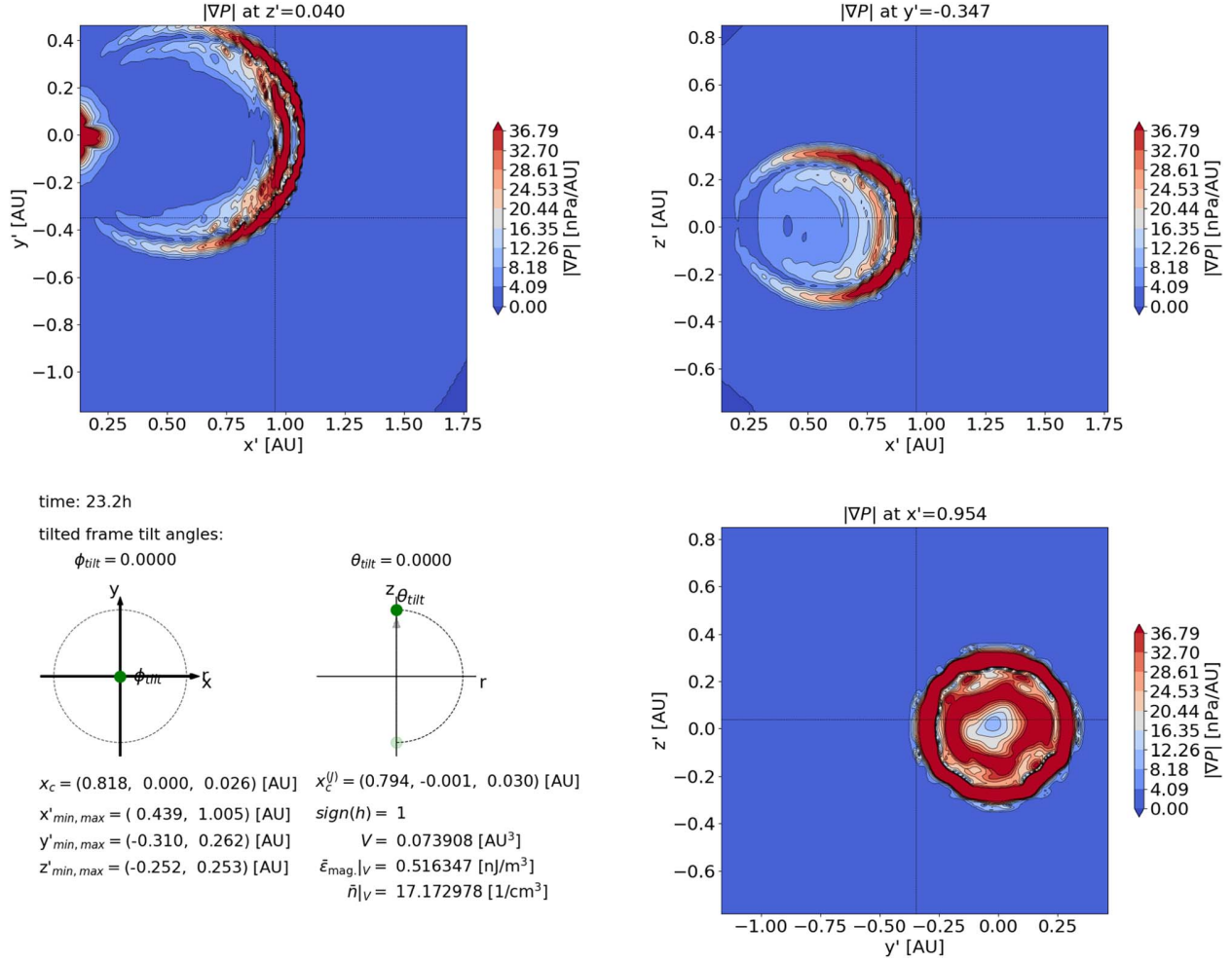


Figure 3. Magnitude of the pressure gradient in a neighborhood of VS-d in the low-inclination spheromak simulation, visualized along three perpendicular slices (two top and bottom-right panels). The three slices are selected so that VS-d is located at their centers (grid cross). The x' - y' - z' coordinate system, specified by the orientation of the slices, agrees here with HEEQ (x - y - z). The bottom-left panel shows information about the spheromak's center location, extent, helicity, volume, average magnetic field energy, and mass, as determined by the detection tool. The angles ϕ_{tilt} and θ_{tilt} specify the orientation of the x' - y' - z' coordinate system relative to the HEEQ x - y - z coordinates.

Furthermore, we note that for some spacecraft, the MO boundaries based on the β parameter of the plasma (blue vertical lines) are not set. This is because, in some in situ profiles, there is no plasma β less than one. Details on the manually derived end of the sheath and the examples of in situ profiles where plasma β does not fall below one are shown in Appendix A. Plots of the plasma β parameter across all radial distances with corresponding MO and sheath boundaries overplotted for both, the high- and low-inclination spheromaks are given in the following link: doi:10.6084/m9.figshare.25849135.

4. Manifestation of Spheromak Tilting and Drifting

In E. Asvestari et al. (2022) it was shown that, when inserted into the interplanetary magnetic field, the spheromak can start rotating (tilting) due to a torque forcing it to align its magnetic moment to the direction of the ambient magnetic field, which in the heliospheric MHD simulations is the IMF. Furthermore, the spheromak drifts away from its initial direction of propagation. To minimize this rotation and drift, we opted, as mentioned in Section 2, for inserting rather heavy spheromaks in the simulation domain, with mass densities of $0.5 \cdot 10^{-17}$ kg m³. This is a similar approach to R. Sarkar et al. (2024). The

reasoning behind this choice is that a heavier spheromak has a larger moment of inertia than a lighter spheromak of the same size, and will therefore experience less rotational acceleration when subject to the same torque. Similarly, more mass means more inertia and therefore less acceleration/deflection when subject to the same force. Of course, the rotation is not completely prevented but heavily reduced. In the cases we studied, the evolution of the orientation of the two spheromaks simulated with EUHFORIA, with low and high inclinations, is shown, respectively, in the left- and right-hand panels of Figure 5. For simplicity, we sketch the spheromak in their idealized representation. The arrow running through the center of the spheromak is its magnetic moment, indicating the orientation of the poloidal field at the center of the spheromak. As the spheromak tilts due to the torque exerted on it by the IMF, the orientation of this arrow changes accordingly. As can be seen in the left-hand panel, for the low-inclination spheromak, there is a slight eastward and southward tilting, while for the high-inclination spheromak in the right-hand panel, we see a slight northward and very small, basically negligible, westward tilting. This is because for both cases the IMF, depicted as a swarm of gray arrows, is positive and thus

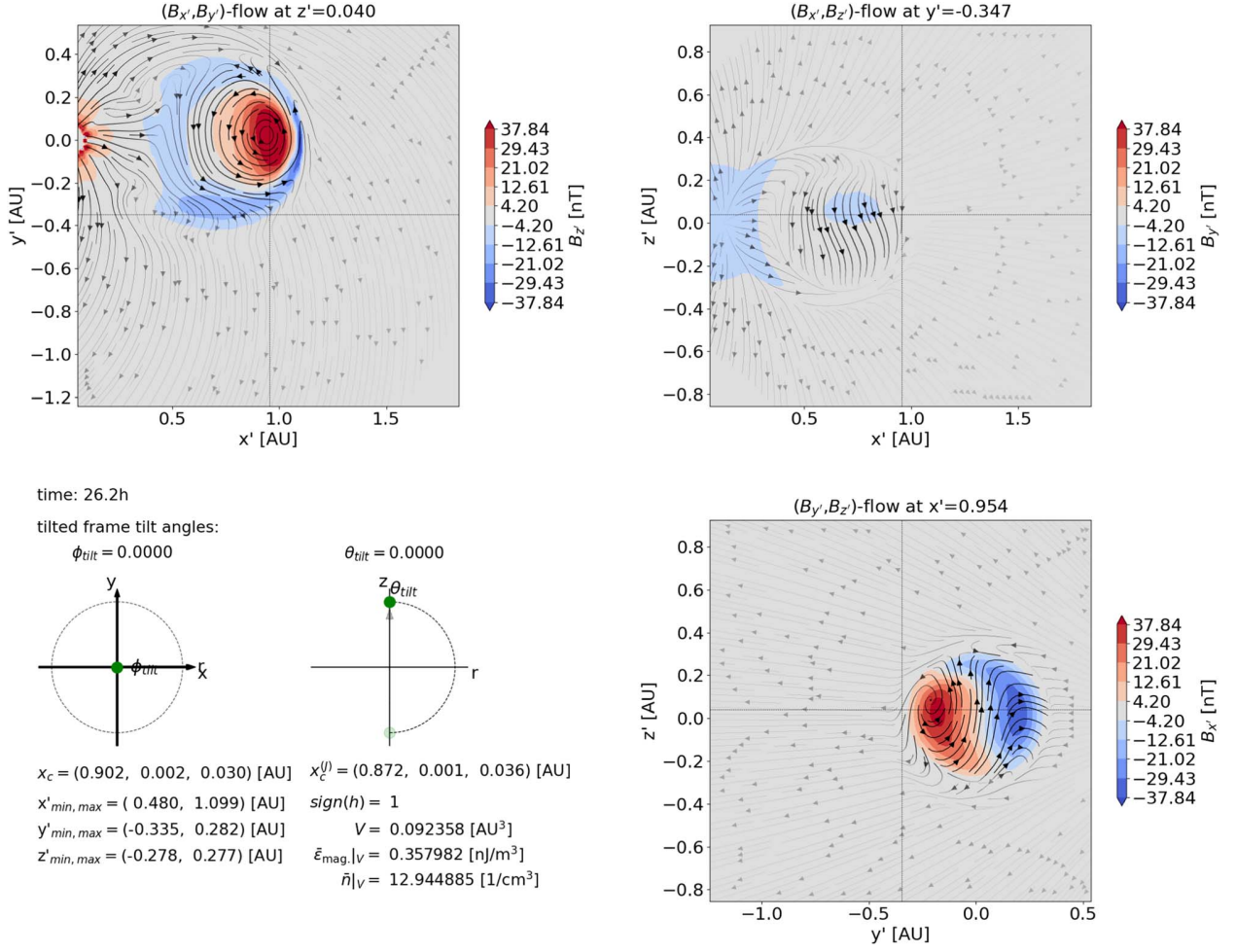


Figure 4. Vector field indicating the division between spheromak FR and IMF for VS-d in the low-inclination spheromak simulation. Same as in the previous figure, the three slices are selected so that the spacecraft being analyzed is located at the center of the images (grid cross).

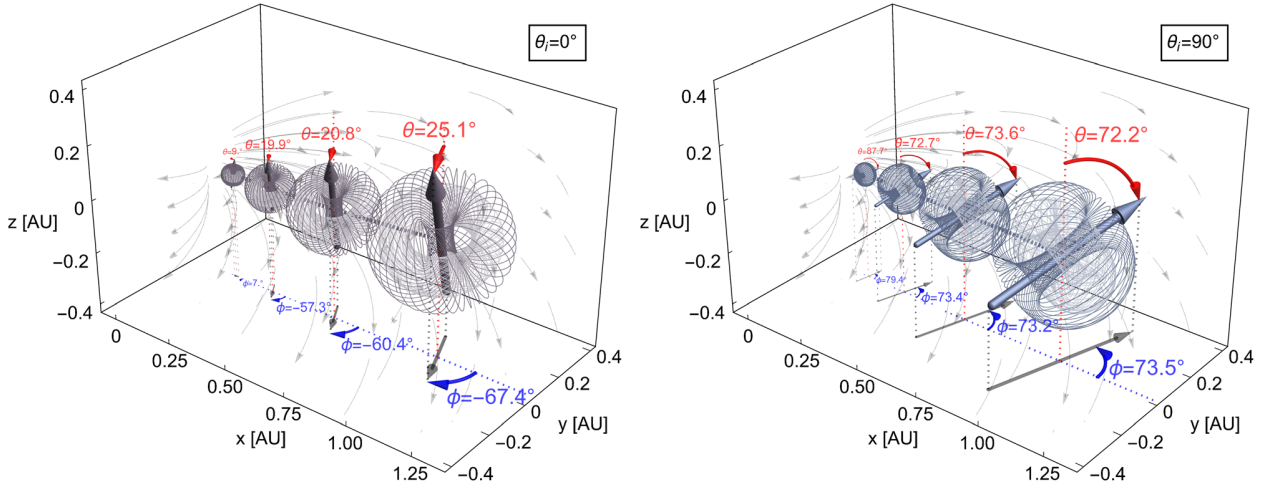


Figure 5. Visual representation of how the spheromaks of low inclination (left panel) and high inclination (right panel) have tilted from their original orientations due to the torque exerted on them by the ambient magnetic field. For simplicity, we sketch the spheromaks in their idealized representation and at only 80% of their actual size to avoid overlap. The arrow running through the center of the spheromak represents its magnetic moment, indicating the orientation of the poloidal field at the center of the spheromak. The change of orientation of this arrow illustrates the spheromak tilting toward the IMF direction (gray arrows). This tilting is quantified by two angles, θ (red) and ϕ (blue), where θ is the angle the magnetic moment forms with the z -axis and ϕ is the angle the projection of the magnetic moment on the x - y plane forms with the x -axis. The evolution of these angles over the full simulation time can be found in Figure 6 below.

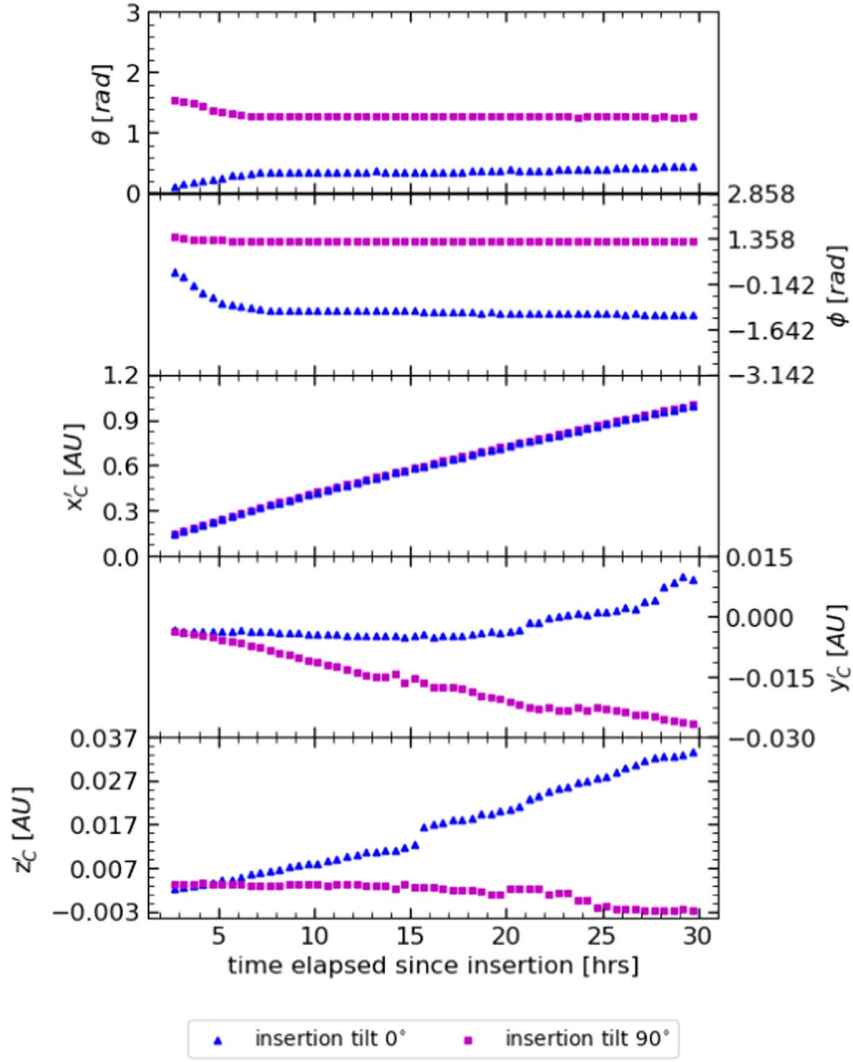


Figure 6. Evolution of the spheromak orientation due to the torque causing it to tilt (first and second panels from the top), and its drifting motion indicated by the change of the location of its center of mass in the x' , y' , and z' coordinates (third to fifth panels from the top). The first panel from the top shows the spheromak tilting from the solar north toward the solar equatorial plane (θ_{tilt}), while the second panel shows the tilt in the solar equatorial (x - y) plane ϕ_{tilt} .

points away from the Sun, while at the same time, it curves forming the Parker spiral. The tilt and the drift of the two spheromaks modeled can also be seen in the time series presented in Figure 6.

The two upper panels show the time evolution of spheromak tilt, represented by the two angles θ and ϕ (see bottom-left panel of Figure 9). As can be seen, the overall change in θ is for both spheromaks relatively small and occurs primarily during the first 5–7 hr, while propagating below 0.3 au. After that distance, the variations become almost unnoticeable. The third to fifth panels show, respectively, the time evolution of the x , y , and z coordinates of the spheromaks' centers of mass. As can be seen, the drift in the y - and z -directions remains for both spheromaks very small, of the order of 10^{-2} au. This small-scale drift in the y - and z -direction is of the opposite direction for different-inclination spheromaks, the low-inclination spheromak drifts westward, and the high-inclination spheromak drifts eastward (see 4th panel of Figure 6). Similarly, as can be seen from the bottom panel of Figure 6 the low-inclination spheromak drifts slightly northward, and the high-inclination

spheromak drifts slightly southward, but such southward drift is almost negligible.

5. Drag Parameter γ Determination

Studies based on observations have revealed that the drag force becomes the dominant factor governing the propagation of (I)CMEs within specific distances in the heliosphere. Several drag-based models for (I)CMEs have been established based on these findings (B. Vršnak et al. 2013; C. Kay et al. 2013; C. Mostl et al. 2015; P. Hess & J. Zhang 2015). These models commonly utilize a simple analytical equation:

$$a_d = -\gamma(v - w)|v - w|, \quad (1)$$

where v denotes the CME velocity, w represents the solar wind velocity, and γ stands for the drag parameter calculated using the equation (e.g., B. Vršnak et al. 2013):

$$\gamma = \frac{C_d}{L(\rho/\rho_w + 1/2)}. \quad (2)$$

Here, L corresponds to the radial cross section of the (I)CME MO part, ρ is (I)CME MO enclosed density, ρ_w the ambient solar wind density, and C_d the dimensionless drag coefficient. Notably, C_d is often assumed to be constant and set to one throughout the (I)CME propagation. However, P. J. Cargill (2004) demonstrated that the value of C_d depends on the relative density and velocity of the (I)CME with regard to the solar wind. Cargill's work highlighted that for dense CMEs, C_d remains close to one, whereas for low-density (I)CMEs, it can increase to as high as three, exhibiting significant radial dependence in the latter case.

The drag parameter γ plays a crucial role in understanding the drag force acting on an (I)CME. From the EUHFORIA simulation, we can derive the density ratio ρ/ρ_w for each VS at each radial distance from the Sun in the heliosphere. The radial cross section, L , can also be derived from simulation results. From in situ representation, L is given as the duration of the MO multiplied by the mean plasma velocity inside the MO as observed by the VS. We note here that the above-given representation of the drag parameter γ assumes locally cylindrical geometry where L is 2 times the radius of the base of the cylinder (for details see B. Vršnak et al. 2013 and P. J. Cargill 2004), and to be the closest to this idealization we only calculated the cross section L from green MO boundaries displayed in Figure 2. This way we avoid a double FR crossing due to the spheromak "ring-shaped" toroidal magnetic body. The parameter ρ is taken as a median of the density measurements at the VS and ρ_w is the mean density before the (I)CME sheath onset (mean ambient density). Finally, C_d is assumed to be constant and is set to one.

6. Results and Discussion

6.1. Evolution of the Sheath Region

Figure 2 shows that for VS-E the end of the sheath (second red vertical line) and the start of the MO (first green vertical line) coincide. However, this is not the case for VS-d. We see that in this case, the MO start (first vertical green line) is before the estimated end of the sheath (second red vertical line). As a reminder for the reader, the end of the sheath was based solely on the plasma β while the start of the MO was derived based on the magnetic field vector flow. Therefore, the fact that the start of the MO was found to be before the determined end of the sheath means that the plasma β parameter stays increased within the beginning of the MO. Within this region (between the first green vertical line and the second red vertical line), as shown in Figure 2 (right panels) we see a gradual decrease in velocity, while temperature and number density show a rapidly decreasing profile similar to plasma β parameter. B. Vršnak et al. (2016) studied early FR evolution in the solar corona in the 2.5D MHD setting and found a sharp density peak in front of the FR represents the contact surface, i.e., the edge of the FR where the density pileup forms as a result of the FR expansion. From an observational point of view, the compressed region in front of the MO part of (I)CMEs, which has both sheath and MO properties, has been studied in E. K. J. Kilpua et al. (2013) and in M. Temmer & V. Bothmer (2022). Interestingly, this is also manifested in our simulation setting. However, it is beyond the scope of this work to determine the origin of the misalignment between the sheath end time and MO onset time for some of the VS and to relate simulation results with observational features of this region. From now on, we will call

this region the MO front region for simplicity. For the purpose of this study, we first looked into the extended sheath signatures, where the duration of the sheath is given as $SH_{end}-SH_{start}$ (region in between the red vertical lines). We next analyze the clear sheath region with duration $MO_{start}-SH_{start}$ (region in between the first red and first green vertical lines). Finally, we analyze the MO front region with duration $MO_{start}-SH_{end}$ (between the first green vertical line and the second red vertical line).

We first analyze the evolution of the sheath, using different border selections, as explained in Section 3. The top panels of Figure 7 show the duration of the extended sheath in relation to the radial distance from the Sun for the spheromak with low inclination (left panel) and the spheromak with high inclination (right panel). The middle and bottom panels show the same but for a clear sheath and MO front region, respectively. Different colors represent different spacecraft, black for VS-E (middle, Earth-directed), red shades are the spacecraft on the crosses with respect to VS-E (namely, VS-a, VS-b, VS-c, and VS-d), and blue shades are the spacecraft on the diagonals of the spacecraft constellation (namely the VS-e, VS-f, VS-g, and VS-h). For both spheromaks, both clear and extended sheaths increase with increasing radial distance. The largely increasing extended sheath indicates that for most spacecraft, the MO start time is before the sheath end time (similar to what we see for VS-d in the right panels of Figure 2). This is confirmed by the bottom panels of Figure 7, where we see that the duration of the MO front region is negative (as per definition $MO_{start}-SH_{end}$, where $MO_{start} < SH_{end}$).

The extended sheath shows exponentially increasing profiles with distance for both spheromak inclinations which is consistent with earlier studies based on observations or simulations with other types of FR configurations, such as Gibson-Low (W. B. I. Manchester 2005; G. Siscoe & D. Odstreil 2008; M. Janvier et al. 2019). The study by C. Scolini et al. (2021) also confirms this exponentially increasing sheath in the simulation output based on EUHFORIA simulation with spheromak implementation as well as a recent comprehensive observational study by C. Larrodera & M. Temmer (2024). For the high-inclination spheromak (top-right panel), we can distinguish three different regimes, based on the rate of change of the sheath. The black curve (VS-E) is the slowest, i.e., the size of the sheath increases slowly in time in the Earth's direction compared to other directions. The rate of change in the four red curves (VS-a, VS-b, VS-c, and VS-d) and two blue-shaded curves (VS-f and VS-g) is faster compared to the black curve and increasingly faster for each curve (referred to hereafter as the middle-increase regime). Finally, the fastest rate of change is for the two curves in the light shades of blue (VS-e and VS-h; referred to hereafter as the high-increase regime). This is a direct consequence of the high-inclination spheromak northward tilting, i.e., the decrease in the θ angle shown in the uppermost panel of Figure 6. Due to this tilting, VS-e, and VS-h, which exhibit that the high-increase regime spends more time in the sheath than the other two spacecraft on the diagonal, VS-f and VS-g. This can also be seen in Figure 13 of Appendix B. The situation is slightly different for the low-inclination spheromak (top-left panel). Again, we see the slowest rate of change for the VS-E curve and the middle regime for VS on the crosses (VS-a, VS-b, VS-c, and VS-d). However, the situation is different for the VS on the diagonals of the spacecraft constellation. In this case, VS-h falls in the

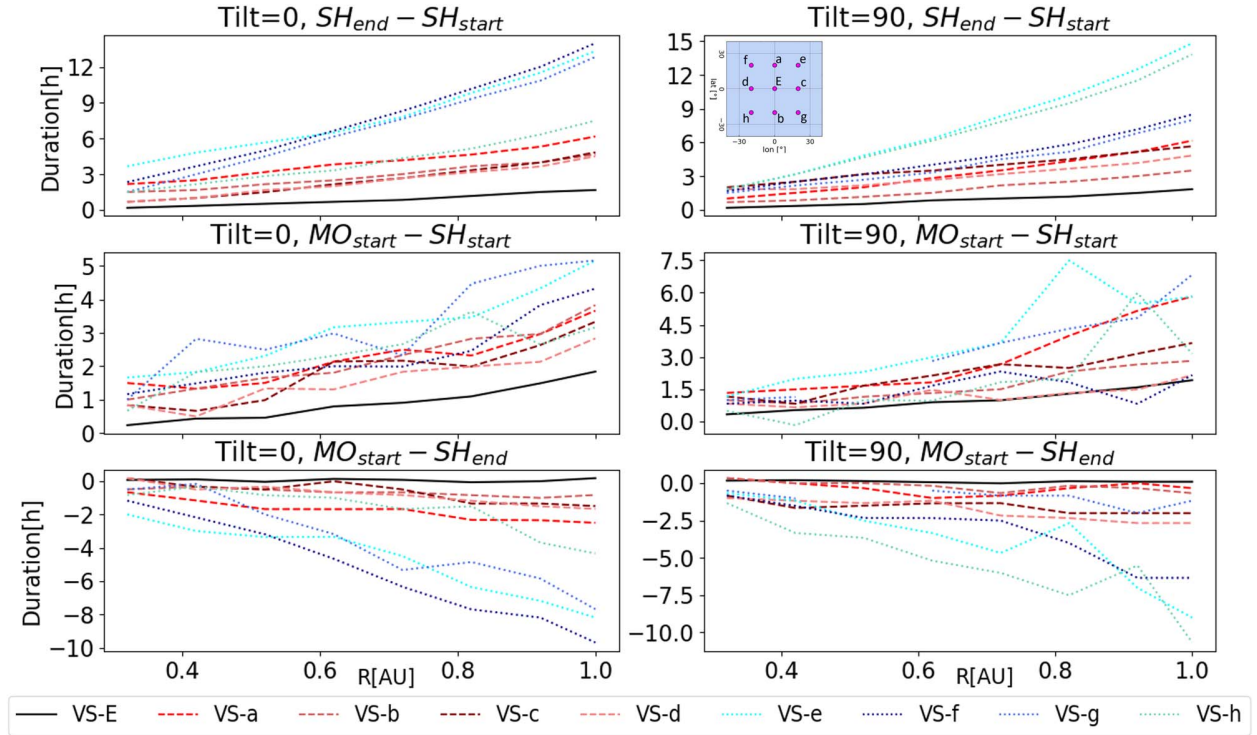


Figure 7. The top panels show the extended sheath duration with respect to radial distance for different VS, for both the high-inclination spheromak (right panels) and low-inclination spheromak (left panels). The middle and bottom panels show the same for the clear sheath and MO front region of the MO, respectively. Different colors correspond to different spacecraft: black for VS-E (middle, Earth-directed), red shades for spacecraft on the crosses with respect to VS-E (VS-a, VS-b, VS-c, and VS-d), and blue shades for spacecraft on the diagonals of the spacecraft constellation (VS-e, VS-f, VS-g, and VS-h). For details see the main text.

middle-increase regime, while the rest of the spacecraft on the diagonals (VS-e, VS-f, VS-g) are found in the high-increase regime. The slight difference in the behavior of the time evolution curves corresponding to the diagonals of the spacecraft constellation is related to the slight differences in the tilting and drift of the spheromak, which is slightly different for low- and high-inclined spheromaks, as well as the inclination itself. Better visualization of the extended sheath crossing for each VS for the low-inclination spheromak is shown in Figure 14 in Appendix B, while corresponding animations for all the other radial distances are included here: doi:10.6084/m9.figshare.25849135. Nevertheless, in general, for both inclinations, we observe that the rate of the change in the time evolution curve of the extended sheath is slowest at the apex and increases toward the flanks.

The clear sheath (middle panels of Figure 7), does not show the regular profile as is the case with the extended sheath in the upper panels. However, the increase in duration with radial distance is still visible. The irregularity of the profile may not be an inherent property of the clear sheath, but rather related to the methodology based on which it was estimated: (a) the end and the beginning of the observed interval are determined based on two different methods (the plasma β and the magnetic field vector method; see Section 3 for details) and (b) the time cadence with which the 3D simulation domain data are stored that can lead to an error of ± 30 minutes.

Finally, we analyze the time evolution of the MO front region, which is shown in the bottom panels of Figure 7. Considering that the duration is here negative (as per definition), we can again see a clear increase in duration with increasing distance from the Sun. Similar to the top panels, the slowest rate of increase is observed for VS-E (black curve), the

spacecraft on the cross of the constellation (red color tones) are found in the middle-increase regime, and the spacecraft on the diagonals (blue-colored tones) are found in the high-increase regime. The only difference between the low- and high-inclination spheromaks is seen in the duration of the frontal region for VS-g. The low-inclination spheromak shows a profile similar to other VS on the diagonals of the constellation, while the high-inclination spheromak shows a profile more similar to VS on the crosses of the constellation. This could be related to the slight differences in the tilting and drift of the spheromak for two different inclinations, as noted above for an extended sheath.

6.1.1. Plasma Nonradial Flows Inside the Sheath Region

We next analyze plasma nonradial flows (NRFs) in the extended sheath region, where we refrain our analysis to the extended sheath ($SH_{\text{end}} - SH_{\text{start}}$; see Section 3 for details).

Figure 8 shows the normal and tangential components, and the magnitude of the NRFs within the extended sheath region. Each subplot represents one VS and the subplots are aligned to mimic the position of the spacecraft on the grid (see Figure 1). For both high-inclination (blue color tones) and low-inclination (red color tones) spheromaks, we can see very similar profiles and values of the magnitude of NRFs inside the extended sheath region. This is not surprising considering that a spheromak, regardless of its inclination, is initially a spherical structure. It is important to note that as the simulation progresses they lose their spherical symmetry. More precisely, spheromaks have a perfect spherical structure when they are inserted in the simulation, but as they move through the inner boundary they interact with the ambient IMF and solar wind,

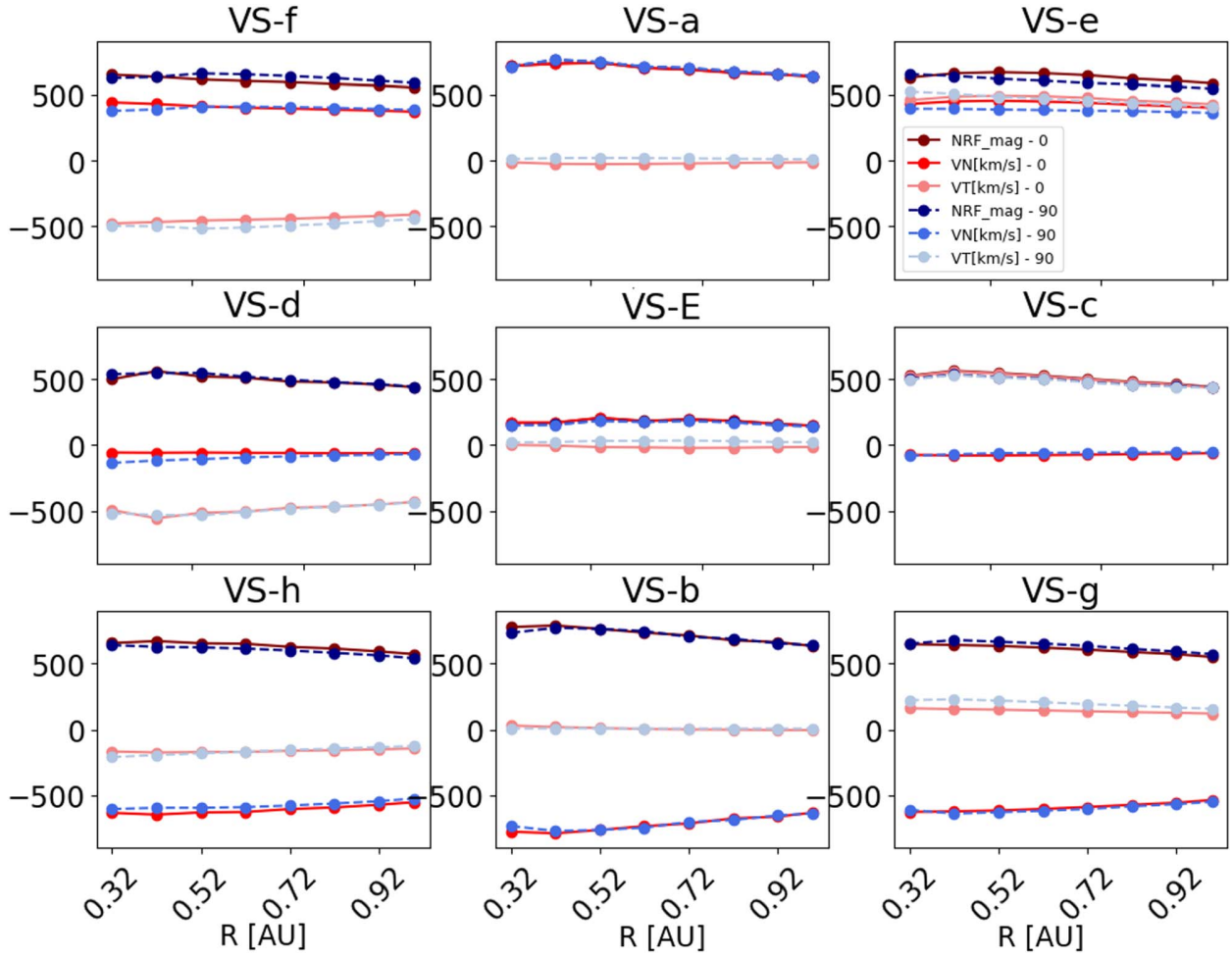


Figure 8. Mean values of the NRF magnitude, the tangential, and the normal component for both low- (red shading) and high- (blue shading) inclination spheromaks in the sheath region in relation to the radial distance.

and thus, they experience a certain amount of flattening in the plane perpendicular to the central axis. This can be seen in Figure 9, which shows the vector field as it is distributed inside the spheromak volume in the case of the low inclination 18.7 hr since insertion. The detection tool found a spheromak with an extent of 0.490 au in the east–west direction and 0.430 au in the north–south direction (see the minimum and maximum values for y' and z' at the bottom left of Figure 9). These orientations are in the reference frame of the spheromak, which is tilted with respect to the HEEQ coordinate frame as given by the angles on the bottom left of the figure. Due to this distortion of the spheromak shape, for the low-inclination spheromak, we have a greater extent in the ecliptic plane compared to the meridional plane, and vice versa for the high-inclination spheromak. However, based on the NRF behavior we observe in Figure 8, it would not seem that this distortion has a significant impact on the NRFs in the sheath region. In the case of the high-inclination spheromak, 18.7 hr since insertion, its extent in the east–west and the north–south directions in the spheromak reference frame was 0.500 au and 0.414 au, respectively.

The magnitude of the NRFs is the lowest for VS-E at $100\text{--}200\text{ km s}^{-1}$, which is to be expected as this is the direction of propagation of the two spheromaks, and the solar wind begins to diverge around the MO, while the nonradial flows appear to be more pronounced in the latitudinal and

longitudinal directions, away from the apex. Slightly higher values of NRF magnitudes than for VS-E, $400\text{--}600\text{ km s}^{-1}$, can be seen for the VS in the ecliptic plane (VS-d and VS-c), while the highest values, $500\text{--}800\text{ km s}^{-1}$ are seen for VS out of the ecliptic plane. This indicates that the pressure gradient developing in front of the (I)CME acts to slide IMF field lines away from the center of the (I)CME in the direction perpendicular to the ecliptic plane (see D. J. McComas et al. 1989).

For both high- and low-inclination spheromaks, we see a positive tangential component of velocity for the spacecraft on the right (VS-e, VS-c, and VS-g) and it is negative for the spacecraft on the left (VS-f, VS-d, and VS-h). Similarly, the normal component of the NRFs has positive values for spacecraft above the ecliptic (VS-f, VS-a, and VS-e) and negative for spacecraft below the ecliptic (VS-h, VS-b, and VS-g). As expected, this indicates that the plasma flows from the center of the spheromak toward the edges, bypassing the obstacle.

Some differences between the NRFs for different-inclination spheromaks can be observed. First, for VS-f and VS-g, we see a slightly higher tangential component of velocity for high-inclination spheromaks (light blue) than for low-inclination spheromaks (light red). This is consistent with the assumption presented in K. Martinić et al. (2022) and K. Martinić et al. (2023) that the ambient plasma bypasses the obstacle in the

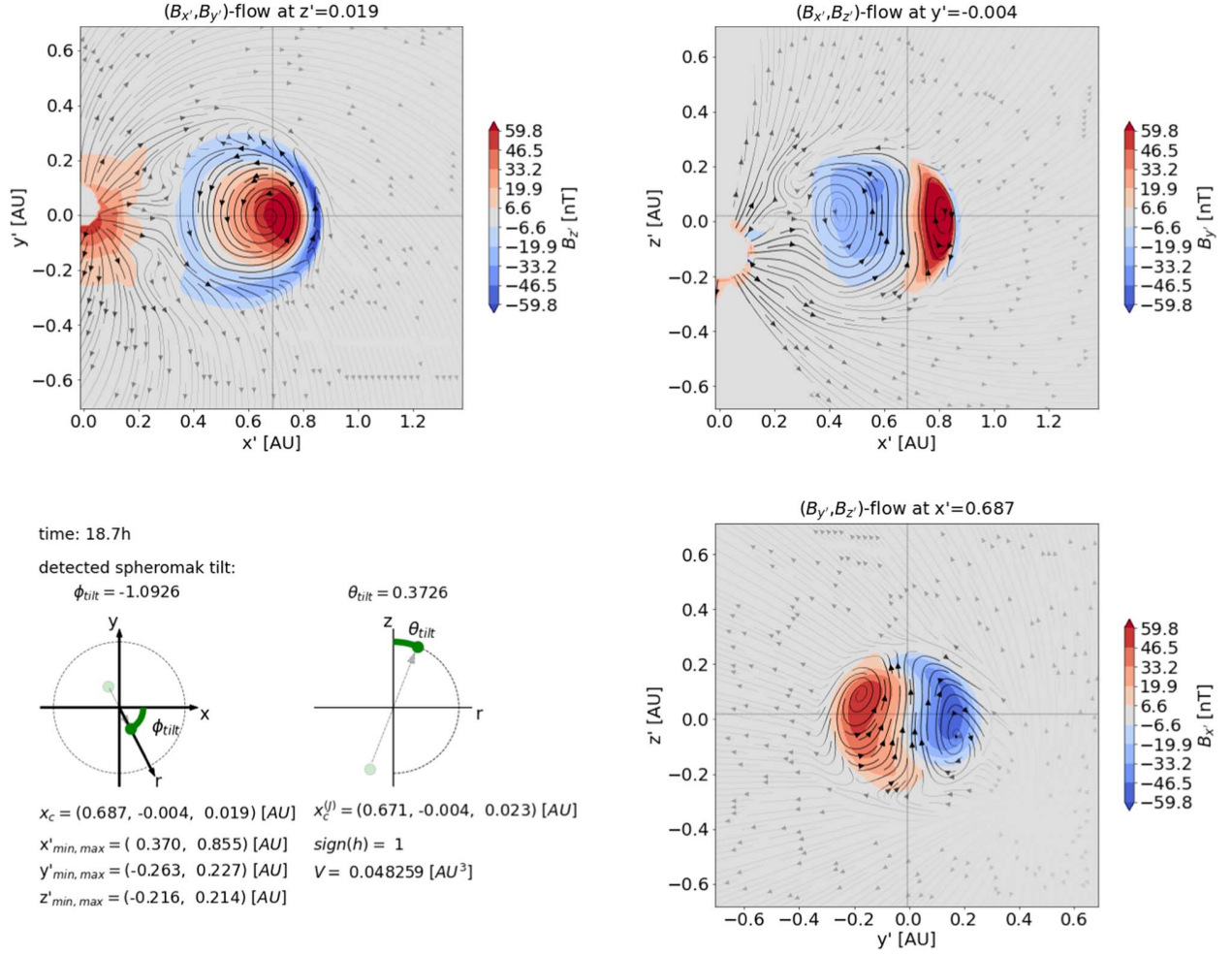


Figure 9. Vector field as distributed inside the spheromak volume in the case of the low-inclination spheromak shown in the spheromak’s reference frame (x' , y' , z') for three perpendicular planes.

direction in which the extent of the obstacle is smaller. A spheromak with a high inclination has a slightly smaller extension of the front in the tangential direction than a spheromak with a low inclination, so the tangential component of the NRF is more pronounced in spheromaks with a high inclination. This can also be seen in the right-hand panels of Figure 10. Figure 10 shows the tangential component of the velocity over all heliospheric distances probed in the simulation for both high- (light blue) and low-inclination (light red) spheromaks. The right panels refer to VS-f and VS-g, while the left panels refer to spacecraft VS-a and VS-E. We also see a difference in the direction of the tangential NRF component in the sheath for low- and high-inclination spheromaks for VS-E and VS-a. The tangential component of the velocity in the sheath has positive values for high-inclination spheromaks and negative values for low-inclination spheromaks (see Figure 8 center panels and Figure 10 left panels). Figure 10 shows that the differences in the tangential component of the NRFs for low- and high-inclination spheromaks are not due to random fluctuations, e.g., due to turbulence or small-scale wave activity, as often seen in in situ profiles of real (I)CMEs, but rather a consistent difference seen in the simulation in situ profiles for all heliospheric distances. This difference between the tangential component of NRFs inside the extended sheath

region seen in in situ profiles for VS-E across all radial distances is due to the different drifting (east–west) direction of different-inclination spheromak as shown in Figure 5, fourth panel.

The profiles shown in Figure 8 for the NRF magnitude, the tangential, and the normal components show similar behavior, where dominant is the slight decrease with increasing radial distance from the Sun. But we can also see for some VS (for VS on the crosses of the constellation—VS-a, VS-c, VS-b, and VS-d) an NRF maximum is reached somewhere around 0.4 au, after which a slow decline can be observed. This could be because the rate of growth of the sheath region is higher below 0.4 au compared to greater distances from the Sun. This is an interesting aspect of the simulation output, but it falls outside the scope of this paper. However, we consider investigating it further in a follow-up study.

6.2. The Drag Parameter

Finally, we analyze the drag parameter γ for two different inclinations. We remind the reader that apart from different inclinations, both spheromaks were inserted with identical properties in the same SW and IMF environment.

The bottom-right panel of Figure 11 shows the drag parameter γ as a function of the radial distance for both

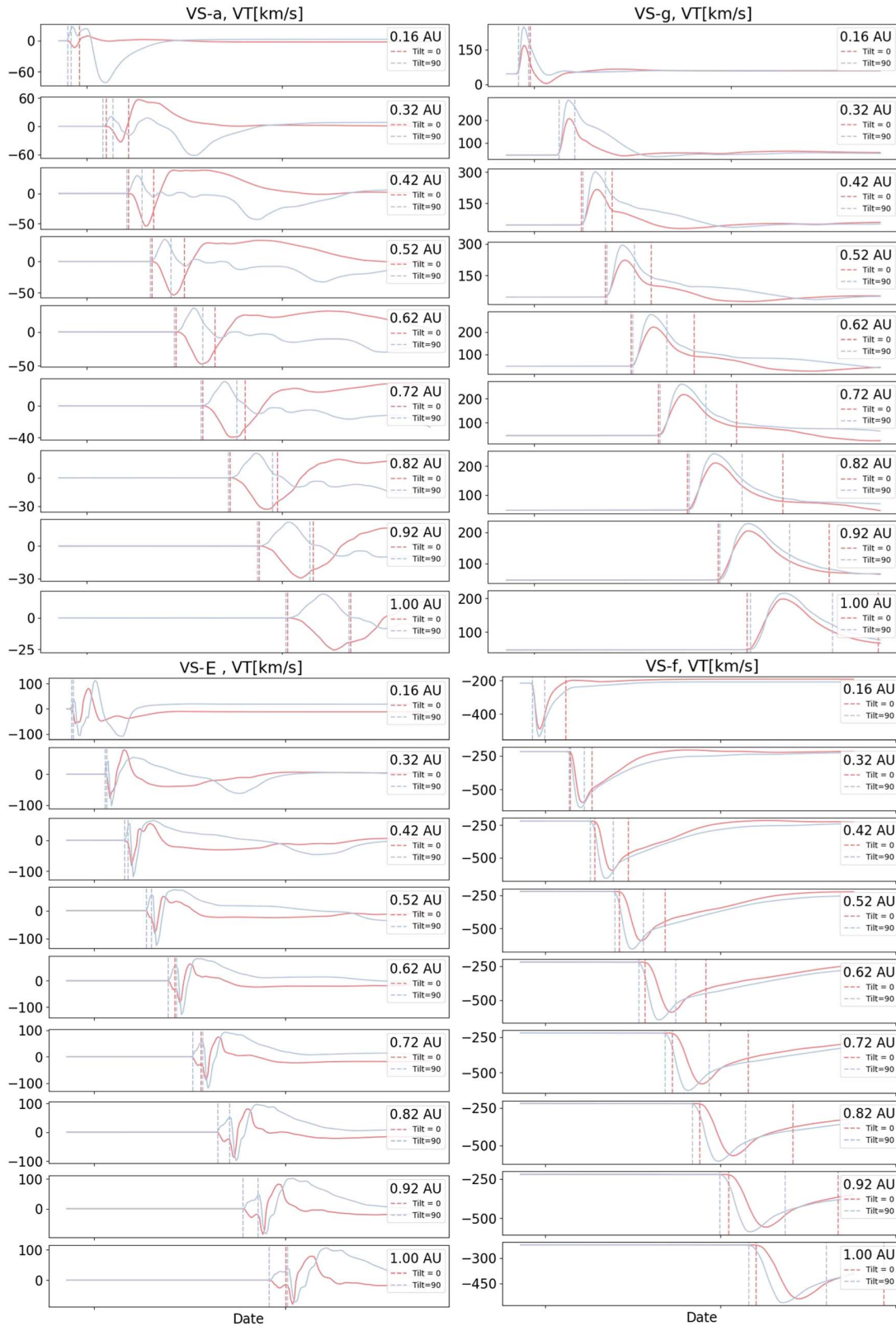


Figure 10. Tangential component of the velocity as seen in situ for SV-a, SV-f, SV-E, and SV-g, from left to right and from top to bottom. The light red lines refer to the low-inclination spheromak and the light blue lines are related to the high-inclination one. Similarly, dashed red vertical lines mark the sheath of the low-inclination spheromak, and a pair of light blue vertical lines mark the sheath of the high-inclination spheromak.

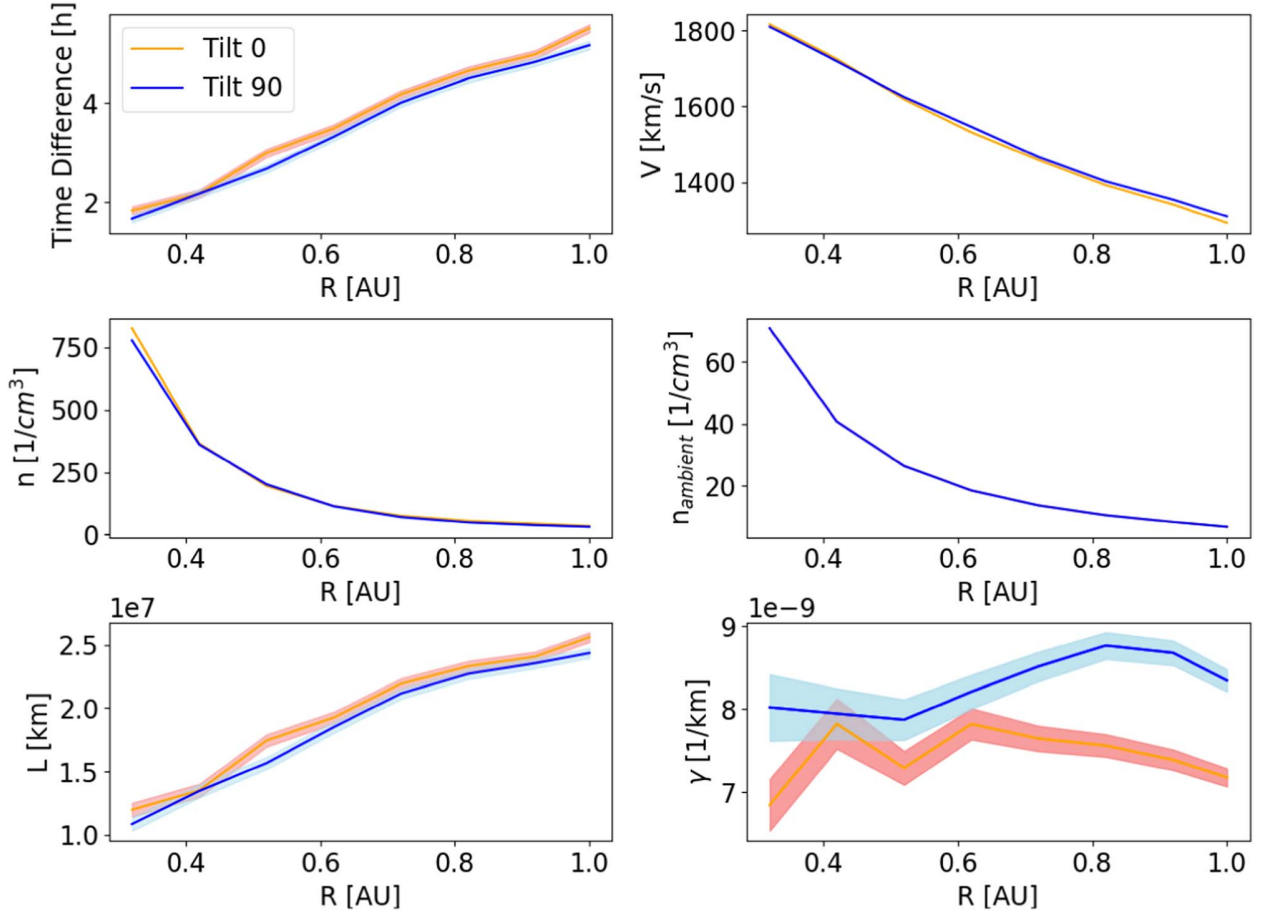


Figure 11. MO duration in seconds based on B_{vec} (corresponding to the green boundaries in Figure 2), mean velocity, and median density inside the respective MO, mean ambient density, radial cross section of the respective MO, and drag parameter γ , respectively, from left to right and from top to bottom. Variables are given with respect to the radial distance and separately for the low-inclination spheromak (orange) and the high-inclination spheromak (blue).

low- (orange) and high- (blue) inclination spheromaks. The other panels of the figure show variables needed to obtain the drag parameter γ , based on Equation (2) from Section 5. From top to bottom and from left to right, Figure 11 shows, (1) the duration of the MO part of the spheromak determined based on the B_{vec} (see green vertical lines shown in Figure 2, left panels), (2) mean velocity and (3) median density inside the respective MO, (4) the mean ambient density, and (5) the obtained radial cross section of the MO part. The shaded area shown for the time difference between the MO boundaries (top-left panel) takes the ± 5 minute uncertainty in the derivation of the MO boundaries into account. This uncertainty is also the source of the uncertainties in the calculated values for the radial cross section L and drag parameter γ . We note here that for this portion of the study, we used a higher time cadence for the 3D simulation domain output than what was used for the previous sections. We can see a slight difference between the values of the drag parameter γ for low- and high-inclination spheromaks in the simulation. The high-inclination spheromak has somewhat higher values of the γ parameter, meaning that the high-inclination spheromak experienced greater drag force in the simulation. We note that this difference is directly related to the difference in the radial cross section of the MO part (bottom-left panel).

From the simulation, it appears that there is a slight difference in the MO duration for low- and high-inclination

spheromaks (see the top-left panel of Figure 11). The greater the MO duration, the greater the radial cross section, and then consequently smaller γ is obtained. The differences in the mean velocity and median density inside the spheromak MO part (top-right panel and middle-left panel in Figure 11, respectively), as well as the differences in the ambient density (middle-right panel in Figure 11), are negligible. It is important to note here that the C_d , dimensionless drag coefficient is taken to be constant and equal to one when calculating the drag parameter γ and thus we cannot expect the drag parameter γ results shown in the bottom-right panel of Figure 11 to outline the difference in the draping pattern between the two spheromaks in the simulation. The draping pattern is a crucial factor governing the proposed hypothesis in K. Martinić et al. (2022) and K. Martinić et al. (2023) that the high-inclination spheromak should experience greater drag due to less efficient sliding of the IMF field lines in the direction perpendicular to the motion of the (ICME (i.e., slipping of the transversal IMF component perpendicular to the direction of (ICMEs motion; see also J. T. Gosling & D. J. McComas 1987)). From Figure 11 we can also see that the drag parameter γ is not constant with respect to the radial distance. Except for radial cross section L , drag parameter γ also depends on the ratio between the density inside the MO and ambient density, from the middle panels we can see that the decrease in the ambient density shows a slightly different profile than the decrease in the spheromak

density meaning its ratio changes with radial distance. This result challenges the constant γ assumption which is often used in drag-based models in operational mode. Furthermore, the obtained drag parameter γ shows a rather low value when compared to for example with results presented in B. Vršnak et al. (2013), where γ is in the range $0-2 \cdot 10^{-7}$. We believe this discrepancy stems from a rather high spheromak density used in our simulation (for a range of densities see also M. Temmer et al. 2021) that increases the density ratio in Equation (2) in Section 5 and consequently smaller gamma values are obtained.

When we performed the same analysis of the drag parameter γ , using Equation (2) from Section 5, but with a numerical setup with a different resolution— ± 30 minutes, we found that the drag parameter γ is slightly higher for the low-inclination spheromak than for the high-inclination spheromak (opposite to what is shown in the bottom-right panel of Figure 11). We also cross-checked the results shown in Figure 11 for the drag parameter γ using Equation (1) from Section 5, and we obtained a drag parameter γ of the same order of magnitude and with a similar profile with respect to the radial distance but slightly higher for the low-inclination spheromak than for the high-inclination spheromak. Thus, we conclude that different methods and time resolutions showed that the inclination dependency of drag parameter γ cannot be resolved for the given setup.

7. Conclusions

We have investigated the influences of the (I)CME inclination on its propagation in the heliosphere by performing simulations with the EUROpean Heliospheric FORecasting Information Asset (EUHFORIA) 3D MHD model (J. Pomoell & S. Poedts 2018). The study focuses on two (I)CMEs implemented as spheromaks (C. Verbeke et al. 2019) with almost identical properties, differing only in their inclination. We also inserted 81 virtual spacecraft into the simulation domain to investigate the radial, longitudinal, and latitudinal differences. One spheromak is embedded as a low-inclination spheromak (Tilt = 0°) with its axis of symmetry perpendicular to the ecliptic and its central axis (toroidal axis of the FR) laying in the ecliptic. The other spheromak is embedded as a high-inclination spheromak (Tilt = 90°), whose axis of symmetry lies in the ecliptic and whose corresponding FR axis is perpendicular to the ecliptic plane. To avoid the CME interaction with heliospheric current sheath and to maximize the inclination effect on the propagation, we have chosen simplified conditions for the solar wind and the IMF. The IMF has a uniform and outwardly directed (positive) radial configuration, $B_r = 100$ nT at the inner boundary with a radial velocity component of the surrounding solar wind of $V_r = 400.0$ km s $^{-1}$. Inserted spheromaks were chosen with a high density ($\rho = 0.5 \cdot 10^{-17}$ kg m $^{-3}$) and a high velocity ($v = 1500.0$ km s $^{-1}$) in order to minimize the spheromak tilting due to torque (E. Asvestari et al. 2022). Regardless of the fact that we carefully chose the ambient and spheromak conditions, we found that a torque is exerted on the spheromak affecting the orientation and thus, the simulation results should be interpreted accordingly. Furthermore, we derived the boundaries of the spheromak sheath and the magnetic obstacle by using both the in situ simulation profiles at each VS and determining the plasma β boundary as well as the magnetic flux density as a vector field and the magnitude of the plasma

pressure gradient derived from the 3D simulation output. We found that the boundaries derived in these two discrete ways are very different.

We found that the duration of the sheath increases exponentially with increasing radial distance, similar to Gibson-Low FR, which is essentially a modified spheromak (W. B. I. Manchester 2005; G. Siscoe & D. Odstrcil 2008; M. Janvier et al. 2019). We also found that the duration of the sheath increases toward the flanks of the spheromak, confirming the growth of the sheath as moving away from the (I)CME apex. Similarly, the nonradial flows are smallest near the apex of the (I)CME and increase toward the flanks. However, we found a difference in the magnitude of the nonradial flows in the ecliptic and out of the ecliptic plane. Nonradial flows out of the ecliptic are stronger than in the ecliptic plane for both high- and low-inclination spheromaks. This confirms the assumption of K. Martinić et al. (2022) and K. Martinić et al. (2023), following the discussion in J. T. Gosling & D. J. McComas (1987), that the transverse IMF magnetic field component “slips” in the direction perpendicular to the (I)CME motion due to the pressure gradient that accumulates in front of the (I)CME during its propagation. We also derived that the drag parameter γ , a crucial factor in the study of the drag force acting on the (I)CME, changes slightly with radial distance in the order of 10^{-9} . We highlighted that such a rather small value of the drag parameter γ is a consequence of having inserted very dense spheromaks.

When cross-checking our results for drag parameter γ with the same method, but different resolution, as well as when cross-checking our results with a different method based on Equation (1) from Section 5 we found that inclination dependency of the drag parameter γ cannot be resolved with our numerical setup. We also note that the drag parameter γ determined in this study assumes that the dimensionless drag coefficient C_d is constant and equal to one, so our drag parameter γ cannot reflect the difference in the draping pattern between the two spheromaks investigated.

Besides the tilting due to torque and drift of the spheromak (E. Asvestari et al. 2022), the differences between the two differently inclined spheromaks could be masked by the predominantly spherical geometry of the spheromak, which leaves room for progress for future study in which we plan to use different FR models in the simulation, such as the FR3D model by A. Isavnin (2016) among others. In addition, this study showed the potential of MHD simulation studies in linking nonradial flows to the change in the orientation of the surrounding magnetic field (i.e., in revealing the draping pattern), which should also be reflected in the magnetohydrodynamic drag force acting on the CME as it propagates in the surrounding magnetic field and solar wind. In the future, we also hope to explore in more depth the sheath growth rate and the MO front exhibiting both, sheath and MO properties. These topics have been discussed only briefly in this work to keep the manuscript short and with a clear focus.

Acknowledgments

We gratefully acknowledge the support from the Austrian-Croatian Bilateral Scientific Projects “Multi-Wavelength Analysis of Solar Rotation Profile” and “Analysis of solar eruptive phenomena from cradle to grave.” M.D. and K.M. acknowledge support from the Croatian Science Foundation under project IP-2020-02-9893 (ICOHOSS). K.M. acknowledges

support from the Croatian Science Foundation in the scope of Young Researches Career Development Project Training New Doctoral Students. E.A. acknowledges support from the Academy of Finland/Research Council of Finland (Academy Research Fellow grant No. 355659). T.R. is supported by the Swiss National Science Foundation (SNSF) through the grant No. 210064.

Appendix A

Determination of the Spheromak Boundary Using the In Situ Profiles

In Section 3, it was already mentioned that the first red vertical line is derived as a 50% increase in β compared to the mean of the first 35 values when iterating from the beginning of the time series. The second red vertical line is derived as a 50% increase compared to the last 35 values of the time series when

iterating from the end to the beginning of the time series. Here we show four exceptions to this method. The second vertical line was derived manually for spheromaks with a low inclination for VS-c and VS-g and spheromaks with a high inclination for VS-a and VS-e. The boundaries for these VS can be seen in Figure 12. In Figure 12, one can see that the β profiles exhibit a numerical artifact, namely, an increase in the β parameter directly after the MO. Due to this artifact, it was not possible to derive the sheath end boundary using the method described in Section 3. At this point, we would also like to point out that MO, defined as the part of the in situ profile where plasma β falls below one, is also not visible for all VS and all radial distances. For example, for spheromaks with low inclination, for VS-e (see Figure 12 bottom-left panels), there is no plasma β value less than one for all distances except 0.16 au, i.e., there is no MO according to the chosen criterion.

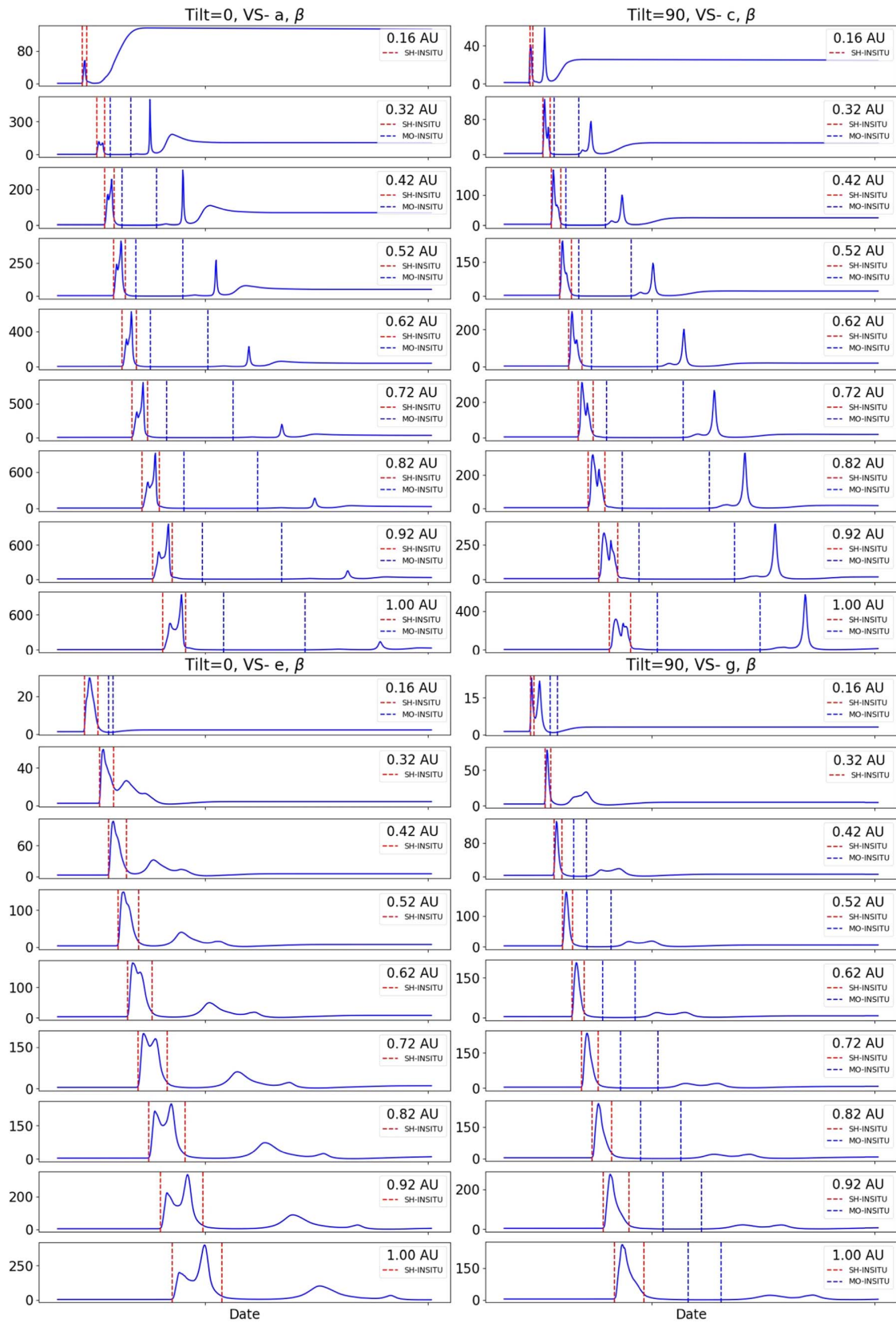


Figure 12. Plasma β parameter for VS-a and VS-e for the low-inclination spheromak and for VS-c and VS-g for the high-inclination spheromak. Red vertical lines mark the extended sheath derived solely based on the plasma β parameter increase/decrease, while blue vertical lines mark the MO part of the spheromak where the plasma β parameter is less than one.

Appendix B Plasma Beta Parameter Spacecraft Crossing

Figure 13 (for the high-inclination spheromak) and Figure 14 (for the low-inclination spheromak) show the plasma β parameter, normalized by $1/r^2$, where r is in astronomical units, in equatorial and in three meridional planes corresponding to -20° , 0° , and 20° in longitude, respectively, from left to right. Red arrows indicate the spacecraft crossing. Figure 13 shows the spacecraft crossing of VS-f and VS-h in the meridional plane corresponding to -20° longitude and we can see that VS-h will spend more time in the clear sheath region (region of increased plasma β parameter) than VS-f.

Similarly, VS-e will spend more time in the extended sheath region than VS-g as seen in the meridional plane corresponding to 20° longitude. This confirms the results for the extended sheath duration for the high-inclination spheromak where we derived the highest increase regime for VS-h and VS-e, while VS-f and VS-g showed an intermediate-increase regime (see top-right panel of Figure 7). Analogously, in Figure 14 we can see that VS-h will spend less time in the extended sheath region than VS-f, which is why for VS-h we found an intermediate-increase regime of the extended sheath, unlike for the rest of the spacecraft on the diagonal (see the top-left panel of Figure 7).

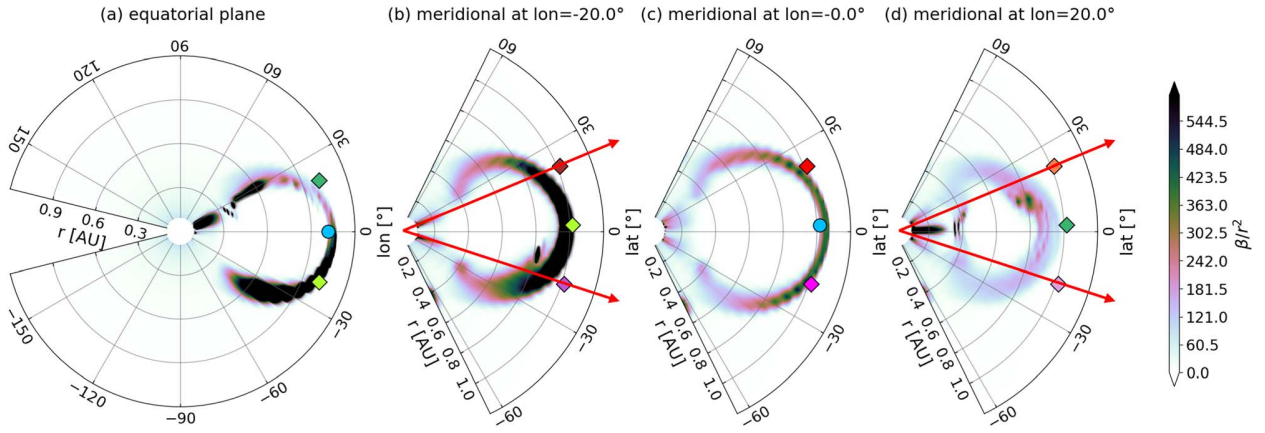


Figure 13. Plasma β parameter, normalized by $1/r^2$, where r is in astronomical units, of the simulated high-inclination spheromak at the equatorial and meridional planes.

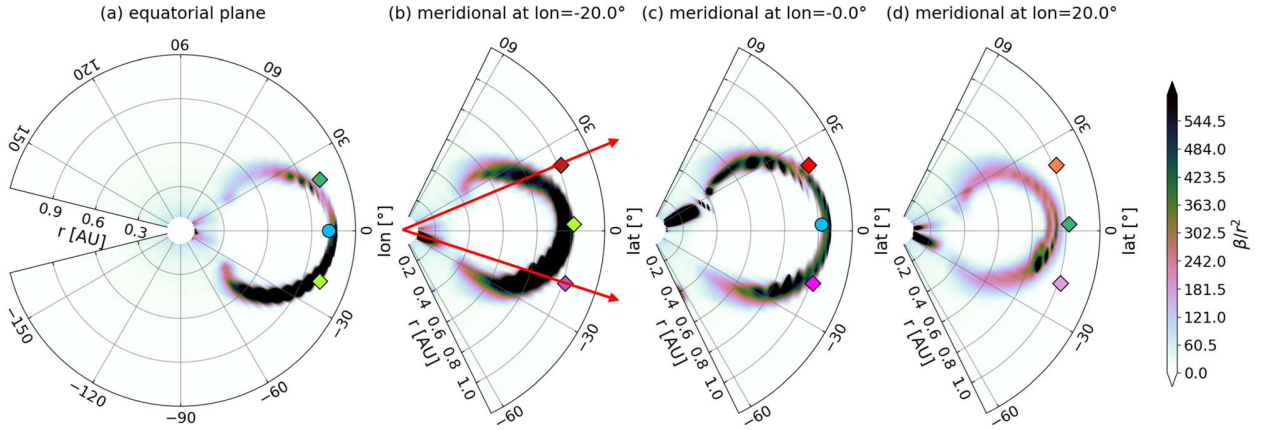


Figure 14. Plasma β parameter, normalized by $1/r^2$, where r is in astronomical units, of the simulated low-inclination spheromak at the equatorial and meridional planes.

ORCID iDs

Karmen Martinić  <https://orcid.org/0000-0002-9866-0458>
 Eleanna Asvestari  <https://orcid.org/0000-0002-6998-7224>
 Mateja Dumbović  <https://orcid.org/0000-0002-8680-8267>
 Tobias Rindlisbacher  <https://orcid.org/0000-0003-2617-4319>
 Manuela Temmer  <https://orcid.org/0000-0003-4867-7558>
 Bojan Vršnak  <https://orcid.org/0000-0002-0248-4681>

References

- Asvestari, E., Rindlisbacher, T., Pomoell, J., & Kilpua, E. K. J. 2022, *ApJ*, **926**, 87
- Burlaga, L., Sittler, E., Mariani, F., & Schwenn, R. 1981, *JGR*, **86**, 6673
- Cargill, P. J. 2004, *SoPh*, **221**, 135
- Dasso, S., Mandrini, C. H., Démoulin, P., & Luoni, M. L. 2006, *A&A*, **455**, 349
- Dumbović, M., Devos, A., Vršnak, B., et al. 2015, *SoPh*, **290**, 579
- Gosling, J. T., Bame, S. J., McComas, D. J., & Phillips, J. L. 1990, *GeoRL*, **17**, 901
- Gosling, J. T., & McComas, D. J. 1987, *GeoRL*, **14**, 355
- Gosling, J. T., Thomsen, M. F., Bame, S. J., & Zwickl, R. D. 1987, *JGR*, **92**, 12399
- Hess, P., & Zhang, J. 2015, *ApJ*, **812**, 144
- Huttunen, K. E. J., & Koskinen, H. E. J. 2004, *AnGeo*, **22**, 1729
- Huttunen, K. E. J., Koskinen, H. E. J., & Schwenn, R. 2002, *JGRA*, **107**, 1121
- Isavnin, A. 2016, *ApJ*, **833**, 267
- Janvier, M., Winslow, R. M., Good, S., et al. 2019, *JGRA*, **124**, 812
- Kay, C., Opher, M., & Evans, R. M. 2013, *ApJ*, **775**, 5
- Kay, C., Opher, M., & Evans, R. M. 2015, *ApJ*, **805**, 168
- Kilpua, E., Koskinen, H. E. J., & Pulkkinen, T. I. 2017, *LRSP*, **14**, 5
- Kilpua, E. K. J., Isavnin, A., Vourlidas, A., Koskinen, H. E. J., & Rodriguez, L. 2013, *AnGeo*, **31**, 1251
- Koskinen, H. E. J., & Huttunen, K. E. J. 2006, *SSRv*, **124**, 169
- Larrodera, C., & Temmer, M. 2024, *A&A*, **685**, A89
- Lepping, R. P., Jones, J. A., & Burlaga, L. F. 1990, *JGR*, **95**, 11957
- Lundquist, S. 1950, *Ark. Fys*, **2**, 35
- Manchester, W. B. I., Gombosi, T. I., De Zeeuw, D. L., et al. 2005, *ApJ*, **622**, 1225
- Martinić, K., Dumbović, M., Temmer, M., Veronig, A., & Vršnak, B. 2022, *A&A*, **661**, A155
- Martinić, K., Dumbović, M., Čalogović, J., et al. 2023, *A&A*, **679**, A97
- McComas, D. J., Gosling, J. T., Bame, S. J., Smith, E. J., & Cane, H. V. 1989, *JGR*, **94**, 1465
- Mostl, C., Rollett, T., Frahm, R. A., et al. 2015, *NatCo*, **6**, 7135
- Pal, S., Kilpua, E., Good, S., Pomoell, J., & Price, D. J. 2021, *A&A*, **650**, A176
- Pomoell, J., & Poedts, S. 2018, *JSWSC*, **8**, A35
- Ruffenach, A., Lavraud, B., Farrugia, C. J., et al. 2015, *JGRA*, **120**, 43
- Sarkar, R., Pomoell, J., Kilpua, E., et al. 2024, *ApJS*, **270**, 18
- Scolini, C., Dasso, S., Rodríguez, L., Zhukov, A. N., & Poedts, S. 2021, *A&A*, **649**, A69
- Siscoe, G., MacNeice, P. J., & Odstrcil, D. 2007, *SpWea*, **5**, S04002
- Siscoe, G., & Odstrcil, D. 2008, *JGRA*, **113**, A00B07
- Smith, E. J. 2001, *JGR*, **106**, 15819
- Temmer, M., & Bothmer, V. 2022, *A&A*, **665**, A70
- Temmer, M., Holzkecht, L., Dumbović, M., et al. 2021, *JGRA*, **126**, e28380
- Temmer, M., Scolini, C., Richardson, I. G., et al. 2023, arXiv:2308.04851
- Tsurutani, B. T., Gonzalez, W. D., Tang, F., Akasofu, S. I., & Smith, E. J. 1988, *JGR*, **93**, 8519
- Vandas, M., Fischer, S., Dryer, M., Smith, Z., & Detman, T. 1995, *JGR*, **100**, 12285
- Vandas, M., Fischer, S., Dryer, M., Smith, Z., & Detman, T. 1996, *JGR*, **101**, 2505
- Verbeke, C., Pomoell, J., & Poedts, S. 2019, *A&A*, **627**, A111
- Vourlidas, A., Lynch, B. J., Howard, R. A., & Li, Y. 2013, *SoPh*, **284**, 179
- Vršnak, B., Žic, T., Lulić, S., Temmer, M., & Veronig, A. M. 2016, *SoPh*, **291**, 89
- Vršnak, B., Žic, T., Vrbanec, D., et al. 2013, *SoPh*, **285**, 295
- Wang, J., Liu, S., & Luo, B. 2023, *AdSpR*, **72**, 5263
- Wu, S. T., Dryer, M., & Han, S. M. 1983, *SoPh*, **84**, 395
- Wu, S. T., Han, S. M., & Dryer, M. 1979, *P&SS*, **27**, 255
- Yurchyshyn, V. 2008, AGU Fall Meeting Abstracts, 2008, SH13B-1551
- Yurchyshyn, V., Abramenko, V., & Tripathi, D. 2009, *ApJ*, **705**, 426
- Zhang, J., Dere, K. P., Howard, R. A., & Bothmer, V. 2003, *ApJ*, **582**, 520

Chapter 3

Unified discussion

Due to a generally anisotropic heliosphere, differently oriented CMEs may interact differently with the ambient plasma and IMF, even when the initial eruption conditions are similar. For this, we examined the possible link between the orientation of a CME and its propagation in the heliosphere. The theme is covered within three published papers: Martinić et al. (2022), Martinić et al. (2023), and Martinić et al. (2024). The first two are observational studies where CMEs were probed remotely and in-situ using data from STEREO (Howe, 2009), SOHO (Brueckner et al., 1995), and SDO (Pesnell et al., 2012) missions. The third paper is a modeling study where inclination effects were probed in the EUHFORIA simulation (Pomoell & Poedts, 2018) with CMEs represented as spheromaks (Verbeke et al., 2019).

In Martinić et al. (2022) we analyzed 22 well-associated CME-ICME pairs in the rising and maximum phase of solar cycle 24. We found that GCS (Thernisien et al., 2006) and ellipse fit (Chen et al., 1997) are only robust to determine whether FR orientation is predominately low (in the ecliptic plane) or high (in the meridional plane) and we found that these two methods perform equally good for deriving the dominant inclination in the near Sun environment. Regarding obtaining the inclination from in-situ measurements (near Earth environment) we performed an approximative method where CME orientation can be derived from the rotation of the magnetic field components and each CME can be associated with one of eight FR types, four of which are low inclined and four high inclined (see Figure 1 in Palmerio et al., 2018). As shown in Al-Haddad et al. (2013), more sophisticated in-situ FR fitting techniques provide significantly different results for inclination and are highly dependent on the determination of FR boundaries (which is a subjective procedure on its own). Uncertainties in inclination determination were also highlighted in Verbeke et al. (2023) and Kay & Palmerio (2024) where they showed that inclination (tilt angle in GCS) is the parameter with the greatest uncertainty of all. Interestingly, the CMEs' inclination is the most important for accurate space weather

prediction because it greatly conditions the CMEs' geoeffectiveness (see also discussion in Kay & Palmerio, 2024). The analysis of non-radial flows (NRFs) in the sheath region of studied 22 CME-ICME events indicates that high-inclination events show a slightly higher ratio of the velocity in the y- and z-direction of the GSE coordinate system. This result is confirmed in the Martinić et al. (2023) where 31 CME-ICME associations were studied in the greater period containing additional CMEs from solar cycle 23. We attribute different NRFs in the sheath region of the two groups of differently inclined CMEs in the manner that ambient plasma accumulates in front of the CME's FR (the driver) and bypasses it in the direction where the extent of the FR is smaller. For low inclination events, this is the CME's extent in the meridional plane (\pm z-direction of GSE) and for high inclination, this is the CME's extent in the ecliptic plane (\pm y-direction of GSE).

In Martinić et al. (2023) we additionally probed the drag parameter γ for the two groups of high and low inclination events. Under the a frozen-in condition of the IMF, different NRFs should reflect different IMF draping patterns. Consequently, this could be reflected in the difference in the overall drag experienced by the CMEs during its propagation in the heliosphere, i.e. in the drag parameter γ . However, there is no evidence of a statistically significant difference in drag parameter γ for the two groups of events with different dominant inclinations in Martinić et al. (2023). We note that the drag (as given by Equation (1) and (2) in section 1.2.3) primarily depends on the difference between the CME propagation velocity and the velocity of the ambient solar wind as well as on the cross-section of the CME, its' mass, and the density of the solar wind. It is thus possible that the inclination effect is "masked" by all those contributions. Moreover, the event sample in Martinić et al. (2023) mostly contains CMEs that occurred during the solar maximum which is when the IMF has the most complex configuration that significantly deviates from the idealized configuration shown in Figure 1.8. In the solar maximum quadrupolar and higher order moments of the coronal magnetic field become more significant (Hoeksema et al., 1982; Wang et al., 2000) and thus global draping pattern significantly deviates from the one presented in Section 1.3, reducing the chances for the revelation of systematic drag parameter γ difference for the two studied groups of events.

In order to avoid complex ambient conditions present in observational studies we performed a complementary simulation study with the simplest possible ambient configuration. In Martinić et al. (2024) we performed two EUHFORIA MHD simulations (Pomoell & Poedts, 2018) where CME was represented by spheromak (Verbeke et al., 2019). One simulation accounts for low inclination spheromak (toroidal spheromak axis in the ecliptic plane), and in another simulation, we inserted a spheromak with high inclination (toroidal spheromak axis in the meridional plane). Ambient conditions were chosen to minimize the spheromak tilting and drifting (Asves-

tari et al., 2022) so that the difference in the inclination between the two spheromak remains maximum as they are propagated in the heliospheric domain of the model. Another important feature we avoided in the simulations is the HCS. It is well known that CMEs interact with HCS (Yurchyshyn et al., 2009; Kay et al., 2015; Pal et al., 2021; Wang et al., 2023). This is why simulations with unidirectional IMF topology were performed. Boundaries of the shock-sheath and MO part of the spheromaks were derived in two different ways: based on the plasma β in-situ profiles and from the magnetic flux density and plasma pressure gradient derived from the 3D simulation output. Boundaries derived in these two ways indicate the existence of a so-called front region, where we observe the start of the MO indicated by magnetic field configuration, but plasma parameters still appear high, meaning, this region exhibits both MO and sheath properties. Interestingly, some portion of CMEs show front region properties observed in-situ, however, its origin is still debatable (Kilpua et al., 2013 and Temmer & Bothmer, 2022). Another interesting aspect of the simulation output is the observed sheath increase in duration with radial distance as well as an increase in duration with moving away from the CME's apex. The former was also shown in Scolini et al. (2021), where they calculated an exponential increase of the sheath with radial distance in spheromak EUHFORIA simulation of a case study halo CME. The latter might be just related to the way virtual spacecraft (VS) in the larger latitudinal/longitudinal distances cross the spheromak, but it can also be related to the intrinsic sheath creation mechanism which is still under discussion (see Larrodera & Temmer, 2024 and reference therein). Studied NRFs inside the sheath region show greater values for VS that are outside of the ecliptic plane which can be explained by the "slipping" of the transverse IMF component in the direction perpendicular to the CMEs motion due to the pressure gradient that develops in front of the CME as it propagates in the heliosphere as suggested by Gosling & McComas (1987). This simulation result is in agreement with the proposed draping of the transverse IMF mechanism (Martinić et al., 2022, Martinić et al., 2023). We also calculated the drag parameter γ for differently inclined spheromak CMEs from the simulation results. However, we found this calculation to be very sensitive to the resolution of the simulation output, and thus no conclusions were drawn. The lack of differences in simulation for differently inclined spheromaks might be related to the fact that spheromaks inserted in the simulation have spherical structures. Although they lose this ideal spherical structure as they propagate (they become flatter in the plane perpendicular to the central axis of the spheromak), this does not seem to be sufficient for systematic differences to appear. Further studies on the relationship between the behavior of NRFs and IMF draping as well as magnetic pressure and plasma pressure at different latitude/longitude distances from the CME apex are needed to better understand the global draping pattern. In addition, full Sun-to-Earth MHD simulations (e.g. Török et al., 2018) with a CME

implemented in the simulation as an FR structure, such as Isavnin (2016) with different extent of the front in the ecliptic and meridional planes for differently inclined CMEs are required to better investigate the effects of inclination on propagation.

Chapter 4

Conclusions

In this work, we have analysed the effects of the inclination of CMEs on their propagation in the heliosphere. The work consists of three peer-reviewed papers. In Martinić et al. (2022) and Martinić et al. (2023) we have compiled a list of real CME-ICME pairs for solar cycle 23 and 24. We grouped the CME-ICME events according to their dominant inclination and statistically tested the difference between the propagation properties of the two groups. We analysed the transit time (an indicator of the drag experienced by the CME during propagation), the drag parameter γ and the non-radial flows within the sheath region. We found the difference for the non-radial flows for the two groups of events, but the difference in drag was not found. The non-radial flow difference found can be interpreted as the ambient plasma bypassing the FR driver in the direction where the extent of the front of the FR is smaller. For events with low inclination, this is the meridional plane, for events with high inclination the ecliptic plane. In Martinić et al. (2024), we investigated the effects of inclination by performing two simulations using the EUHFORIA 3D MHD model and the spheromak representation of the CME. The simulations performed differ only in the inclination of the embedded spheromak. In one simulation the toroidal axis of the spheromak lies in the ecliptic plane (CME with low inclination), in the other simulation the toroidal axis of the spheromak lies in the meridional plane (CME with high inclination). The simulation setup was chosen to minimise the interaction of the CME with a heliospheric current sheath and to minimise the tilting and drifting (Asvestari et al., 2022). We found that the sheath region duration increases exponentially with increasing radial distance and that the sheath increases with the latitude/longitude distance from the CMEs' apex. We found that the non-radial flows in the simulation for both spheromaks are higher outside the ecliptic than in the ecliptic. This confirms the hypothesis put forward in observational studies that the transverse IMF component (indicative of the Parker spiral configuration) slips perpendicular to the CME motion due to the developed pressure gradient, as highlighted in Gosling & McComas

(1987). The significant differences in the simulations for the two spheromaks were not found. Although the spheromak becomes flatter in the course of the simulation, it is a spherical structure at the beginning of the simulation (equal extent of the front in the meridional and ecliptic planes), which most likely masks the influence of the inclination.

The studies presented show the importance of the inclination effects of CMEs, but also highlight the need for a better understanding of the small- and large-scale processes that contribute to the overall drag of the CME during its propagation in the heliosphere through a combination of observations and modeling approaches.

References

- Abraham-Shrauner B., Yun S. H., 1976, *J. Geophys. Res.*, 81, 2097, *Interplanetary shocks seen by Ames Plasma Probe on Pioneer 6 and 7*
- Al-Haddad N., et al., 2013, *Sol. Phys.*, 284, 129, *Magnetic Field Configuration Models and Reconstruction Methods for Interplanetary Coronal Mass Ejections*
- Al-Haddad N., Galvin A. B., Lugaz N., Farrugia C. J., Yu W., 2022, *ApJ*, 927, 68, *Investigating the Cross Sections of Coronal Mass Ejections through the Study of Nonradial Flows with STEREO/PLASTIC*
- Altschuler M. D., Newkirk G., 1969, *Sol. Phys.*, 9, 131, *Magnetic Fields and the Structure of the Solar Corona. I: Methods of Calculating Coronal Fields*
- Amerstorfer T., Möstl C., Hess P., Temmer M., Mays M. L., Reiss M. A., Lowrance P., Bourdin P. A., 2018, *Space Weather*, 16, 784, *Ensemble Prediction of a Halo Coronal Mass Ejection Using Heliospheric Imagers*
- Amerstorfer T., et al., 2021, *Space Weather*, 19, e02553, *Evaluation of CME Arrival Prediction Using Ensemble Modeling Based on Heliospheric Imaging Observations*
- Arlt R., 2011, *Astronomische Nachrichten*, 332, 805, *The sunspot observations by Samuel Heinrich Schwabe*
- Asvestari E., Rindlisbacher T., Pomoell J., Kilpua E. K. J., 2022, *ApJ*, 926, 87, *The Spheromak Tilting and How it Affects Modeling Coronal Mass Ejections*
- Aulanier G., Janvier M., Schmieder B., 2012, *A&A*, 543, A110, *The standard flare model in three dimensions. I. Strong-to-weak shear transition in post-flare loops*
- Babcock H. W., 1961, *ApJ*, 133, 572, *The Topology of the Sun's Magnetic Field and the 22-YEAR Cycle.*
- Balogh A., Beek T. J., Forsyth R. J., Hedgecock P. C., Marquedant R. J., Smith E. J., Southwood D. J., Tsurutani B. T., 1992, *A&AS*, 92, 221, *The magnetic field investigation on the ULYSSES mission - Instrumentation and preliminary scientific results*
- Behannon K. W., Acuna M. H., Burlaga L. F., Lepping R. P., Ness N. F., Neubauer F. M., 1977, *Space Sci. Rev.*, 21, 235, *Magnetic Field Experiment for Voyagers 1 and 2*
- Berghmans D., et al., 2023, *A&A*, 675, A110, *First perihelion of EUI on the Solar Orbiter mission*
- Bothmer V., Schwenn R., 1998, *Annales Geophysicae*, 16, 1, *The structure and origin of magnetic clouds in the solar wind*
- Bueckner G. E., et al., 1995, *Sol. Phys.*, 162, 357, *The Large Angle Spectroscopic Coronagraph (LASCO)*
- Brun A. S., Browning M. K., 2017, *Living Reviews in Solar Physics*, 14, 4, *Magnetism, dynamo action and the solar-stellar connection*
- Burlaga L., Sittler E., Mariani F., Schwenn R., 1981, *J. Geophys. Res.*, 86, 6673, *Magnetic loop behind an interplanetary shock: Voyager, Helios, and IMP 8 observations*
- Burlaga L. F., Ness N. F., Acuña M. H., Lepping R. P., Connerney J. E. P., Stone E. C., McDonald F. B., 2005, *Science*, 309, 2027, *Crossing the Termination Shock into the Heliosheath: Magnetic Fields*
- Byrne J. P., Gallagher P. T., McAteer R. T. J., Young C. A., 2009, *A&A*, 495, 325, *The kinematics of coronal mass ejections using multiscale methods*
- Cane H. V., Richardson I. G., 2003, *Journal of Geophysical Research (Space Physics)*, 108, 1156, *Interplanetary coronal mass ejections in the near-Earth solar wind during 1996-2002*

- Cargill P. J., 2004, *Sol. Phys.*, 221, 135, *On the Aerodynamic Drag Force Acting on Interplanetary Coronal Mass Ejections*
- Cargill P. J., Chen J., Spicer D. S., Zalesak S. T., 1996, *J. Geophys. Res.*, 101, 4855, *Magnetohydrodynamic simulations of the motion of magnetic flux tubes through a magnetized plasma*
- Carmichael H., 1964, in , Vol. 50, NASA Special Publication. p. 451
- Carrington R. C., 1859, *MNRAS*, 20, 13, *Description of a Singular Appearance seen in the Sun on September 1, 1859*
- Chané E., van der Holst B., Jacobs C., Poedts S., Kimpe D., 2006, *A&A*, 447, 727, *Inverse and normal coronal mass ejections: evolution up to 1 AU*
- Charbonneau P., 2010, *Living Reviews in Solar Physics*, 7, 3, *Dynamo Models of the Solar Cycle*
- Chen J., 1996, *J. Geophys. Res.*, 101, 27499, *Theory of prominence eruption and propagation: Interplanetary consequences*
- Chen J., Garren D. A., 1993, *Geophys. Res. Lett.*, 20, 2319, *Interplanetary magnetic clouds: Topology and driving mechanism*
- Chen J., et al., 1997, *ApJ*, 490, L191, *Evidence of an Erupting Magnetic Flux Rope: LASCO Coronal Mass Ejection of 1997 April 13*
- Chiu M. C., et al., 1998, *Space Sci. Rev.*, 86, 257, *ACE Spacecraft*
- Colburn D. S., Sonett C. P., 1966, *Space Sci. Rev.*, 5, 439, *Discontinuities in the Solar Wind*
- Cummings A. C., et al., 2016, *ApJ*, 831, 18, *Galactic Cosmic Rays in the Local Interstellar Medium: Voyager 1 Observations and Model Results*
- Dasso S., Mandrini C. H., Démoulin P., Luoni M. L., 2006, *A&A*, 455, 349, *A new model-independent method to compute magnetic helicity in magnetic clouds*
- Delaboudinière J. P., et al., 1995, *Sol. Phys.*, 162, 291, *EIT: Extreme-Ultraviolet Imaging Telescope for the SOHO Mission*
- Domingo V., Fleck B., Poland A. I., 1995, *Sol. Phys.*, 162, 1, *The SOHO Mission: an Overview*
- Dumbović M., et al., 2015, *Sol. Phys.*, 290, 579, *Geoeffectiveness of Coronal Mass Ejections in the SOHO Era*
- Dumbović M., Čalogović J., Vršnak B., Temmer M., Mays M. L., Veronig A., Piantschitsch I., 2018, *ApJ*, 854, 180, *The Drag-based Ensemble Model (DBEM) for Coronal Mass Ejection Propagation*
- Dumbović M., Čalogović J., Martinić K., Vršnak B., Sudar D., Temmer M., Veronig A., 2021, *Frontiers in Astronomy and Space Sciences*, 8, 58, *Drag-based model (DBM) tools for forecast of coronal mass ejection arrival time and speed*
- Duvall T. L. J., 1979, *Sol. Phys.*, 63, 3, *Large-scale solar velocity fields.*
- Fan Y., Gibson S. E., 2004, *ApJ*, 609, 1123, *Numerical Simulations of Three-dimensional Coronal Magnetic Fields Resulting from the Emergence of Twisted Magnetic Flux Tubes*
- Gopalswamy N., Lara A., Lepping R. P., Kaiser M. L., Berdichevsky D., St. Cyr O. C., 2000, *Geophys. Res. Lett.*, 27, 145, *Interplanetary acceleration of coronal mass ejections*
- Gopalswamy N., Lara A., Yashiro S., Kaiser M. L., Howard R. A., 2001, *J. Geophys. Res.*, 106, 29207, *Predicting the 1-AU arrival times of coronal mass ejections*
- Gosling J. T., 1990, *Washington DC American Geophysical Union Geophysical Monograph Series*, 58, 343, *Coronal mass ejections and magnetic flux ropes in interplanetary space*
- Gosling J. T., 1993, *J. Geophys. Res.*, 98, 18937, *The solar flare myth*
- Gosling J. T., McComas D. J., 1987, *Geophys. Res. Lett.*, 14, 355, *Field line draping about fast coronal mass ejecta: A source of strong out-of-the-ecliptic interplanetary magnetic fields*
- Gosling J. T., Hildner E., MacQueen R. M., Munro R. H., Poland A. I., Ross C. L., 1975, *Sol. Phys.*, 40, 439, *Direct Observations of a Flare Related Coronal and Solar Wind Disturbance*
- Green L. M., Kliem B., Török T., van Driel-Gesztelyi L., Attrill G. D. R., 2007, *Sol. Phys.*, 246, 365, *Transient Coronal Sigmoids and Rotating Erupting Flux Ropes*
- Hale G. E., 1908, *ApJ*, 28, 315, *On the Probable Existence of a Magnetic Field in Sun-Spots*

- Harvey J. W., et al., 1996, *Science*, 272, 1284, *The Global Oscillation Network Group (GONG) Project*
- Hayes A. P., Vourlidas A., Howard R. A., 2001, *ApJ*, 548, 1081, *Deriving the Electron Density of the Solar Corona from the Inversion of Total Brightness Measurements*
- Hess P., Zhang J., 2014, *ApJ*, 792, 49, *Stereoscopic Study of the Kinematic Evolution of a Coronal Mass Ejection and Its Driven Shock from the Sun to the Earth and the Prediction of Their Arrival Times*
- Hess P., Zhang J., 2015, *ApJ*, 812, 144, *Predicting CME Ejecta and Sheath Front Arrival at L1 with a Data-constrained Physical Model*
- Hirayama T., 1974, *Sol. Phys.*, 34, 323, *Theoretical Model of Flares and Prominences. I: Evaporating Flare Model*
- Hodgson R., 1859, *MNRAS*, 20, 15, *On a curious Appearance seen in the Sun*
- Hoeksema J. T., Wilcox J. M., Scherrer P. H., 1982, *J. Geophys. Res.*, 87, 10331, *Structure of the heliospheric current sheet in the early portion of sunspot cycle 21*
- Howard R. A., 2006, *Geophysical Monograph Series*, 165, 7, *A Historical Perspective on Coronal Mass Ejections*
- Howard R. A., et al., 2008, *Space Sci. Rev.*, 136, 67, *Sun Earth Connection Coronal and Heliospheric Investigation (SECCHI)*
- Howard T. A., DeForest C. E., Schneck U. G., Alden C. R., 2017, *ApJ*, 834, 86, *Challenging Some Contemporary Views of Coronal Mass Ejections. II. The Case for Absent Filaments*
- Howe R., 2009, *Living Reviews in Solar Physics*, 6, 1, *Solar Interior Rotation and its Variation*
- Hudson H. S., Bougeret J. L., Burkepile J., 2006, *Space Sci. Rev.*, 123, 13, *Coronal Mass Ejections: Overview of Observations*
- Huttunen K., Koskinen H., 2004, *Annales Geophysicae*, 22, 1729, *Importance of post-shock streams and sheath region as drivers of intense magnetospheric storms and high-latitude activity*
- Huttunen K. E. J., Koskinen H. E. J., Schwenn R., 2002, *Journal of Geophysical Research (Space Physics)*, 107, 1121, *Variability of magnetospheric storms driven by different solar wind perturbations*
- Isavnin A., 2016, *ApJ*, 833, 267, *FRiED: A Novel Three-dimensional Model of Coronal Mass Ejections*
- Isavnin A., Vourlidas A., Kilpua E. K. J., 2013, *Sol. Phys.*, 284, 203, *Three-Dimensional Evolution of Erupted Flux Ropes from the Sun ($2 - 20 R_{\odot}$) to 1 AU*
- Isavnin A., Vourlidas A., Kilpua E. K. J., 2014, *Sol. Phys.*, 289, 2141, *Three-Dimensional Evolution of Flux-Rope CMEs and Its Relation to the Local Orientation of the Heliospheric Current Sheet*
- Janvier M., Aulanier G., Pariat E., Démoulin P., 2013, *A&A*, 555, A77, *The standard flare model in three dimensions. III. Slip-running reconnection properties*
- Janvier M., et al., 2019, *Journal of Geophysical Research (Space Physics)*, 124, 812, *Generic Magnetic Field Intensity Profiles of Interplanetary Coronal Mass Ejections at Mercury, Venus, and Earth From Superposed Epoch Analyses*
- Kay C., Gopalswamy N., 2018, *Journal of Geophysical Research (Space Physics)*, 123, 7220, *The Effects of Uncertainty in Initial CME Input Parameters on Deflection, Rotation, B_z , and Arrival Time Predictions*
- Kay C., Palmerio E., 2024, *Space Weather*, 22, e2023SW003796, *Collection, Collation, and Comparison of 3D Coronal CME Reconstructions*
- Kay C., Opher M., Evans R. M., 2013, *ApJ*, 775, 5, *Forecasting a Coronal Mass Ejection's Altered Trajectory: ForeCAT*
- Kay C., Opher M., Evans R. M., 2015, *ApJ*, 805, 168, *Global Trends of CME Deflections Based on CME and Solar Parameters*
- Kay C., Gopalswamy N., Xie H., Yashiro S., 2017, *Sol. Phys.*, 292, 78, *Deflection and Rotation of CMEs from Active Region 11158*
- Kay C., Mays M. L., Verbeke C., 2020, *Space Weather*, 18, e02382, *Identifying Critical Input Parameters for Improving Drag-Based CME Arrival Time Predictions*
- Kay C., et al., 2024, *Space Weather*, 22, e2024SW003951, *Updating Measures of CME Arrival Time Errors*
- Kilpua E. K. J., Isavnin D., Vourlidas A., Koskinen H. E. J., Rodriguez L., 2013, *Annales Geophysicae*, 31, 1251, *On the relationship between interplanetary coronal mass ejections and magnetic clouds*

- Kilpua E., Koskinen H. E. J., Pulkkinen T. I., 2017, *Living Reviews in Solar Physics*, 14, 5, *Coronal mass ejections and their sheath regions in interplanetary space*
- King J. H., Papitashvili N. E., 2005, *Journal of Geophysical Research (Space Physics)*, 110, A02104, *Solar wind spatial scales in and comparisons of hourly Wind and ACE plasma and magnetic field data*
- Kivelson L., Russel L., 1996, *Solar Wind*. p. 152
- Klein L. W., Burlaga L. F., 1982, *J. Geophys. Res.*, 87, 613, *Interplanetary magnetic clouds at 1 AU*
- Kopp R. A., Pneuman G. W., 1976, *Sol. Phys.*, 50, 85, *Magnetic reconnection in the corona and the loop prominence phenomenon.*
- Koskinen H. E. J., Huttunen K. E. J., 2006, *Space Sci. Rev.*, 124, 169, *Geoeffectivity of Coronal Mass Ejections*
- Krall J., St. Cyr O. C., 2006, *ApJ*, 652, 1740, *Flux-Rope Coronal Mass Ejection Geometry and Its Relation to Observed Morphology*
- Larrodera C., Temmer M., 2024, *A&A*, 685, A89, *Evolution of coronal mass ejections with and without sheaths from the inner to the outer heliosphere: Statistical investigation for 1975 to 2022*
- Leighton R. B., 1969, *ApJ*, 156, 1, *A Magneto-Kinematic Model of the Solar Cycle*
- Lemen J. R., et al., 2012, *Sol. Phys.*, 275, 17, *The Atmospheric Imaging Assembly (AIA) on the Solar Dynamics Observatory (SDO)*
- Liu Y., Luhmann J. G., Bale S. D., Lin R. P., 2011, *ApJ*, 734, 84, *Solar Source and Heliospheric Consequences of the 2010 April 3 Coronal Mass Ejection: A Comprehensive View*
- Liu J., Ye Y., Shen C., Wang Y., Erdélyi R., 2018, *ApJ*, 855, 109, *A New Tool for CME Arrival Time Prediction using Machine Learning Algorithms: CAT-PUMA*
- Lundquist S., 1950, *Ark. Fys.*, *Magnetohydrostatic fields*
- Lynch B. J., Antiochos S. K., Li Y., Luhmann J. G., DeVore C. R., 2009, *ApJ*, 697, 1918, *Rotation of Coronal Mass Ejections during Eruption*
- Maharana A., Isavnin A., Scolini C., Wijzen N., Rodriguez L., Mierla M., Magdalenic J., Poedts S., 2022, *Advances in Space Research*, 70, 1641, *Implementation and validation of the FRI3D flux rope model in EUHFORIA*
- Manchester W. B. I., et al., 2005, *ApJ*, 622, 1225, *Coronal Mass Ejection Shock and Sheath Structures Relevant to Particle Acceleration*
- Manoharan P. K., 2006, *Sol. Phys.*, 235, 345, *Evolution of Coronal Mass Ejections in the Inner Heliosphere: A Study Using White-Light and Scintillation Images*
- Maričić D., et al., 2020, *Sol. Phys.*, 295, 91, *Sun-to-Earth Observations and Characteristics of Isolated Earth-Impacting Interplanetary Coronal Mass Ejections During 2008 - 2014*
- Martinić K., Dumbović M., Temmer M., Veronig A., Vršnak B., 2022, *A&A*, 661, A155, *Determination of coronal mass ejection orientation and consequences for their propagation*
- Martinić K., Dumbović M., Čalogović J., Vršnak B., Al-Haddad N., Temmer M., 2023, *A&A*, 679, A97, *Effects of coronal mass ejection orientation on its propagation in the heliosphere*
- Martinić K., Asvestari E., Dumbović M., Rindlisbacher T., Temmer M., Vršnak B., 2024, arXiv e-prints, p. arXiv:2408.14971, *Probing coronal mass ejections inclination effects with EUHFORIA*
- Marubashi K., Akiyama S., Yashiro S., Gopalswamy N., Cho K. S., Park Y. D., 2015, *Sol. Phys.*, 290, 1371, *Geometrical Relationship Between Interplanetary Flux Ropes and Their Solar Sources*
- McComas D. J., Gosling J. T., Winterhalter D., Smith E. J., 1988, *J. Geophys. Res.*, 93, 2519, *Interplanetary magnetic field draping about fast coronal mass ejecta in the outer heliosphere*
- McComas D. J., Gosling J. T., Bame S. J., Smith E. J., Cane H. V., 1989, *J. Geophys. Res.*, 94, 1465, *A test of magnetic field draping induced B_z perturbations ahead of fast coronal mass ejecta*
- McComas D. J., Elliott H. A., Schwadron N. A., Gosling J. T., Skoug R. M., Goldstein B. E., 2003, *Geophys. Res. Lett.*, 30, 1517, *The three-dimensional solar wind around solar maximum*
- Moore R. L., Sterling A. C., Hudson H. S., Lemen J. R., 2001, *ApJ*, 552, 833, *Onset of the Magnetic Explosion in Solar Flares and Coronal Mass Ejections*

- Möstl C., Miklenic C., Farrugia C. J., Temmer M., Veronig A., Galvin A. B., Vršnak B., Biernat H. K., 2008, *Annales Geophysicae*, 26, 3139, *Two-spacecraft reconstruction of a magnetic cloud and comparison to its solar source*
- Möstl C., et al., 2015, *Nature Communications*, 6, 7135, *Strong coronal channelling and interplanetary evolution of a solar storm up to Earth and Mars*
- Möstl C., et al., 2017, *Space Weather*, 15, 955, *Modeling observations of solar coronal mass ejections with heliospheric imagers verified with the Heliophysics System Observatory*
- Möstl C., et al., 2018, *Space Weather*, 16, 216, *Forward Modeling of Coronal Mass Ejection Flux Ropes in the Inner Heliosphere with 3DCORE*
- Müller D., et al., 2017, *A&A*, 606, A10, *JHelioviewer. Time-dependent 3D visualisation of solar and heliospheric data*
- Müller D., et al., 2020, *A&A*, 642, A1, *The Solar Orbiter mission. Science overview*
- Mulligan T., Russell C. T., Luhmann J. G., 1998, *Geophys. Res. Lett.*, 25, 2959, *Solar cycle evolution of the structure of magnetic clouds in the inner heliosphere*
- Napoletano G., Forte R., Del Moro D., Pietropaolo E., Giovannelli L., Berrilli F., 2018, *Journal of Space Weather and Space Climate*, 8, A11, *A probabilistic approach to the drag-based model*
- Nieves-Chinchilla T., Vourlidas A., Raymond J. C., Linton M. G., Al-haddad N., Savani N. P., Szabo A., Hidalgo M. A., 2018, *Sol. Phys.*, 293, 25, *Understanding the Internal Magnetic Field Configurations of ICMEs Using More than 20 Years of Wind Observations*
- Nitta N., Mulligan Skov T., 2017, in *AGU Fall Meeting Abstracts*. pp SH51E–04
- Odstrčil D., Pizzo V. J., Linker J. A., Riley P., Lionello R., Mikic Z., 2004, *Journal of Atmospheric and Solar-Terrestrial Physics*, 66, 1311, *Initial coupling of coronal and heliospheric numerical magnetohydrodynamic codes*
- Odstrčil D., Pizzo V. J., 1999, *J. Geophys. Res.*, 104, 483, *Three-dimensional propagation of CMEs in a structured solar wind flow: 1. CME launched within the streamer belt*
- Ogilvie K. W., Parks G. K., 1996, *Geophys. Res. Lett.*, 23, 1179, *First results from WIND spacecraft: An introduction*
- Owens M., Cargill P., 2004, *Annales Geophysicae*, 22, 4397, *Non-radial solar wind flows induced by the motion of interplanetary coronal mass ejections*
- Owens M. J., Forsyth R. J., 2013, *Living Reviews in Solar Physics*, 10, 5, *The Heliospheric Magnetic Field*
- Pal S., Kilpua E., Good S., Pomoell J., Price D. J., 2021, *A&A*, 650, A176, *Uncovering erosion effects on magnetic flux rope twist*
- Palmerio E., et al., 2018, *Space Weather*, 16, 442, *Coronal Magnetic Structure of Earthbound CMEs and In Situ Comparison*
- Paouris E., Čalogović J., Dumbović M., Mays M. L., Vourlidas A., Papaioannou A., Anastasiadis A., Balasis G., 2021, *Sol. Phys.*, 296, 12, *Propagating Conditions and the Time of ICME Arrival: A Comparison of the Effective Acceleration Model with ENLIL and DBEM Models*
- Parker E. N., 1955, *ApJ*, 121, 491, *The Formation of Sunspots from the Solar Toroidal Field.*
- Parker E. N., 1958, *ApJ*, 128, 664, *Dynamics of the Interplanetary Gas and Magnetic Fields.*
- Pesnell W. D., Thompson B. J., Chamberlin P. C., 2012, *Sol. Phys.*, 275, 3, *The Solar Dynamics Observatory (SDO)*
- Pneuman G. W., Kopp R. A., 1971, *Sol. Phys.*, 18, 258, *Gas-Magnetic Field Interactions in the Solar Corona*
- Pomoell J., Poedts S., 2018, *Journal of Space Weather and Space Climate*, 8, A35, *EUHFORIA: European heliospheric forecasting information asset*
- Raouafi N. E., et al., 2023, *Space Sci. Rev.*, 219, 8, *Parker Solar Probe: Four Years of Discoveries at Solar Cycle Minimum*
- Richardson I. G., Cane H. V., 2010, *Sol. Phys.*, 264, 189, *Near-Earth Interplanetary Coronal Mass Ejections During Solar Cycle 23 (1996 - 2009): Catalog and Summary of Properties*

- Riley P., Linker J. A., Mikić Z., 2001, *J. Geophys. Res.*, 106, 15889, *An empirically-driven global MHD model of the solar corona and inner heliosphere*
- Rodari M., Dumbović M., Temmer M., Holzkecht L., Veronig A., 2018, *Central European Astrophysical Bulletin*, 42, 11, *3D reconstruction and interplanetary expansion of the 2010 April 3rd CME*
- Rollett T., Möstl C., Temmer M., Veronig A. M., Farrugia C. J., Biernat H. K., 2012, *Sol. Phys.*, 276, 293, *Constraining the Kinematics of Coronal Mass Ejections in the Inner Heliosphere with In-Situ Signatures*
- Rollett T., Möstl C., Isavnin A., Davies J. A., Kubicka M., Amerstorfer U. V., Harrison R. A., 2016, *ApJ*, 824, 131, *ElEvoHI: A Novel CME Prediction Tool for Heliospheric Imaging Combining an Elliptical Front with Drag-based Model Fitting*
- Ruffenach A., et al., 2015, *Journal of Geophysical Research (Space Physics)*, 120, 43, *Statistical study of magnetic cloud erosion by magnetic reconnection*
- Russell C. T., 2008, *The STEREO Mission*. Springer Science & Business Media
- Sachdeva N., 2019, arXiv e-prints, p. arXiv:1907.12673, *Dynamics of solar Coronal Mass Ejections: forces that impact their propagation*
- Sachdeva N., Subramanian P., Colaninno R., Vourlidas A., 2015, *ApJ*, 809, 158, *CME Propagation: Where does Aerodynamic Drag 'Take Over'?*
- Salman T. M., Lugaz N., Farrugia C. J., Winslow R. M., Jian L. K., Galvin A. B., 2020, *ApJ*, 904, 177, *Properties of the Sheath Regions of Coronal Mass Ejections with or without Shocks from STEREO in situ Observations near 1 au*
- Sarkar R., Pomoell J., Kilpua E., Asvestari E., Wijzen N., Maharana A., Poedts S., 2024, *ApJS*, 270, 18, *Studying the Spheromak Rotation in Data-constrained Coronal Mass Ejection Modeling with EUHFORIA and Assessing Its Effect on the B_z Prediction*
- Schatten K. H., Wilcox J. M., Ness N. F., 1969, *Sol. Phys.*, 6, 442, *A model of interplanetary and coronal magnetic fields*
- Scherrer P. H., et al., 1995, *Sol. Phys.*, 162, 129, *The Solar Oscillations Investigation - Michelson Doppler Imager*
- Scherrer P. H., et al., 2012, *Sol. Phys.*, 275, 207, *The Helioseismic and Magnetic Imager (HMI) Investigation for the Solar Dynamics Observatory (SDO)*
- Schwabe H., 1844, *Astronomische Nachrichten*, 21, 233, *Sonnenbeobachtungen im Jahre 1843. Von Herrn Hofrath Schwabe in Dessau*
- Schwenn R., 2006, *Space Sci. Rev.*, 124, 51, *Solar Wind Sources and Their Variations Over the Solar Cycle*
- Scolini C., Dasso S., Rodriguez L., Zhukov A. N., Poedts S., 2021, *A&A*, 649, A69, *Exploring the radial evolution of interplanetary coronal mass ejections using EUHFORIA*
- Sheeley N. R., Walters J. H., Wang Y. M., Howard R. A., 1999, *J. Geophys. Res.*, 104, 24739, *Continuous tracking of coronal outflows: Two kinds of coronal mass ejections*
- Shen F., Liu Y., Yang Y., 2021, *ApJS*, 253, 12, *Numerical Research on the Effect of the Initial Parameters of a CME Flux-rope Model on Simulation Results*
- Shi T., Wang Y., Wan L., Cheng X., Ding M., Zhang J., 2015, *ApJ*, 806, 271, *Predicting the Arrival Time of Coronal Mass Ejections with the Graduated Cylindrical Shell and Drag Force Model*
- Shibata K., Masuda S., Shimojo M., Hara H., Yokoyama T., Tsuneta S., Kosugi T., Ogawara Y., 1995, *ApJ*, 451, L83, *Hot-Plasma Ejections Associated with Compact-Loop Solar Flares*
- Singh T., Yalim M. S., Pogorelov N. V., 2018, *ApJ*, 864, 18, *A Data-constrained Model for Coronal Mass Ejections Using the Graduated Cylindrical Shell Method*
- Siscoe G., Odstrcil D., 2008, *Journal of Geophysical Research (Space Physics)*, 113, A00B07, *Ways in which ICME sheaths differ from magnetosheaths*
- Siscoe G., MacNeice P. J., Odstrcil D., 2007, *Space Weather*, 5, S04002, *East-west asymmetry in coronal mass ejection geoeffectiveness*
- Smith E. J., 2001, *J. Geophys. Res.*, 106, 15819, *The heliospheric current sheet*

- Song H., Zhang J., Li L., Yang Z., Xia L., Zheng R., Chen Y., 2023, *ApJ*, 942, 19, *On the Nature of the Three-part Structure of Solar Coronal Mass Ejections*
- Steenbeck M., Krause F., Rädler K. H., 1966, *Zeitschrift Naturforschung Teil A*, 21, 369, *Berechnung der mittleren LORENTZ-Feldstärke $v \times B$ für ein elektrisch leitendes Medium in turbulenter, durch CORIOLIS-Kräfte beeinflusster Bewegung*
- Stone E. C., Cummings A. C., McDonald F. B., Heikkilä B. C., Lal N., Webber W. R., 2013, *Science*, 341, 150, *Voyager 1 Observes Low-Energy Galactic Cosmic Rays in a Region Depleted of Heliospheric Ions*
- Sturrock P. A., 1966, *Nature*, 211, 695, *Model of the High-Energy Phase of Solar Flares*
- Sudar D., Vršnak B., Dumbović M., 2016, *MNRAS*, 456, 1542, *Predicting coronal mass ejections transit times to Earth with neural network*
- Temmer M., 2021, *Living Reviews in Solar Physics*, 18, 4, *Space weather: the solar perspective*
- Temmer M., Bothmer V., 2022, *A&A*, 665, A70, *Characteristics and evolution of sheath and leading edge structures of interplanetary coronal mass ejections in the inner heliosphere based on Helios and Parker Solar Probe observations*
- Temmer M., Rollett T., Möstl C., Veronig A. M., Vršnak B., Odstrčil D., 2011, *ApJ*, 743, 101, *Influence of the Ambient Solar Wind Flow on the Propagation Behavior of Interplanetary Coronal Mass Ejections*
- Temmer M., et al., 2012, *ApJ*, 749, 57, *Characteristics of Kinematics of a Coronal Mass Ejection during the 2010 August 1 CME-CME Interaction Event*
- Temmer M., et al., 2023, arXiv e-prints, p. arXiv:2308.04851, *CME Propagation Through the Heliosphere: Status and Future of Observations and Model Development*
- Thernisien A., 2011, *ApJS*, 194, 33, *Implementation of the Graduated Cylindrical Shell Model for the Three-dimensional Reconstruction of Coronal Mass Ejections*
- Thernisien A. F. R., Howard R. A., Vourlidas A., 2006, *ApJ*, 652, 763, *Modeling of Flux Rope Coronal Mass Ejections*
- Toriumi S., Wang H., 2019, *Living Reviews in Solar Physics*, 16, 3, *Flare-productive active regions*
- Török T., et al., 2018, *ApJ*, 856, 75, *Sun-to-Earth MHD Simulation of the 2000 July 14 “Bastille Day” Eruption*
- Tousey R., 1973, in *Space Research Conference*. pp 713–730
- Tsurutani B. T., Gonzalez W. D., Tang F., Akasofu S. I., Smith E. J., 1988, *J. Geophys. Res.*, 93, 8519, *Origin of interplanetary southward magnetic fields responsible for major magnetic storms near solar maximum (1978-1979)*
- Ulrich R. K., 2010, *ApJ*, 725, 658, *Solar Meridional Circulation from Doppler Shifts of the Fe I Line at 5250 Å as Measured by the 150-foot Solar Tower Telescope at the Mt. Wilson Observatory*
- Vandas M., Fischer S., Dryer M., Smith Z., Detman T., 1995, *J. Geophys. Res.*, 100, 12285, *Simulation of magnetic cloud propagation in the inner heliosphere in two-dimensions. 1. A loop perpendicular to the ecliptic plane*
- Vandas M., Fischer S., Dryer M., Smith Z., Detman T., 1996, *J. Geophys. Res.*, 101, 2505, *Simulation of magnetic cloud propagation in the inner heliosphere in two dimensions 2. A loop parallel to the ecliptic plane and the role of helicity*
- Verbeke C., Pomoell J., Poedts S., 2019, *A&A*, 627, A111, *The evolution of coronal mass ejections in the inner heliosphere: Implementing the spheromak model with EUHFORIA*
- Verbeke C., et al., 2023, *Advances in Space Research*, 72, 5243, *Quantifying errors in 3D CME parameters derived from synthetic data using white-light reconstruction techniques*
- Vourlidas A., Colaninno R., Nieves-Chinchilla T., Stenborg G., 2011, *ApJ*, 733, L23, *The First Observation of a Rapidly Rotating Coronal Mass Ejection in the Middle Corona*
- Vourlidas A., Lynch B. J., Howard R. A., Li Y., 2013, *Sol. Phys.*, 284, 179, *How Many CMEs Have Flux Ropes? Deciphering the Signatures of Shocks, Flux Ropes, and Prominences in Coronagraph Observations of CMEs*
- Vourlidas A., Patsourakos S., Savani N. P., 2019, *Philosophical Transactions of the Royal Society of London Series A*, 377, 20180096, *Predicting the geoeffective properties of coronal mass ejections: current status, open issues and path forward*

- Vršnak B., 2001, *Sol. Phys.*, 202, 173, *Deceleration of Coronal Mass Ejections*
- Vršnak B., Ruždjak D., Sudar D., Gopalswamy N., 2004, *A&A*, 423, 717, *Kinematics of coronal mass ejections between 2 and 30 solar radii. What can be learned about forces governing the eruption?*
- Vršnak B., Vrbanec D., Čalogović J., 2008, *A&A*, 490, 811, *Dynamics of coronal mass ejections. The mass-scaling of the aerodynamic drag*
- Vršnak B., et al., 2013, *Sol. Phys.*, 285, 295, *Propagation of Interplanetary Coronal Mass Ejections: The Drag-Based Model*
- Vršnak B., et al., 2014, *ApJS*, 213, 21, *Heliospheric Propagation of Coronal Mass Ejections: Comparison of Numerical WSA-ENLIL+Cone Model and Analytical Drag-based Model*
- Vršnak B., Žic T., Lulić S., Temmer M., Veronig A. M., 2016, *Sol. Phys.*, 291, 89, *Formation of Coronal Large-Amplitude Waves and the Chromospheric Response*
- Wang Y. M., Sheeley N. R. J., 1990, *ApJ*, 355, 726, *Solar Wind Speed and Coronal Flux-Tube Expansion*
- Wang Y. M., Sheeley N. R. J., Lean J., 2000, *Geophys. Res. Lett.*, 27, 621, *Understanding the evolution of the Sun's open magnetic flux*
- Wang J., Liu S., Luo B., 2023, *Advances in Space Research*, 72, 5263, *Analyzing deflection of multiple Solar Coronal Mass Ejections from the same active region*
- Wolf R., 1856, *Astronomische Mitteilungen der Eidgenössischen Sternwarte Zurich*, 1, 3, *Mittheilungen über die Sonnenflecken I*
- Wu S. T., Han S. M., Dryer M., 1979, *Planet. Space Sci.*, 27, 255, *Two-dimensional, time-dependent MHD description of interplanetary disturbances: Simulation of high speed solar wind interactions*
- Wu S. T., Dryer M., Han S. M., 1983, *Sol. Phys.*, 84, 395, *Non-Planar Magnetohydrodynamic Model for Solar Flare Generated Disturbances in the Heliospheric Equatorial Plane*
- Xie H., Gopalswamy N., Akiyama S., 2021, *ApJ*, 922, 64, *The Structural Connection between Coronal Mass Ejection Flux Ropes near the Sun and at 1 au*
- Yurchyshyn V., 2008, in *AGU Fall Meeting Abstracts*. pp SH13B–1551
- Yurchyshyn V., Abramenko V., Tripathi D., 2009, *ApJ*, 705, 426, *Rotation of White-light Coronal Mass Ejection Structures as Inferred from LASCO Coronagraph*
- Zhang J., Dere K. P., Howard R. A., Bothmer V., 2003, *ApJ*, 582, 520, *Identification of Solar Sources of Major Geomagnetic Storms between 1996 and 2000*
- Zhang J., Liemohn M. W., Kozyra J. U., Lynch B. J., Zurbuchen T. H., 2004, *Journal of Geophysical Research (Space Physics)*, 109, A09101, *A statistical study of the geoeffectiveness of magnetic clouds during high solar activity years*
- Zhang J., et al., 2021a, *Progress in Earth and Planetary Science*, 8, 56, *Earth-affecting solar transients: a review of progresses in solar cycle 24*
- Zhang J., et al., 2021b, *Progress in Earth and Planetary Science*, 8, 56, *Earth-affecting solar transients: a review of progresses in solar cycle 24*
- Zhou Y., Feng X., Zhao X., 2014, *Journal of Geophysical Research (Space Physics)*, 119, 9321, *Using a 3-D MHD simulation to interpret propagation and evolution of a coronal mass ejection observed by multiple spacecraft: The 3 April 2010 event*
- Čalogović J., Dumbović M., Sudar D., Vršnak B., Martinić K., Temmer M., Veronig A. M., 2021, *Sol. Phys.*, 296, 114, *Probabilistic Drag-Based Ensemble Model (DBEM) Evaluation for Heliospheric Propagation of CMEs*
- Žic T., Vršnak B., Temmer M., 2015, *ApJS*, 218, 32, *Heliospheric Propagation of Coronal Mass Ejections: Drag-based Model Fitting*
- van Driel-Gesztelyi L., Green L. M., 2015, *Living Reviews in Solar Physics*, 12, 1, *Evolution of Active Regions*

Curriculum vitae

Karmen Martinić (1994, Split) has been working at the Hvar Observatory (Faculty of Geodesy in Zagreb) since 2020. In the same year, she graduated from the Faculty of Sciences at the University of Zagreb with a thesis on "Changes in the Earth's thermosphere during geomagnetic disturbances in the final phase of the 23rd solar cycle". During her studies, she worked in the seismological service as an assistant in the preparation of the Croatian earthquake catalogue and completed an Erasmus+ internship at the German Research Centre for Geosciences (GFZ) in Potsdam, where she worked on modelling the Earth's magnetic field. As part of her scientific work, she has published 7 scientific articles so far, which are indexed in the CC database (3 as first author). She presented her research at international scientific conferences with a total of 13 abstracts (6 posters and 7 oral presentations). She participated in a total of 6 summer schools and 6 scientific stays and project meetings at recognised institutions in the field of solar and heliospheric physics throughout Europe, the USA and Brazil. She has also held two guest seminars at the University of Helsinki (Finland) and the University of New Hampshire (USA). She participates in the SCOSTEP/VarSITI MiniMax campaign, which provides daily information on the state of the Sun and its potential impact on the Earth. In addition to her research activities, she is involved in the scientific community by reviewing scientific articles, organising international meetings, participating in popular science events and being a member of the State Commission for Astronomy Competitions.

Refereed publications

Submitted

- 9 Temmer, M., Dumbović, M., **Martinić, K.**, et al., submitted to *A&A*, *Two episodes of strongly geoeffective CME events in November and December 2023 with their similarities and differences*
- 8 Čalogović, J., Dumbović, M., **Martinić, K.**, et al, submitted to *A&A*, *Constraints to the Drag-Based Reverse Modeling*

Published

- 7 **Martinić, K.**, Asvestari, E. et al., 2024, *ApJ*, 974(2), 203, *Probing coronal mass ejections inclination effects with EUHFORIA*
- 6 Dumbović, M., Karbonini, L., Čalogović, J., Matković, F., **Martinić, K.**, et al., 2024, *Solar Physics*, 299, A66, *The catalog of Hvar Observatory solar observations*
- 5 Karuppiah, S., Dumbović, M., **Martinić, K.**, et al., 2024, *Solar Physics*, 299, A87, *Early Evolution of Earth-Directed Coronal Mass Ejections in the Vicinity of Coronal Holes*
- 4 **Martinić, K.**, et al., 2023, *A&A*, 697, A97, *Effects of coronal mass ejection orientation on its propagation in the heliosphere*
- 3 **Martinić, K.**, et al., 2022, *A&A*, 661, A155, *Determination of coronal mass ejection orientation and consequences for their propagation*
- 2 Dumbović, M., Čalogović, J., **Martinić, K.**, et al., 2021, *Solar Physics*, 299, A66, *Drag-Based Model (DBM) Tools for Forecast of Coronal Mass Ejection Arrival Time and Speed*
- 1 Čalogović, J., Dumbović, M., Sudar, D., Vršnak, B., **Martinić, K.**, et al., 2021, *Front. Astron.*, 296(7), 114, *Probabilistic Drag-Based Ensemble Model (DBEM) Evaluation for Heliospheric Propagation of CMEs*

Prošireni sažetak na hrvatskom jeziku

Koronini izbačaji (engl., *coronal mass ejections*, CMEs) su najsilovitije erupcije plazme i magnetskog polja na Sunčevoj površini. CME-ovi su, pogotovo za vrijeme maksimuma Sunčeve aktivnosti glavni činitelji svemirskog vremena (engl., *space weather*). CME-ovi nakon što su izbačeni sa Sunčeve površine nastavljaju propagaciju i ekspanziju u međuplanetarnom prostoru tj. direktno međudjeluju s okolnim Sunčevim vjetrom i međuplanetarnim magnetskim poljem. Nailaskom CME-ova na Zemljinu magnetosferu dolazi do prijenosa velike količine energije u neposrednu Zemljinu okolinu zbog čega može doći do poremećaja u komunikacijskim i navigacijskim sustavima te u električnoj mreži. Neposredno su ugroženi sudionici u zrakoplovnom prometu te osoblje i instrumenti/tehnologija svemirskih misija. Izuzev intrinzičnih svojstava samog CME-a, upravo međudjelovanje sa ambijentalnim magnetskim poljem i Sunčevim vjetrom uvjetuje geoefektivnost CME-ova.

Danas se uglavnom smatra da su CME-ovi cilindrične magnetske strukture u kojima magnetsko polje helikoidalno zavija oko toroidalne komponente koja prati središnju os cilindra (engl. *flux rope*, FR), koja može biti orijentirana pod arbitrarnim kutom s obzirom na ekliptiku. možemo razlikovati CME-ove male inklinacije (centralna os leži u ekliptici) i velike inklinacije (centralna os leži u ravnini okomitoj na ekliptiku).

Cilj ovog rada je ispitati utjecaj orijentacije CME-ova na međudjelovanje s ambijentalnim magnetskim poljem i Sunčevim vjetrom. Posljedica ovog međudjelovanja je nastanak tzv. zone interakcije (engl. *sheath region*)- područja ispred same magnetske strukture CME-a koju karakterizira povećana fluktuacija plazmenih i magnetskih parametara, povećana gustoća i temperatura, a uključuje nastanak magnetohidrodinamičkih (MHD) valova, akceleraciju i defleksiju Sunčevog vjetra te povlačenje (engl. *draping*) okolnog magnetskog polja. Konfiguracija ambijentalnog magnetskog polja uvelike ovisi o fazi samog Sunčevog jedanaestogodišnjeg ciklusa, a u prvoj aproksimaciji poprima izgled "rastegnutog" magnetskog dipola s otvorenim silnicama u blizini Sunčevog ekvatora. Zbog Sunčeve rotacije, magnetsko polje dodatno pokazuje zakrivljenost u obliku tzv. Parkerove spirale. Budući da niti magnetsko polje, niti Sunčev vjetar ne pokazuju homogenost u međuplanetarnom prostoru, očekujemo da CME-ovi različitih inkli-

nacija različito međudjeluju s ambijentom.

Veza između inklinacije i propagacije proučavana je s opažачkog aspekta (Martinić et al., 2022; Martinić et al., 2023). CME-ovi se mogu opažati pomoću daljinskih satelitskih mjerenja odnosno korištenjem mjerenja s koronagrafa. Baš kao što ime sugerira, koronagrafi su instrumenti specijalizirani za proučavanje najvišeg sloja Sunčeve atmosfere- korone. Na sebi imaju okultni disk čija je svrha blokiranje svjetlosti Sunčeve fotosfere, kako bi se sama korona uopće mogla opaziti. Korištenjem koronografskim mjerenja s više od jednog satelita dobivamo pogled na istu strukturu (CME) iz različitih smjerova pa je 3D rekonstrukcija CME-a moguća. Thernisien et al. (2006) su razvili Graduated Cylindrical Shell (GCS) model za 3D CME rekonstrukciju korištenjem koronografskih mjerenja sa STEREO i SOHO misija. U GCS modelu, unutarnja struktura CME-a je prikazana tzv. "praznim kroasanom" (engl. *hollow croissant*), a čine ga dvije strukture: stožaste noge i kvazicirkularni prednji dio. Svaki je FR potpuno opisan s ukupno šest GCS parametara: 1) longituda, 2) latituda i 3) visina najisturenije točke FR-a; 4) polukut kao mjera udaljenosti centra stožaste noge od najisturenije točke FR-a ; 5) aspect ratio kao mjera debljine stožaste noge i 6) tilt odnosno inklinacija FR-a s obzirom na solarni ekvator. Inklinaciju CME-a možemo odrediti i pomoću 2D rekonstrukcije. Chen et al. (1997) su uveli tehniku za ellipse fit 2D projekcije FR osi CME-a. Promjenom lokacije, duljine poluosi i inklinacije elipse mogu se odrediti širina i inklinacija promatranog CME-a. Karakterističan zapis CME-ova se može primijetiti i u in-situ podacima, za vrijeme prolaska CME-a kroz letjelicu. Najčešće se može uočiti trodijelna struktura: šok, zona interakcije i FR dio. Nailazak šoka karakterizira naglo povećanje magnetskog polja, brzine i temperature plazme. Nakon šoka tipično slijedi zona interakcije koju karakterizira plazma izražene turbulencije koja ima povećanu temperaturu i gustoću. Zona interakcije pokazuje velike fluktuacije plazme i magnetskog polja, a samo njeno trajanje je puno manje nego trajanje glavnog FR dijela (Kilpua et al., 2017). Nadalje, u zoni interakcije možemo opaziti i tzv. neradijalne tokove ambijentalne plazme tj. defleksiju plazme oko FR dijela CME-a. FR može imati desnu ili lijevu kiralnost, ovisno o relativnoj orijentaciji helikoidalnog i toroidalnog magnetskog polja. Inklinacija i kiralnost nam omogućavaju klasifikaciju svih opaženih FR-ova kao jedan od osam osnovnih tipova prema Mulligan et al. (1998), a od tih osam, četiri tipa su male inklinacije (toroidalna os položena u ekliptici) i četiri tipa su velike inklinacije (toroidalna os položena okomito na ekliptiku).

U Martinić et al. (2022) i Martinić et al. (2023) proučavani su CME-ovi konzistente dominantne inklinacije određene iz daljinskih i in-situ mjerenja u period 23. i 24. Sunčevog ciklusa. Nakon grupacije CME-ove prema njihovom dominantnom nagibu (CME-ovi s malom i velikom inklinacijom), statistički je ispitana razlika između propagacijskih svojstava tih dviju skupina. Analizirali smo vrijeme prolaska (pokazatelj otpora CME-a tijekom propagacije),

parametar otpora γ i neradijalne tokove unutar zone interakcije. Pronašli smo razliku u neradijalnim tokovima za dvije skupine događaja, ali razlika u otporu nije pronađena. Pronađena razlika u neradijalnim tokovima se može protumačiti kao okolna plazma koja zaobilazi FR u smjeru gdje je duljina FR front manja. Za događaje s malom inklinacijom, to je meridionalna ravnina, a za događaje s velikim inklinacijom to je ravnina ekliptike.

Nadalje, utjecaj orijentacije CME-ova na njihovu propagaciju je proučavan i pomoću European Heliospheric FORecasting Information Asset (EUHFORIA) modela- 3D MHD modela za propagaciju CME-ova Pomoell & Poedts (2018) što je prikazano u Martinić et al. (2024). U provedenim simulacijama CME-ovi su implementirani pomoću sferomak CME reprezentacije. Sferomak je kompaktna toroidalna struktura u kojoj je magnetsko polje generirano tokom plazme tako da vrijedi $\mathbf{J} \times \mathbf{B} = 0$, što znači da je Lorentzova sila jednaka nuli, tj. da je električna struja kolinearna s magnetskim polje. Napravljene su dvije simulacije za dva sferomaka potpuno istih svojstava, ali inklinacije različite za 90° , tako da jedan CME ima malu inklinaciju (leži u ekliptici), a drugi veliku inklinaciju (leži u meridionalnoj ravnini). Na ovaj način minimiziramo utjecaj ostalih svojstava CME-a kao što su masa, gustoća, poprečni presjek i relativna brzina na dinamiku. Također, postavke simulacije odabrane su tako da se minimizira interakciju CME-a s heliosferskim strujnim omotačem (engl., *heliospheric current sheath*) i da minimizira "tilting i drifting efekt" koji je detaljno opisan u Asvestari et al. (2022). Pokazano je da se trajanje zone interakcije eksponencijalno povećava s povećanjem radijalne udaljenosti i da se zona interakcije povećava s povećanjem udaljenosti od najisturenije točke sferomaka (engl., *apex*). Neradijalni tokovi plazme su u simulaciji za oba sferomaka veći izvan ekliptike nego u ekliptici. Ovo potvrđuje hipotezu iznesenu u opažачkim radovima da transverzalna komponenta međuplanetarnog magnetskog polja (indikativna za konfiguraciju Parkerove spirale) klizi okomito na CME gibanje zbog razvijenog gradijenta tlaka, kao što je istaknuto u Gosling & McComas (1987). Značajne razlike u neradijalnim tokovima u simulacijama za dva sferomaka ipak nisu pronađene. Pokazano je da izračun parametra otpora γ jako ovisi o rezoluciji same simulacije i bez dodatnih ispitivanja ga nije moguće sa sigurnošću odrediti. Iako se sferomak tijekom simulacije zaravnava (različita duljina fronte u meridionalnoj i ravnini ekliptike) on je na početku simulacije sferna struktura (jednaka duljina fronte u meridionalnoj i ekliptičkoj ravnini) i ovo najvjerojatnije maskira utjecaj inklinacije. Razvojem novih modela FR struktura i njihova implementacija u 3D MHD modele za propagaciju ostavlja prostora za naprednije ispitivanje utjecaja inklinacije pomoću simulacija.

Rezultati prezentiranih istraživanja osim što pokazuju utjecaj inklinacije na propagaciju CME-ova također pokazuju potrebu za boljim sveobuhvatnim razumijevanjem različitih doprinosa magnetohidrodinamičkom otporu kombinacijom opažачkog pristupa i modeliranjem.